HEPATOLOGY

Hepatocyte Elovl6 determines ceramide acyl-chain length and hepatic insulin sensitivity in mice

Journal:	*Hepatology*
Manuscript ID	HEP-19-1048.R1
Wiley - Manuscript type:	Original
Date Submitted by the Author:	n/a
Complete List of Authors:	Matsuzaka, Takashi; University of Tsukuba Faculty of Medicine Kuba, Motoko; University of Tsukuba Faculty of Medicine Koyasu, Saori; University of Tsukuba Faculty of Medicine yamamoto, yuta; Rikkyo University College of Science Department of Chemistry Motomura, Kaori; University of Tsukuba Faculty of Medicine Arulmozhiraja, Sundaram; Rikkyo University College of Science Department of Chemistry Ohno, Hiroshi; University of Tsukuba Faculty of Medicine Sharma, Rahul; University of Tsukuba Faculty of Medicine Shimura, Takuya; University of Tsukuba Faculty of Medicine Okajima, Yuka; University of Tsukuba Faculty of Medicine Han, Song-iee; University of Tsukuba Faculty of Medicine Aita, Yuichi; University of Tsukuba Faculty of Medicine Mizunoe, Yuhei; University of Tsukuba Faculty of Medicine Osaki, Yoshinori; University of Tsukuba Faculty of Medicine Iwasaki, Hitoshi; University of Tsukuba Faculty of Medicine Yatoh, Shigeru; University of Tsukuba Faculty of Medicine Suzuki, Hiroaki; University of Tsukuba Faculty of Medicine Sone, Hirohito; Niigata University Takeuchi, Yoshinori; University of Tsukuba Faculty of Medicine Yahagi, Naoya; University of Tsukuba Faculty of Medicine Miyamoto, Takafumi; University of Tsukuba Faculty of Medicine Sekiya, Motohiro; University of Tsukuba Faculty of Medicine Nakagawa, Yoshimi; University of Tsukuba Faculty of Medicine Ema, Masatsugu; Shiga University of Medical Science Takahashi, Satoru; University of Tsukuba Faculty of Medicine Tokiwa, Hiroaki; Rikkyo University College of Science Department of Chemistry Shimano, Hitoshi; University of Tsukuba Faculty of Medicine
Keywords:	Non-alcoholic fatty liver disease, Fatty acid, Lipogenesis, Patatin-like phospholipase domain-containing protein 3, Protein phosphatase 2A

Manuscript ID: HEP-19-1048

Hepatocyte Elovl6 determines ceramide acyl-chain length and hepatic insulin sensitivity in mice

Takashi Matsuzaka[1,2], Motoko Kuba[1], Saori Koyasu[1], Yuta Yamamoto[3], Kaori Motomura[1], Sundaram Arulmozhiraja[3], Hiroshi Ohno[1], Rahul Sharma[1], Takuya Shimura[1], Yuka Okajima[1], Song-iee Han[1], Yuichi Aita[1], Yuhei Mizunoe[1], Yoshinori Osaki[1], Hitoshi Iwasaki[1], Shigeru Yatoh[1], Hiroaki Suzuki[1], Hirohito Sone[4], Yoshinori Takeuchi[1], Naoya Yahagi[1], Takafumi Miyamoto[1,2], Motohiro Sekiya[1], Yoshimi Nakagawa[1,5], Masatsugu Ema[6], Satoru Takahashi[2,5,7,8,9], Hiroaki Tokiwa[3], and Hitoshi Shimano[1,5,8,10] *

Emails

t-matsuz@md.tsukuba.ac.jp, motokoamiki@gmail.com, sao_kys@yahoo.co.jp, 17lb019f@rikkyo.ac.jp, korm013730@md.tsukuba.ac.jp, raja@rikkyo.ac.jp, hohno@md.tsukuba.ac.jp, s1430593@u.tsukuba.ac.jp, s1830411@s.tsukuba.ac.jp, s1430456@u.tsukuba.ac.jp, shan@md.tsukuba.ac.jp, metabmetabmetab@gmail.com,

ymizunoe@md.tsukuba.ac.jp, oosaki-tuk@umin.ac.jp, iwasaki@md.tsukuba.ac.jp,

shigeru.yatoh@md.tsukuba.ac.jp, hirosuzu@md.tsukuba.ac.jp, sone@med.niigata-u.ac.jp,

yoshinori-takeuchi@umin.ac.jp, nyahagi-tky@umin.ac.jp, takmi565@md.tsukuba.ac.jp,

msekiya@md.tsukuba.ac.jp, yosshy@md.tsukuba.ac.jp, mema@belle.shiga-med.ac.jp,

satoruta@md.tsukuba.ac.jp, tokiwa@rikkyo.ac.jp, hshimano@md.tsukuba.ac.jp

Affiliations

[1]Department of Internal Medicine (Endocrinology and Metabolism), Faculty of Medicine, University of Tsukuba, 1-1-1 Tennodai, Tsukuba, Ibaraki 305-8575, Japan

[2]Transborder Medical Research Center, University of Tsukuba, 1-1-1 Tennodai, Tsukuba, Ibaraki 305-8575, Japan

[3]Department of Chemistry, Rikkyo University, Nishi-Ikebukuro, Toshima, Tokyo 171-8501, Japan

[4]Department of Internal Medicine, Faculty of Medicine, Niigata University, 1-754 Asahimachi, Niigata 951-8510, Japan

[5]International Institute for Integrative Sleep Medicine (WPI-IIIS), University of Tsukuba, 1-1-1 Tennodai, Tsukuba, Ibaraki 305-8575, Japan

[6]Department of Stem Cells and Human Disease Models, Research Center for Animal Life Science, Shiga University of Medical Science, Seta, Tsukinowa-cho, Otsu, Shiga 520-2192, Japan

[7]Department of Anatomy and Embryology, Faculty of Medicine, University of Tsukuba, 1-1-1 Tennodai, Tsukuba, Ibaraki 305-8575, Japan

[8]Life Science Center for Survival Dynamics, Tsukuba Advanced Research Alliance (TARA), University of Tsukuba, 1-1-1 Tennodai, Tsukuba, Ibaraki 305-8575, Japan

[9]Laboratory Animal Resource Center (LARC), University of Tsukuba, 1-1-1 Tennodai, Tsukuba, Ibaraki 305-8575, Japan

[10]AMED-CREST, Japan Agency for Medical Research and Development (AMED), 1-7-1, Ohte-machi, Chiyoda-ku, Tokyo, 100-0004, Japan

Keywords

Non-alcoholic fatty liver disease

Fatty acid

Lipogenesis

Patatin-like phospholipase domain-containing protein 3

Protein phosphatase 2A

Contact information

* Correspondence to: Hitoshi Shimano, MD, Ph.D.

Department of Internal Medicine (Endocrinology and Metabolism), Faculty of Medicine, University of Tsukuba, 1-1-1 Tennodai, Tsukuba, Ibaraki 305-8575, Japan.

Tel. and Fax: +81-29-863-2081; E-mail: hshimano@md.tsukuba.ac.jp

Abbreviations

NAFLD, non-alcoholic fatty liver disease; T2D, type 2 diabetes; Elovl6, ELOVL fatty acid elongase 6; FA, fatty acid; LKO, liver-specific Elovl6 knockout; HSD, high-sucrose diet; Pnpla3, patatin-like phospholipase domain-containing protein 3; PP2A, protein phosphatase 2A; CerS4, ceramide synthase 4; ER, endoplasmic reticulum; LD, lipid droplet; TAG, triacylglycerol; NASH, non-alcoholic steatohepatitis; DNL, *de novo* lipogenesis; GKO, global deletion of *Elovl6*; HFHS, high-fat and high-sucrose; LC-MS/MS, liquid chromatography coupled with tandem mass spectrometry; DMEM, Dulbecco's Modified Eagle's Medium; T-Cho, total cholesterol; eWAT, epididymal white adipose tissue; AUC, area under the curve; IR, insulin receptor; IRS, insulin receptor substrate; PKC, protein kinase C; GSK3, glycogen synthase kinase 3; PRAS40, proline-rich Akt substrate of 40 kDa; qPCR, quantitative real-time

PCR; Srebf1c, sterol regulatory element binding protein 1c; ACC, acetyl-CoA carboxylase; Fasn, fatty acid synthase; Scd, stearoyl-CoA desaturase; GFP, green fluorescent protein; PL, phospholipid; I2PP2A, Inhibitor 2 of PP2A; shRNA, short hairpin RNA.

Financial support

This work was supported by AMED-CREST from the Japan Agency for Medical Research and Development, AMED (to H.S.); Grants-in-Aid for Scientific Research (A) 15H02541 (to H.S.), Scientific Research (A) 18H04051, Scientific Research on Innovative Areas 17H06395 (to H.S.), Scientific Research (B) 15H03093 (to T.M.), Scientific Research (B) 18H03189 (to T.M.), and Program to Disseminate Tenure Tracking System (to T.M.) from the Ministry of Science, Education, Culture, and Technology of Japan; Front Runner of Future Diabetes Research from Japan Foundation for Applied Enzymology (to T.M.); Ono Medical Research Foundation (to T.M.); Takeda Science Foundation (to T. M.); Mochida Memorial Foundation for Medical and Pharmaceutical Research (to T. M.); Kowa Life Science Foundation (to T. M.).

ABSTRACT

Dysfunctional hepatic lipid metabolism is a cause of non-alcoholic fatty liver disease (NAFLD), the most common chronic liver disorder worldwide, and is closely associated with insulin resistance and type 2 diabetes (T2D). ELOVL fatty acid elongase 6 (Elovl6) is responsible for converting C16 saturated and monounsaturated fatty acids (FAs) into C18 species. We have previously shown that Elovl6 contributes to obesity-induced insulin resistance by modifying hepatic C16/C18-related FA composition. To define the precise molecular mechanism by which hepatic Elovl6 affects energy homeostasis and metabolic disease, we generated liver-specific Elovl6 knockout (LKO) mice. Unexpectedly, LKO mice were not protected from high-fat diet-induced insulin resistance. Instead, LKO mice exhibited higher insulin sensitivity than controls when consuming a high-sucrose diet (HSD), which induces lipogenesis. Hepatic patatin-like phospholipase domain-containing protein 3 (Pnpla3) expression was downregulated in LKO mice, and adenoviral Pnpla3 restoration reversed the enhancement in insulin sensitivity in HSD-fed LKO mice. Lipidomic analyzes showed that the hepatic ceramide(d18:1/18:0) content was lower in LKO mice, which may explain the effect on insulin sensitivity. Ceramide(d18:1/18:0) enhances protein

phosphatase 2A (PP2A) activity by interfering with the binding of PP2A to its biological inhibitor I2PP2A, leading to Akt dephosphorylation. Its production involves the formation of an Elovl6-ceramide synthase 4 (CerS4) complex in the endoplasmic reticulum (ER) and a Pnpla3-CerS4 complex on lipid droplets (LDs). Consistent with this, liver-specific Elovl6 deletion in *ob/ob* mice reduced both hepatic ceramide(d18:1/18:0) and PP2A activity, and ameliorated insulin resistance. *Conclusion:* Our study demonstrates the key role of hepatic Elovl6 in the regulation of the acyl-chain composition of ceramide, and that C18:0-ceramide is a potent regulator of hepatic insulin signaling linked to Pnpla3-mediated NAFLD.

INTRODUCTION

Non-alcoholic fatty liver disease (NAFLD), characterized by excessive triacylglycerol (TAG) accumulation in hepatocytes, is recognized as a hepatic phenotype of the metabolic syndrome (1). A large majority of obese and diabetic individuals develop NAFLD, but it is also a risk factor for various other conditions, including insulin resistance, hyperlipidemia, and type 2 diabetes (T2D) (2, 3). Furthermore, non-alcoholic steatohepatitis (NASH), a severe form of NAFLD characterized by hepatocellular damage, lobular inflammation, abnormal glucose tolerance, and fibrosis, can progress to cirrhosis and hepatocellular carcinoma (4, 5).

Chronic and/or excess consumption of carbohydrates and saturated fatty acids (FAs) is associated with the development of hepatic insulin resistance (6, 7). Hepatic insulin resistance promotes aberrant glucose production, *de novo* lipogenesis (DNL), atherogenic dyslipidemia, and NAFLD, which are major risk factors for T2D and cardiovascular disease (8, 9). There are few effective therapies for hepatic insulin resistance or obesity, and the development of novel therapeutics necessitates a better understanding of the mechanistic relationship between obesity and NAFLD.

Elongation and desaturation are central steps in the *de novo* synthesis of long-chain FAs, and length and saturation are critical determinants of FA function and metabolic fate (10). ELOVL fatty acid elongase 6 (Elovl6) is a microsomal enzyme that is involved in the elongation of C16 saturated and monounsaturated FAs to form C18 FAs (11, 12). Loss of Elovl6 function reduces stearate (C18:0) and oleate (C18:1n-9) concentrations but increases palmitate (C16:0), palmitoleate (C16:1n-7), and vaccinate (C18:1n-7) concentrations (13, 14). We have previously reported that mice with global deletion of *Elovl6* (GKO) are protected against insulin resistance when fed a high-fat and high-sucrose (HFHS) diet or when mated to leptin-deficient *ob/ob* mice because the hepatic FA composition is modified (13). In the present study, we generated liver-specific *Elovl6* knockout (LKO) mice to investigate the role of Elovl6 in the hepatic control of lipid metabolism and energy homeostasis.

MATERIALS AND METHODS

Animals.

All animal husbandry and experimental protocols complied with institutional guidelines

and were approved by the Animal Experiment Committee of the University of Tsukuba. The mice were housed in specific pathogen-free conditions under a 12-h light/dark cycle, with free access to water and either standard chow (MF; Oriental Yeast, Tokyo, Japan) or a HFHS diet (F2HFHSD; Oriental Yeast, Tokyo, Japan) or a high-sucrose diet high-sucrose diet (HSD; D11725; Research Diets, New Jersey, USA) in the Laboratory Animal Resource Center at the University of Tsukuba. The detailed dietary composition of the HFHS diet and HSD is shown in Supporting Table 1.

Lipidomic profiling.

The MxP® Lipids platform (Metanomics Health GmbH, Berlin, Germany) was used for the entire lipid analysis workflow as described in the Online Materials and Methods.

Statistical analysis.

Values are expressed as mean ± SEM. Student's t-tests were used to compare the means of two groups and one-way ANOVA was used for multiple group mean comparisons. All analyzes were performed using GraphPad Prism 5 (GraphPad Software Inc., CA, USA), and $p < 0.05$ (two-tailed) was considered to represent statistical significance.

RESULTS

LKO mice are not protected from HFHS diet-induced insulin resistance

We generated LKO mice by crossing Elovl6 lox/lox mice with albumin promoter-Cre transgenic mice, which express Cre exclusively in postpartum hepatocytes (Supporting Figure 1). To determine whether liver-specific *Elovl6* deletion produces the same metabolic phenotype as that of GKO mice (13), Flox and LKO mice were fed a normal chow or HFHS diet from 8 weeks of age. There were no differences in body weight (Supporting Figure 2A), liver weights (Supporting Figure 2B), or hepatic TAG or total cholesterol (T-Cho) concentrations (Supporting Figure 2C) between Flox and LKO mice on either a chow or HFHS diet. Epididymal white adipose tissue (eWAT) weight was slightly but significantly lower in LKO mice than in Flox mice on an HFHS diet (Supporting Figure 2B). In contrast to GKO, however, liver-specific Elovl6 deletion did not reduce plasma glucose or insulin concentrations in mice on an HFHS diet (Supporting Figure 2D). Moreover, oral glucose tolerance tests (OGTTs; Supporting Figure 2E) and insulin tolerance tests (ITTs; Supporting Figure 2F) showed no significant differences between Flox and LKO mice fed an HFHS diet. These results

demonstrate that hepatocyte-specific *Elovl6* deficiency is insufficient to ameliorate insulin resistance induced by an HFHS diet.

Insulin sensitivity is higher in LKO mice fed a lipogenic diet

We next fed Flox and LKO mice an HSD for 14 days to induce Elovl6 activity and DNL, which revealed several phenotypic differences. On the HSD diet, there were no differences in body, liver and eWAT weights (Supporting Figure 3A), or in plasma lipid concentrations (Supporting Figure 3B) between Flox and LKO mice. The HSD induced a similar degree of hepatosteatosis, as demonstrated by increases in hepatic TAG and T-Cho concentrations (Figure 1A) and number of lipid droplets (LDs) (Supporting Figure 3C) in both genotypes, compared to the chow diet. Furthermore, *Elovl6* deletion exacerbated the changes in hepatic FA composition induced by HSD feeding. Specifically, HSD feeding of LKO mice significantly lowered the stearate and oleate content, but increased the palmitate, palmitoleate, and vaccinate content, relative to Flox mice (Figure 1B). HSD-fed LKO mice had significantly lower plasma glucose and insulin levels compared to HSD-fed Flox controls (Figure 1C). During OGTTs, HSD-fed LKO mice exhibited lower plasma glucose excursions than HSD-fed Flox mice, evidenced by a lower area under the curve (AUC; Figure 1D). Furthermore,

during ITTs, HSD-fed LKO mice demonstrated lower plasma glucose concentrations than HSD-fed Flox mice (Figure 1E). These results suggest that LKO mice are more insulin-sensitive than Flox mice when consuming an HSD.

We next evaluated insulin signaling following an intravenous injection of insulin. Insulin administration had similar effects on total insulin receptor (IR) and phospho-IR protein levels, and on the ratio of phosphorylated IR to total IR in HSD-fed Flox and LKO mouse liver (Figure 1F). We have previously shown that global *Elovl6* deficiency increases total and phosphorylated insulin receptor substrate (IRS)-2 protein levels and suppresses protein kinase C (PKC) ε activity in the liver, which at least partially explains the amelioration of diet-induced insulin resistance (13). However, the total and phosphorylated levels of IRS-1 and IRS-2 proteins (Supporting Figure 3D), and PKCε translocation to the membrane, an index of PKCε activity (Supporting Figure 3E), were not affected by LKO in the liver of HSD-fed mice. In contrast, the insulin-induced phosphorylation of Akt (Ser473, Thr308) was much higher in the livers of HSD-fed LKO mice than in those of HSD-fed Flox mice (Figure 1F). In addition, the insulin-induced phosphorylation of the Akt substrates glycogen synthase kinase 3 (GSK3) α/β (Ser21/9) and proline-rich Akt substrate of 40 kDa (PRAS40; Thr246) was

significantly higher in the livers of LKO mice than in those of Flox mice. The insulin-induced phosphorylation of Akt (Ser473) was similar in the eWAT and muscle of Flox and LKO mice (Supporting Figure 3F). These data demonstrate that the higher insulin sensitivity in HSD-fed LKO mice is mediated through an enhancement in the hepatic insulin signaling *via* Akt.

Dietary lipids do not normalize the higher insulin sensitivity in HSD-fed LKO mice

Because stearate and oleate content was lower in the liver of LKO mice, we wished to determine whether dietary supplementation with these FAs could reverse the increase in insulin sensitivity identified in HSD-fed LKO mice. We therefore supplemented the HSD with 20% by mass of both tristearin and triolein. However, after 14 days on a diet supplemented with stearate and oleate, LKO mice demonstrated greater insulin sensitivity, as evaluated using an ITT (Supporting Figure 4A), suggesting that FA(s) endogenously synthesized by Elovl6 are involved in the regulation of hepatic insulin sensitivity.

LKO mice demonstrate an altered hepatic gene expression profile

To identify candidate genes associated with the enhancement in hepatic insulin

sensitivity in HSD-fed LKO mice, livers from Flox and LKO mice fed an HSD were profiled using microarray analysis. The heatmap in Figure 2A and Supporting Table 2 list all the genes with significant differences in expression *versus* controls. Pathway analysis revealed highly significant downregulation of eight pathways involved in lipid metabolism (Figure 2B). We next performed quantitative real-time PCR (qPCR) analysis to confirm the major findings of the microarray analysis, and found that liver-specific Elovl6 deficiency was associated with lower expression of sterol regulatory element binding protein 1c (*Srebf1c*) mRNA (Figure 2C) and the nuclear active form of SREBP-1 protein (Supporting Figure 4B), the major transcription factor involved in the transcriptional regulation of lipogenesis by carbohydrates (8, 15). Moreover, liver-specific Elovl6 deficiency significantly impaired the HSD-induced upregulation of hepatic mRNAs encoding lipogenic enzymes, such as acetyl-CoA carboxylase 1 (*Acc1*), fatty acid synthase (*Fasn*), and stearoyl-CoA desaturase 1 (*Scd1*) (Supporting Figure 4C). A volcano plot demonstrates that the genes significantly downregulated by *Elovl6* deficiency (Supporting Figure 4D) included patatin-like phospholipase domain containing 3 (*Pnpla3*), which encodes a membrane-bound protein with a predominant TAG lipase activity (16, 17). qPCR analysis confirmed that *Pnpla3* expression was increased 67-fold by HSD feeding in the liver of Flox mice and

reduced by 68% in the liver of LKO mice (Figure 2C). A similar expression pattern was also identified for the *Pnpla3* paralog *Pnpla5* (Supporting Figure 4E). In addition, we performed immunoblotting for Pnpla3 and found that its protein abundance was lower in the liver of LKO mice than in that of Flox mice (Supporting Figure 4F).

Downregulation of Pnpla3 mediates the increase in insulin sensitivity in HSD-fed LKO mice

To determine if the Pnpla3 reduction contributes to the higher insulin sensitivity in HSD-fed LKO mice, Flox and LKO mice consuming an HSD were injected with a recombinant adenovirus encoding mouse Pnpla3 (Ad-Pnpla3) or green fluorescent protein (Ad-GFP). Hepatic Pnpla3 protein was expressed at similar levels in HSD-fed Ad-Pnpla3-infected LKO mice and Flox mice, according to the results of immunoblotting (Figure 2D). Pnpla3 overexpression did not affect body weight, but increased liver weight to a similar extent in both Flox and LKO mice (Supporting Figure 5A). However, Pnpla3 overexpression did not affect the hepatic lipid content (Supporting Figure 5B, C) or liver pathology (Supporting Figure 5C, D) in Flox and LKO mice. Remarkably, the restoration of hepatic Pnpla3 protein expression in HSD-fed LKO mice reversed both the increase in insulin sensitivity (Figure 2E) and the

increase in the insulin-stimulated phosphorylation of hepatic Akt (Ser473, Thr308), GSK3α/β, and PRAS40 (Figure 2F). These results suggest that Elovl6- and Pnpla3-dependent lipid metabolic pathways are crucial in the regulation of hepatic insulin signaling under lipogenic conditions.

Lipid profiling of Elovl6- and Pnpla3-regulated lipids in the liver

We hypothesized that Elovl6 and Pnpla3 cooperate in the regulation of hepatic insulin sensitivity by changing the acyl-chain composition of specific lipid(s) that modulate insulin action. To test this hypothesis, we performed lipidomics on liver samples from HSD-fed Flox and LKO mice injected with either Ad-GFP or Ad-Pnpla3. Deletion of *Elov6* significantly increased the content of 39 lipid metabolites and reduced the content of 39 other lipid metabolites in the liver (Figure 3A and Supporting Table 3). These Elovl6-related changes occurred in a variety of lipids, including ceramides, cholesterol esters, FFAs, phospholipids (PLs), lysoPL, sphingomyelins, and TAG. Conversely, the restoration of hepatic Pnpla3 expression in LKO mice increased the content of six lipid metabolites and reduced the content of 27 metabolites in the liver (Figure 3A and Supporting Table 3). Consistent with a physiologic role of Pnpla3 in determining the TAG and PL composition of hepatic LDs (18-20), Pnpla3 expression altered the

distribution of TAG and FFA species, as well as of ceramide and sphingomyelin species. Among these, the following specific lipids exhibited changes corresponding to the effects of manipulating Elovl6 and Pnpla3. The concentration of ceramide(d18:1/18:0) was lower in LKO liver than in Flox liver and was increased by the restoration of Pnpla3 expression in LKO mice. In contrast, the concentration of ceramide(d18:2/22:1) was higher in LKO liver than in Flox liver, and was reduced by the restoration of Pnpla3 expression.

Ceramides have been implicated in the lipid-induced inhibition of insulin sensitivity (21-23). Moreover, specific ceramide species, which are defined by their fatty acyl-chain length, can have specific biologic functions (24-26). Therefore, we expanded our initial lipidomic analysis by analyzing multiple ceramide species to determine whether their hepatic concentrations are modulated by Elovl6 and Pnpla3. The total hepatic ceramide content was not significantly affected by genotype, diet, or adenovirus infection (Supporting Figure 6A), and 19 of the ceramide species evaluated were similar in abundance between the HSD-fed Flox and LKO mice (Figure 3B). However, Elovl6 deficiency significantly reduced the content of ceramide(d18:1/18:0) and ceramide(d18:2/18:0) in the liver. In contrast, restoration of Pnpla3 significantly

increased the content of ceramide(d18:1/18:0) and ceramide(d18:1/20:0), but significantly reduced the content of ceramide(d18:2/22:1) in the liver of HSD-fed LKO mice (Figure 3C). An injection of a small quantity of Pnpla3 adenovirus significantly increased the content of ceramide(d18:1/16:0) and ceramide(d18:1/18:0), and significantly reduced the content of ceramide(d18:2/22:1) in the liver of HSD-fed Flox mice. Elovl6 deficiency significantly reduced the HSD-induced increase in hepatic ceramide(d18:1/18:0), and this effect was attenuated by the restoration of Pnpla3 expression (Figure 3B, C). Thus, changes in ceramide(d18:1/18:0) concentration are strongly associated with the insulin sensitivity of LKO mice.

Ceramide(d18:1/18:0) increases PP2A activity and inhibits insulin signaling by reducing the interaction between PP2A and I2PP2A

Because ceramides are known to regulate insulin sensitivity by activating PP2A and PKCζ (21-23), we assessed the hepatic activities of PP2A and PKCζ. HSD-feeding significantly increased PP2A activity in the liver of Flox mice, but not LKO mice (Figure 3D). The restoration of hepatic Pnpla3 expression in HSD-fed LKO mice significantly increased PP2A activity to a level comparable to that of HSD-fed Flox mice (Figure 3D). We also assessed the phosphorylation status of hepatic PKCζ and

found that phosphorylation at Thr410, which is required for PKCζ activation (21), was not altered by Elovl6 deficiency or HSD-feeding (Figure 3E). These results suggest that the higher hepatic insulin sensitivity in HSD-fed LKO mice may be mediated through the suppression of C18:0-ceramide production, resulting in a reduction in ceramide-induced PP2A activity in the liver and lower PP2A-dependent downregulation of insulin signaling, implying a disinhibition of insulin signaling.

To determine whether ceramide(d18:1/18:0) inhibits insulin signaling, human hepatoma HepG2 cells were treated with 10 μM ceramide(d18:1/16:0), ceramide(d18:1/18:0), or ceramide(d18:1/20:0) for 4 h, and with vehicle or insulin for the last 10 min of this period (Figure 4A). Treatment with ceramide(d18:1/16:0) or ceramide(d18:1/20:0) did not affect insulin-stimulated phosphorylation of Akt, but ceramide(d18:1/18:0) treatment significantly suppressed the insulin-stimulated phosphorylation of Akt compared to vehicle and ceramide(d18:1/16:0) treatment.

Ceramide inhibits insulin signaling by activating PP2A, a serine/threonine phosphatase that dephosphorylates and thus deactivates Akt (27). Previous studies have demonstrated that PP2A activity is modulated by phosphorylation at Tyr307 and

carboxymethylation at Leu309 of the C subunit (28). Immunoblot analysis revealed that Elovl6 deficiency and Pnpla3 expression did not affect the levels of phosphorylation or carboxymethylation of the PP2A C subunit in the liver (Supporting Figure 6B). In addition, ceramide activates PP2A activity in part via direct binding of Inhibitor 2 of PP2A (I2PP2A/SET oncogene), which prevents the interaction between PP2A and I2PP2A (27, 29). Notably, I2PP2A preferentially binds C18-ceramides over C14–C16 ceramides (30, 31). We hypothesized that if the major effect of Elovl6 deficiency on hepatic insulin signaling is to reduce hepatic ceramide(d18:1/18:0) production, this effect would be modulated by altering I2PP2A–PP2A binding. To test this hypothesis, HepG2 cells transfected with HA-tagged PP2A catalytic subunit alpha isoform (PPP2CA) and FLAG-tagged I2PP2A were treated with ceramide(d18:1/16:0), ceramide(d18:1/18:0), or ceramide(d18:1/20:0). Ceramide(d18:1/16:0) did not change the PPP2CA–I2PP2A interaction, but ceramide(d18:1/18:0) and ceramide(d18:1/20:0) significantly inhibited the PPP2CA–I2PP2A interaction (Figure 4B). This reduction in the PPP2CA–I2PP2A interaction was much larger in ceramide(d18:1/18:0)-treated cells than in ceramide(d18:1/20:0)-treated cells.

To confirm the role of I2PP2A in ceramide(d18:1/18:0)-induced insulin resistance,

HepG2 cells were infected with lentivirus expressing a short hairpin RNA (shRNA) targeting I2PP2A or a scrambled shRNA (control). Immunoblotting confirmed a significant reduction in the abundance of I2PP2A protein following infection with the specific shRNA (Figure 4C). In HepG2 cells infected with control shRNA, ceramide(d18:1/18:0) reduced the insulin-stimulated phosphorylation of Akt (Figure 4C). Knockdown of I2PP2A reduced the insulin-stimulated phosphorylation of Akt and abrogated the inhibitory effect of ceramide(d18:1/18:0) on the insulin-stimulated phosphorylation of Akt (Figure 4C). Thus, ceramide(d18:1/18:0) inhibits Akt signaling in a I2PP2A-dependent manner to regulate PP2A activity.

To determine the structural basis of the interaction between ceramides and I2PP2A, we performed molecular modeling using the crystal structure of I2PP2A and ceramide(d18:1/16:0), ceramide(d18:1/18:0), or ceramide(d18:1/20:0) as probes, and studied their interactions quantitatively using the first-principles calculations-based fragment molecular orbital method (32). The relative binding scores, the theoretical interaction energies between each ceramide and I2PP2A, from the value of ceramide(d18:1/16:0), are shown in Figure 4D. Consistent with the biologic data, this model suggested that the binding affinity of each species to I2PP2A is in the descending

order ceramide(d18:1/18:0), ceramide(d18:1/20:0), and ceramide(d18:1/16:0). Thus, the potent effect of ceramide(d18:1/18:0) on I2PP2A–PP2A binding shown by *in vivo* and *in vitro* assays was also confirmed by a computer simulation.

Ceramide synthase (CerS) associates with Elovl6 and Pnpla3 on the endoplasmic reticulum (ER) and at the ER-LD interface, respectively

Our findings suggest that both Elovl6 and Pnpla3 are involved in metabolic pathways that regulating ceramide acyl species. *De novo* ceramide synthesis involves six distinct CerSs, CerS1 to CerS6, which are specialized for the synthesis of ceramides with different fatty acyl-chain lengths (26). Therefore, we sought to identify physical interactions among Elovl6, Pnpla3, and CerS4, a CerS that synthesizes C18–C20 ceramides and is highly expressed in the liver (33).

We first characterized the subcellular distributions of each protein in HEK293 cells using confocal microscopy. When expressed in HEK293 cells treated with oleate to increase LD formation, C-terminal FLAG-tagged Elovl6 (Elovl6-FLAG) and V5-tagged CerS4 (CerS4-V5) displayed a reticular distribution that likely corresponded to the ER (Supporting Figure 7A). Consistent with previous reports, HA-tagged Pnpla3

(Pnpla3-HA) accumulated on membranes and in LDs (Supporting Figure 7B). In co-expression experiments, Elovl6-FLAG appeared to colocalize with CerS4-V5 in the ER, while Pnpla3-HA and CerS4-V5 appeared to colocalize at the ER-LD interface upon oleate loading (Figure 5A). When co-expressed with Elovl6-FLAG, Pnpla3-HA displayed a reticular distribution, likely corresponding to the ER and LDs (Figure 5A). However, within 24 h of transfection, both Elovl6-FLAG- and Pnpla3-HA-expressing HEK293 cells were smaller and rounder, with dense cytoplasm and tightly-packed organelles, suggestive of the induction of apoptosis, which was presumably due to the greater production of C18:0-ceramide and the higher PP2A activity (27).

We next aimed to identify interactions among Elovl6, Pnpla3, and CerS4 by immunoprecipitation from co-overexpressing cells. HEK293 cells were transfected with Elovl6-FLAG and CerS4-V5, Pnpla3-HA and CerS4-V5, or Elovl6-FLAG and Pnpla3-HA, and then treated with oleate for 24 h. This confirmed the interaction of Elovl6-FLAG with CerS4-V5 (Figure 5B and Supporting Figure 8A), and Pnpla3-HA was also shown to interact with CerS4-V5 (Figure 5B and Supporting Figure 8B). However, Elovl6-FLAG did not interact with Pnpla3-HA (Figure 5B and Supporting Figure 8C). Taken together, these results suggest that Elovl6 and Pnpla3 may be

involved in regulating a pool of C18:0-ceramide by forming Elovl6-CerS4 and Pnpla3-CerS4 complexes on the ER and at the ER-LD interface, respectively.

Liver-specific deletion of *Elovl6* ameliorates insulin resistance in *ob/ob* mice

To further define the role of hepatic Elovl6 in obesity and insulin resistance, we assessed the effects of liver-specific *Elovl6* deletion in leptin-deficient *ob/ob* mice, a widely used animal model of severe obesity, steatohepatitis, and insulin resistance. Mice with liver-specific disruption of Elovl6 (*ob/ob*-LKO) were severely obese, with similar body and eWAT weight to those of *ob/ob* mice (Figure 6A). Liver weight was significantly greater in *ob/ob*-LKO mice than in *ob/ob* mice (Figure 6A), but with similar degrees of hepatosteatosis (Supporting Figure 9A–C), although there were prominent differences in FA composition (Supporting Figure 9D). Liver-specific disruption of *Elovl6* significantly reduced plasma glucose and insulin concentrations compared to *ob/ob* mice (Figure 6B). OGTTs showed that glucose intolerance was moderately ameliorated in *ob/ob*-LKO mice *versus* *ob/ob* mice (Figure 6C). Furthermore, ITTs showed that the insulin resistance was significantly less severe in *ob/ob*-LKO mice than in *ob/ob* mice (Figure 6C). The expression of lipogenic genes, including *Elovl6*, *Srebf1c*, *Fasn*, *Scd1*, and *Pnpla3*, was significantly higher in the livers

of *ob/ob* mice than in Flox mice (Figure 6D). However, *ob/ob*-LKO mice showed significantly lower hepatic expression of these lipogenic genes than *ob/ob* mice. We also quantified the relative content of representative ceramide species in the livers of Flox, *ob/ob*, and *ob/ob*-LKO mice and found that the increase in ceramide(d18:1/18:0) content in *ob/ob* mouse liver was absent in *ob/ob*-LKO mouse liver (Figure 6E). Moreover, the content of hepatic ceramide(d18:1/20:0), ceramide(d18:1/24:1), ceramide(d17:1/18:0), ceramide(d17:1/24:1), ceramide(d18:2/18:0), and ceramide(d18:2/20:0) was significantly lower, and the content of ceramide(d18:1/16:0) was significantly higher in *ob/ob*-LKO mice than in *ob/ob* mice. The activity of PP2A in the liver of *ob/ob*-LKO mice was also lower than in *ob/ob* mice (Figure 6F), which was comparable to the trend identified in Flox mice. Taking these results together, it can be concluded that hepatic Elovl6-mediated C18:0-ceramide production regulates insulin sensitivity through the modulation of PP2A activity under lipogenic conditions, and that liver-specific deletion of Elovl6 can ameliorate insulin resistance in the obese diabetic state.

DISCUSSION

In the present study, we aimed to determine the role of hepatic Elovl6-synthesized long-chain FAs in lipid metabolism and glucose homeostasis by generating liver-specific *Elovl6*-deficient mice. Our results demonstrate that hepatic Elovl6 regulates hepatic insulin sensitivity, in part by affecting the hepatic ceramide FA composition. In turn, ceramide FA composition regulates insulin signaling under lipogenic conditions by modulating the interaction between I2PP2A and PP2A, and PP2A activity. The proposed pathway is presented in Figure 7 and Supporting Figure 9E.

There is increasing evidence that diets high in carbohydrate result in greater DNL, obesity, ectopic lipid accumulation, and insulin resistance in animals, as well as in humans (23, 34–36). Hyperglycemia stimulates pancreatic insulin secretion, which, together with dietary carbohydrate, stimulates hepatic DNL by upregulating lipogenic gene transcription. The transcription factors responsible for mediating this include SREBP-1c, which regulates hepatic DNL primarily by regulating the expression of genes involved in DNL, lipid homeostasis, and glucose metabolism (8). *Elovl6* expression is highly responsive to carbohydrates and insulin, and its promoter contains

response elements for SREBP-1c (12, 37). *Pnpla3* expression is also strongly induced by carbohydrate feeding and insulin through the lipogenic transcription factors SREBP-1c and carbohydrate-response element-binding protein (38, 39). Moreover, accumulation of long-chain FAs, such as stearate and oleate, the major end-products of the SREBP-1c pathway, prevents the degradation of the Pnpla3 protein by the proteasome and stabilize it, thereby increasing its abundance (38). We found that the expression levels of *Srebf1c* and its target lipogenic genes, including *Acc1*, *Fasn*, *Scd1*, and *Pnpla3*, were collectively suppressed in the livers of HSD-fed LKO mice. How does hepatic Elovl6 regulate lipogenic gene expression? On an HSD diet, hepatic Elovl6 deficiency markedly reduced the nuclear levels of SREBP-1, indicating that hepatic Elovl6 expression and its products are required for the maturation and nuclear translocation of active SREBP-1 protein. Although the mechanism whereby Elovl6 deficiency reduces the maturation of SREBP-1 protein and *Srebf1c* mRNA expression remains to be elucidated, a recent study has suggested that the altered acyl-chain composition of PLs in the ER induced by Elovl6 deficiency may reduce SREBP-1 post-translational processing (40).

Our data demonstrate a novel role for hepatic Elovl6 in the regulation of insulin

signaling. Elovl6 is linked to the generation of ceramide species that activate PP2A by disrupting interactions with its endogenous inhibitor I2PP2A. Ceramides are bioactive sphingolipids, mainly composed of a sphingosine backbone and FA chains of variable length and saturation (26, 41). Several studies have indicated indicate that specific ceramide species possess distinct physiologic activities (24, 25, 42). In particular, C16:0-ceramide appears to have a critical role in the pathophysiology of insulin resistance. For example, mice with global or liver-specific *CerS6* knockout exhibit a lower C16:0-ceramide concentration and are protected against diet-induced obesity, insulin resistance, and adipose tissue inflammation (25). A complementary paper found that heterozygous *CerS2* knockout mice exhibit high C16:0-ceramide concentrations, hepatosteatosis, glucose intolerance, and insulin resistance (24). The present findings suggest that hepatic Elovl6 deficiency increases insulin sensitivity by reducing C18:0-ceramide concentration, which maintains the inhibition of PP2A by I2PP2A, thereby increasing Akt activity, a key insulin signaling intermediate. Consistent with this notion, an important role of ceramide(d18:1/18:0) in the development of insulin resistance has been demonstrated in several studies. In mice, increasing acid ceramidase expression in the liver reduces the concentrations of C16:0- and C18:0-ceramides and improves insulin action, implying that these ceramide species may inhibit insulin

signaling (42). Luukkonen et al. have recently reported that ceramide(d18:1/18:0) is among the species that are present in significantly higher concentrations in the livers of patients with high homeostasis model assessment-insulin resistance, and are most strongly associated with insulin resistance (43). Moreover, studies in humans have shown that plasma ceramide(d18:1/18:0) concentration is significantly higher and is strongly associated with T2D and prediabetes (44, 45). Overall, these results strongly suggest that C18:0-ceramide suppresses insulin sensitivity. We believe that the present findings regarding Elovl6 contribute to understanding the molecular mechanisms that mediate these associations.

Hepatic Pnpla3 is expressed predominantly in hepatocytes, in which it is found on the ER and LD membrane (38, 46). *In vitro* studies have demonstrated that purified recombinant human PNPLA3 catalyzes the hydrolysis of the three major glycerolipids, TAGs, diacylglycerols, and monoacylglycerols, but is most effective with respect to TAGs (38, 47, 48). A recent *in vitro* study also suggested that Pnpla3 alters the TAG and PL composition of LDs by catalyzing the transfer of very long-chain PUFAs from TAGs to PLs (20). The present results suggest that Pnpla3 is involved in the synthesis of ceramides *in vivo*.

In addition to the ER, our results identify the ER-LD interface as a source of ceramides, and C18:0-ceramide generation is mainly catalyzed by CerS4 in the liver (26, 33). The co-overexpression of Pnpla3 and CerS4 in HEK293 cells suggested that Pnpla3 modifies ceramide FA composition by forming an enzyme complex with CerS4 at the ER-LD interface. Consistent with this result, Senkal *et al*. recently reported that CerSs localize to LDs and form a multi-enzyme complex with acyl-CoA synthetase long-chain family member 5 and diacylglycerol O-acyltransferase 2 at the ER-LD interface, where they generate acylceramides from ceramides and fatty acyl-CoAs (49). Therefore, it is possible that the regulation of ceramide species by Pnpla3 may be facilitated by the release of FAs from hepatic LDs. Pnpla3 is a TAG hydrolase that acts at the surface of LDs, where it releases FAs from TAGs, making them available for incorporation into ceramides. This possibility is supported by a lipidomic study of *ob/ob* mice showing an association between greater deposition of TAG species in the liver and a proportional increase in hepatic ceramide(d18:1/18:0) content (50).

Overall, the results of the present study demonstrate that liver-specific deletion of Elovl6 enhances insulin sensitivity in mice by reducing the generation of ceramides

involved in the endogenous activation of PP2A. Although we cannot rule out the possibility that Elovl6 deficiency affects the acyl-chain composition of other lipids that regulate hepatic insulin sensitivity given that our lipidomic platform did not determine the fatty acyl constituents, positional isomers, or double bond positions in the lipid fractions containing PLs, TAGs, and diacylglycerols, the present results strongly suggest that C18:0-ceramide is important in the regulation of insulin sensitivity in lipogenic conditions. Our observations linking Elovl6 and ceramides could thus provide new insight into the pathophysiology of insulin resistance and suggest that inhibition of Elovl6 may represent a therapeutic target for the amelioration of insulin resistance.

ACKNOWLEDGMENTS

We are grateful to Drs. Akio Hayashi and Katsuya Kishikawa for their helpful comments. We also thank Katsuko Okubo and Chizuko Fukui for technical assistance, and the members of our laboratories for discussion and helpful comments on the manuscript.

REFERENCES

1. Cohen JC, Horton JD, Hobbs HH. Human fatty liver disease: old questions and new insights. Science 2011;332:1519-1523.

2. Bugianesi E, McCullough AJ, Marchesini G. Insulin resistance: a metabolic pathway to chronic liver disease. Hepatology 2005;42:987-1000.

3. Utzschneider KM, Kahn SE. Review: The role of insulin resistance in nonalcoholic fatty liver disease. J Clin Endocrinol Metab 2006;91:4753-4761.

4. Michelotti GA, Machado MV, Diehl AM. NAFLD, NASH and liver cancer. Nat Rev Gastroenterol Hepatol 2013;10:656-665.

5. Younossi Z, Anstee QM, Marietti M, Hardy T, Henry L, Eslam M, George J, et al. Global burden of NAFLD and NASH: trends, predictions, risk factors and prevention. Nat Rev Gastroenterol Hepatol 2018;15:11-20.

6. Postic C, Girard J. Contribution of de novo fatty acid synthesis to hepatic steatosis and insulin resistance: lessons from genetically engineered mice. J Clin Invest 2008;118:829-838.

7. Petersen MC, Shulman GI. Mechanisms of Insulin Action and Insulin Resistance. Physiol Rev 2018;98:2133-2223.

8. Shimano H, Sato R. SREBP-regulated lipid metabolism: convergent physiology

- divergent pathophysiology. Nat Rev Endocrinol 2017;13:710-730.

9. Petersen MC, Vatner DF, Shulman GI. Regulation of hepatic glucose metabolism in health and disease. Nat Rev Endocrinol 2017;13:572-587.

10. Guillou H, Zadravec D, Martin PG, Jacobsson A. The key roles of elongases and desaturases in mammalian fatty acid metabolism: Insights from transgenic mice. Prog Lipid Res 2010;49:186-199.

11. Moon YA, Shah NA, Mohapatra S, Warrington JA, Horton JD. Identification of a mammalian long chain fatty acyl elongase regulated by sterol regulatory element-binding proteins. J Biol Chem 2001;276:45358-45366.

12. Matsuzaka T, Shimano H, Yahagi N, Yoshikawa T, Amemiya-Kudo M, Hasty AH, Okazaki H, et al. Cloning and characterization of a mammalian fatty acyl-CoA elongase as a lipogenic enzyme regulated by SREBPs. J Lipid Res 2002;43:911-920.

13. Matsuzaka T, Shimano H, Yahagi N, Kato T, Atsumi A, Yamamoto T, Inoue N, et al. Crucial role of a long-chain fatty acid elongase, Elovl6, in obesity-induced insulin resistance. Nat Med 2007;13:1193-1202.

14. Moon YA, Ochoa CR, Mitsche MA, Hammer RE, Horton JD. Deletion of ELOVL6 blocks the synthesis of oleic acid but does not prevent the

development of fatty liver or insulin resistance. J Lipid Res 2014;55:2597-2605.

15. Horton JD, Goldstein JL, Brown MS. SREBPs: activators of the complete program of cholesterol and fatty acid synthesis in the liver. J Clin Invest 2002;109:1125-1131.

16. Kienesberger PC, Oberer M, Lass A, Zechner R. Mammalian patatin domain containing proteins: a family with diverse lipolytic activities involved in multiple biological functions. J Lipid Res 2009;50 Suppl:S63-68.

17. Bruschi FV, Tardelli M, Claudel T, Trauner M. PNPLA3 expression and its impact on the liver: current perspectives. Hepat Med 2017;9:55-66.

18. Li JZ, Huang Y, Karaman R, Ivanova PT, Brown HA, Roddy T, Castro-Perez J, et al. Chronic overexpression of PNPLA3I148M in mouse liver causes hepatic steatosis. J Clin Invest 2012;122:4130-4144.

19. Ruhanen H, Perttila J, Holtta-Vuori M, Zhou Y, Yki-Jarvinen H, Ikonen E, Kakela R, et al. PNPLA3 mediates hepatocyte triacylglycerol remodeling. J Lipid Res 2014;55:739-746.

20. Mitsche MA, Hobbs HH, Cohen JC. Patatin-like phospholipase domain-containing protein 3 promotes transfer of essential fatty acids from triglycerides to phospholipids in hepatic lipid droplets. J Biol Chem

2018;293:9232.

21. Chavez JA, Summers SA. A ceramide-centric view of insulin resistance. Cell Metab 2012;15:585-594.

22. Chaurasia B, Summers SA. Ceramides - Lipotoxic Inducers of Metabolic Disorders. Trends Endocrinol Metab 2015;26:538-550.

23. Petersen MC, Shulman GI. Roles of Diacylglycerols and Ceramides in Hepatic Insulin Resistance. Trends Pharmacol Sci 2017;38:649-665.

24. Raichur S, Wang ST, Chan PW, Li Y, Ching J, Chaurasia B, Dogra S, et al. CerS2 Haploinsufficiency Inhibits beta-Oxidation and Confers Susceptibility to Diet-Induced Steatohepatitis and Insulin Resistance. Cell Metab 2014;20:919.

25. Turpin SM, Nicholls HT, Willmes DM, Mourier A, Brodesser S, Wunderlich CM, Mauer J, et al. Obesity-induced CerS6-dependent C16:0 ceramide production promotes weight gain and glucose intolerance. Cell Metab 2014;20:678-686.

26. Wegner MS, Schiffmann S, Parnham MJ, Geisslinger G, Grosch S. The enigma of ceramide synthase regulation in mammalian cells. Prog Lipid Res 2016;63:93-119.

27. Oaks J, Ogretmen B. Regulation of PP2A by Sphingolipid Metabolism and

Signaling. Front Oncol 2014;4:388.

28. Seshacharyulu P, Pandey P, Datta K, Batra SK. Phosphatase: PP2A structural importance, regulation and its aberrant expression in cancer. Cancer Lett 2013;335:9-18.

29. Li M, Makkinje A, Damuni Z. The myeloid leukemia-associated protein SET is a potent inhibitor of protein phosphatase 2A. J Biol Chem 1996;271:11059-11062.

30. Mukhopadhyay A, Saddoughi SA, Song P, Sultan I, Ponnusamy S, Senkal CE, Snook CF, et al. Direct interaction between the inhibitor 2 and ceramide via sphingolipid-protein binding is involved in the regulation of protein phosphatase 2A activity and signaling. FASEB J 2009;23:751-763.

31. Saddoughi SA, Gencer S, Peterson YK, Ward KE, Mukhopadhyay A, Oaks J, Bielawski J, et al. Sphingosine analogue drug FTY720 targets I2PP2A/SET and mediates lung tumour suppression via activation of PP2A-RIPK1-dependent necroptosis. EMBO Mol Med 2013;5:105-121.

32. Arulmozhiraja S, Matsuo N, Ishitsubo E, Okazaki S, Shimano H, Tokiwa H. Comparative Binding Analysis of Dipeptidyl Peptidase IV (DPP-4) with Antidiabetic Drugs - An Ab Initio Fragment Molecular Orbital Study. PLoS One

2016;11:e0166275.

33. Laviad EL, Albee L, Pankova-Kholmyansky I, Epstein S, Park H, Merrill AH, Jr., Futerman AH. Characterization of ceramide synthase 2: tissue distribution, substrate specificity, and inhibition by sphingosine 1-phosphate. J Biol Chem 2008;283:5677-5684.

34. Samuel VT. Fructose induced lipogenesis: from sugar to fat to insulin resistance. Trends Endocrinol Metab 2011;22:60-65.

35. Sanders FW, Griffin JL. De novo lipogenesis in the liver in health and disease: more than just a shunting yard for glucose. Biol Rev Camb Philos Soc 2016;91:452-468.

36. Ter Horst KW, Serlie MJ. Fructose Consumption, Lipogenesis, and Non-Alcoholic Fatty Liver Disease. Nutrients 2017;9.

37. Kumadaki S, Matsuzaka T, Kato T, Yahagi N, Yamamoto T, Okada S, Kobayashi K, et al. Mouse Elovl-6 promoter is an SREBP target. Biochem Biophys Res Commun 2008;368:261-266.

38. Huang Y, He S, Li JZ, Seo YK, Osborne TF, Cohen JC, Hobbs HH. A feed-forward loop amplifies nutritional regulation of PNPLA3. Proc Natl Acad Sci U S A 2010;107:7892-7897.

39. Dubuquoy C, Robichon C, Lasnier F, Langlois C, Dugail I, Foufelle F, Girard J, et al. Distinct regulation of adiponutrin/PNPLA3 gene expression by the transcription factors ChREBP and SREBP1c in mouse and human hepatocytes. J Hepatol 2011;55:145-153.

40. Rong X, Wang B, Palladino EN, de Aguiar Vallim TQ, Ford DA, Tontonoz P. ER phospholipid composition modulates lipogenesis during feeding and in obesity. J Clin Invest 2017;127:3640-3651.

41. Hannun YA. Functions of ceramide in coordinating cellular responses to stress. Science 1996;274:1855-1859.

42. Xia JY, Holland WL, Kusminski CM, Sun K, Sharma AX, Pearson MJ, Sifuentes AJ, et al. Targeted Induction of Ceramide Degradation Leads to Improved Systemic Metabolism and Reduced Hepatic Steatosis. Cell Metab 2015;22:266-278.

43. Luukkonen PK, Zhou Y, Sadevirta S, Leivonen M, Arola J, Oresic M, Hyotylainen T, et al. Hepatic ceramides dissociate steatosis and insulin resistance in patients with non-alcoholic fatty liver disease. J Hepatol 2016;64:1167-1175.

44. Wigger L, Cruciani-Guglielmacci C, Nicolas A, Denom J, Fernandez N,

Fumeron F, Marques-Vidal P, et al. Plasma Dihydroceramides Are Diabetes Susceptibility Biomarker Candidates in Mice and Humans. Cell Rep 2017;18:2269-2279.

45. Hilvo M, Salonurmi T, Havulinna AS, Kauhanen D, Pedersen ER, Tell GS, Meyer K, et al. Ceramide stearic to palmitic acid ratio predicts incident diabetes. Diabetologia 2018;61:1424-1434.

46. Hoekstra M, Li Z, Kruijt JK, Van Eck M, Van Berkel TJ, Kuiper J. The expression level of non-alcoholic fatty liver disease-related gene PNPLA3 in hepatocytes is highly influenced by hepatic lipid status. J Hepatol 2010;52:244-251.

47. He S, McPhaul C, Li JZ, Garuti R, Kinch L, Grishin NV, Cohen JC, et al. A sequence variation (I148M) in PNPLA3 associated with nonalcoholic fatty liver disease disrupts triglyceride hydrolysis. J Biol Chem 2010;285:6706-6715.

48. Pingitore P, Pirazzi C, Mancina RM, Motta BM, Indiveri C, Pujia A, Montalcini T, et al. Recombinant PNPLA3 protein shows triglyceride hydrolase activity and its I148M mutation results in loss of function. Biochim Biophys Acta 2014;1841:574-580.

49. Senkal CE, Salama MF, Snider AJ, Allopenna JJ, Rana NA, Koller A, Hannun

YA, et al. Ceramide Is Metabolized to Acylceramide and Stored in Lipid Droplets. Cell Metab 2017;25:686-697.

50. Yetukuri L, Katajamaa M, Medina-Gomez G, Seppanen-Laakso T, Vidal-Puig A, Oresic M. Bioinformatics strategies for lipidomics analysis: characterization of obesity related hepatic steatosis. BMC Syst Biol 2007;1:12.

FIGURE LEGENDS

Figure 1. Deletion of *Elovl6* in the liver increases insulin sensitivity in lipogenic diet-fed mice

(**A**) Hepatic TAG and T-Cho concentrations in 12-week-old male Flox and LKO mice fed normal chow or HSD for 14 days (n = 9–14 per group). (**B**) Hepatic FA composition in Flox and LKO mice fed a chow or HSD for 14 days (n = 5 per group). (**C**) Plasma concentrations of glucose and insulin in Flox and LKO mice fed a chow or HSD for 14 days (n = 14–25 per group). (**D**) Plasma glucose and insulin concentrations and AUCs of glucose during OGTTs in Flox and LKO mice fed a chow or HSD for 14 days (n = 24–26 per group). (**E**) Plasma glucose concentrations and AUCs during ITTs in Flox and LKO mice fed an HSD for 14 days (0.5 U insulin/kg, n = 14–19 per group). (**F**)

Immunoblot analysis of the insulin signaling in response to a bolus injection of insulin in the livers of Flox and LKO mice fed an HSD for 14 days. The results were quantified by densitometry (n = 3 per group). *$p < 0.05$, **$p < 0.01$, ***$p < 0.001$.

Figure 2. Reduction in hepatic Pnpla3 expression is involved in the higher insulin sensitivity of LKO mice

(**A**) Heatmap representation of the differentially expressed transcripts identified using microarray in the livers of HSD-fed Flox and LKO mice. Arbitrary signal intensity acquired from the microarray analysis is represented by colors (n = 3 per group). (**B**) Pathways that were significantly affected by hepatic Elovl6 deficiency. Significantly enriched ($p < 0.01$) metabolic pathways identified using the KEGG database are shown. (**C**) mRNA expression of *Elovl6*, *Srebf1c*, and *Pnpla3* in the livers of Flox and LKO mice fed a chow or HSD for 14 days (n = 15–29 per group). **$p < 0.01$, ***$p < 0.001$. (**D**) Adenovirus-mediated restoration of Pnpla3 expression in the livers of LKO mice. Immunoblot analysis of Pnpla3 expression in the livers of Flox and LKO mice infected with adenovirus encoding GFP (Ad-GFP) or Pnpla3 (Ad-Pnpla3). Twelve-week-old male Flox and LKO mice were fed an HSD for 7 days, then infected with Ad-GFP or Ad-Pnpla3. After adenovirus infection, the mice were fed an HSD for 7 days. (**E**)

Plasma glucose concentrations and AUCs during ITTs in Flox and LKO mice infected with either Ad-GFP or Ad-Pnpla3 (0.5 U insulin/kg, n = 12–17 per group). *$p < 0.05$, **$p < 0.01$ for LKO Ad-GFP vs. Flox Ad-GFP mice. #$p < 0.05$, ##$p < 0.01$ for LKO Ad-Pnpla3 vs. LKO Ad-GFP mice. (**F**) Immunoblot analysis of the insulin signaling pathway in response to a bolus injection of insulin in the livers of Flox and LKO mice infected with either Ad-GFP or Ad-Pnpla3. The results were quantified by densitometry (n = 5 per group). *$p < 0.05$, **$p < 0.01$.

Figure 3. Hepatic insulin sensitivity is associated with changes in the ceramide profile and PP2A activity

(**A**) Heatmap of the liver lipidomic analysis of HSD-fed Flox and LKO mice infected with either Ad-GFP or Ad-Pnpla3. The heatmap shows metabolites that were significantly altered by Elovl6 deficiency or Ad-Pnpla3 infection. The relative content is indicated by the color. (**B, C**) LC-MS/MS analysis of liver ceramide species from Flox and LKO mice fed a chow diet or HSD (n = 5 or 6 per group, **B**), or infected with either Ad-GFP or Ad-Pnpla3 (n = 3–6 per group, **C**). The indicated molecular species were confirmed by product ion scanning. (**D**) The hepatic PP2A activity of Flox and LKO mice fed a normal chow or HSD (n = 6–9 per group) or infected with either Ad-GFP

(GFP) or Ad-Pnpla3 (P3, n = 5–7 per group). The phosphatase activity of the immunoprecipitated PP2A was quantified using a phosphatase activity assay. (**E**) Immunoblot analysis of phosphorylated PKCζ and total PKCζ in the livers of Flox and LKO mice fed a normal chow or HSD. The ratio of phosphorylated to total PKCζ was determined by densitometry (n = 4 per group). *$p < 0.05$, **$p < 0.01$, ***$p < 0.001$.

Figure 4. Ceramide(d18:1/18:0) inhibits the I2PP2A–PP2A interaction and insulin-induced phosphorylation of Akt in HepG2 cells

(**A**) Immunoblot analysis of Akt phosphorylation in response to insulin treatment of HepG2 cells pretreated with ceramide(d18:1/16:0), ceramide(d18:1/18:0), ceramide(d18:1/20:0), or vehicle. Cells were pretreated with media containing vehicle or 10 μM ceramide for 4 h before insulin stimulation. The ratio of phosphorylated to total Akt was determined using densitometry (n = 6 per group). (**B**) Effect of ceramide species on the interaction between PP2A and I2PP2A. HepG2 cells were incubated with the indicated ceramide for 4 h. The PP2A–I2PP2A interaction was determined by immunoprecipitation using an anti-FLAG antibody, followed by immunoblotting using anti-HA and anti-FLAG antibodies. The PP2A–I2PP2A interaction was quantified using densitometry (n = 6 per group). (**C**) Effect of I2PP2A knockdown on insulin-induced

Akt phosphorylation in HepG2 cells treated with 10 mM ceramide for 4 h. The ratio of phosphorylated to total Akt was determined using densitometry (n = 5 per group). (**D**) Molecular docking simulations of ceramide(d18:1/16:0), ceramide(d18:1/18:0), and ceramide(d18:1/20:0) with I2PP2A, and van der Waals interaction energy between the ceramides and amino acid residues of I2PP2A. Hydrophobic and hydrophilic residues are shown in red and blue, respectively. *$p < 0.05$, **$p < 0.01$, ***$p < 0.001$.

Figure 5. CerS4 interacts with Elovl6 and Pnpla3

HEK293 cells were transfected with FLAG-tagged Elovl6, HA-tagged Pnpla3, and (or) V5-tagged CerS4. (**A**) Co-localizations of Elovl6-FLAG with CerS4-V5, Pnpla3-HA with CerS4-V5, and Elovl6-FLAG with Pnpla3-HA were identified using confocal microscopy. Scale bar = 10 μm. (**B**) Interactions among Elovl6, Pnpla3, and CerS4 determined by immunoblotting after immunoprecipitation using the indicated antibodies.

Figure 6. Hepatic deletion of Elovl6 ameliorates insulin resistance in *ob/ob* mice

(**A**) Body, liver, and eWAT weights of 12-week-old Flox, *ob/ob*, and *ob/ob*-LKO mice (n = 17−25 per group). (**B**) Plasma glucose and insulin concentrations of 12-week-old

Flox, *ob/ob*, and *ob/ob*-LKO (n = 17–25 per group). (**C**) Plasma glucose concentration during OGTTs (n = 14–22 per group) and ITTs (2.0 U insulin/kg, n = 10 or 11 per group), and AUCs during the ITT (n = 10 or 11 per group) in 12-week-old Flox, *ob/ob*, and *ob/ob*-LKO mice. (**D**) qPCR analysis of genes involved in DNL in livers of Flox, *ob/ob*, and *ob/ob*-LKO mice (n = 16–21 per group). (**E**) LC-MS/MS analysis of liver ceramide species from Flox, *ob/ob*, and *ob/ob*-LKO mice. The indicated molecular species were confirmed by product ion scanning (n = 3 or 4 per group). (**F**) Liver PP2A activity of Flox, ob/ob, and ob/ob-LKO mice (n = 5 or 6 per group). *$p < 0.05$, **$p < 0.01$, ***$p < 0.001$.

Figure 7. Schematic description of the Elovl6/Pnpla3/CerS pathway regulating hepatic insulin signaling

Excess consumption of carbohydrate and hyperinsulinemia activate *de novo* lipogenesis and upregulate the expression of Elovl6 and Pnpla3 in the liver. Activation of Elovl6 increases the amount of C18:0, enhancing C18:0-ceramide production through formation of an enzyme complex with CerS4 on the ER. Pnpla3 acts on the surface of LDs, releases FAs from TAGs, and modifies ceramide FA composition by forming an enzyme complex with CerS4 at the ER-LD interface. Both Elovl6 and Pnpla3 are linked

to the generation of C18:0-ceramide, which activates PP2A by disrupting the interactions with its endogenous inhibitor I2PP2A. As a consequence, PP2A inhibits insulin signaling by impairing Akt activation.

Manuscript ID: HEP-19-1048

Hepatocyte Elovl6 determines ceramide acyl-chain length and hepatic insulin sensitivity in mice

Takashi Matsuzaka[1,2], Motoko Kuba[1], Saori Koyasu[1], Yuta Yamamoto[3], Kaori Motomura[1], Sundaram Arulmozhiraja[3], Hiroshi Ohno[1], Rahul Sharma[1], Takuya Shimura[1], Yuka Okajima[1], Song-iee Han[1], Yuichi Aita[1], Yuhei Mizunoe[1], Yoshinori Osaki[1], Hitoshi Iwasaki[1], Shigeru Yatoh[1], Hiroaki Suzuki[1], Hirohito Sone[4], Yoshinori Takeuchi[1], Naoya Yahagi[1], Takafumi Miyamoto[1,2], Motohiro Sekiya[1], Yoshimi Nakagawa[1,5], Masatsugu Ema[6], Satoru Takahashi[2,5,7,8,9], Hiroaki Tokiwa[3], and Hitoshi Shimano[1,5,8,10] *

Emails

t-matsuz@md.tsukuba.ac.jp, motokoamiki@gmail.com, sao_kys@yahoo.co.jp, 17lb019f@rikkyo.ac.jp, korm013730@md.tsukuba.ac.jp, raja@rikkyo.ac.jp, hohno@md.tsukuba.ac.jp, s1430593@u.tsukuba.ac.jp, s1830411@s.tsukuba.ac.jp, s1430456@u.tsukuba.ac.jp, shan@md.tsukuba.ac.jp, metabmetabmetab@gmail.com,

ymizunoe@md.tsukuba.ac.jp, oosaki-tuk@umin.ac.jp, iwasaki@md.tsukuba.ac.jp,

shigeru.yatoh@md.tsukuba.ac.jp, hirosuzu@md.tsukuba.ac.jp, sone@med.niigata-u.ac.jp,

yoshinori-takeuchi@umin.ac.jp, nyahagi-tky@umin.ac.jp, takmi565@md.tsukuba.ac.jp,

msekiya@md.tsukuba.ac.jp, yosshy@md.tsukuba.ac.jp, mema@belle.shiga-med.ac.jp,

satoruta@md.tsukuba.ac.jp, tokiwa@rikkyo.ac.jp, hshimano@md.tsukuba.ac.jp

Affiliations

[1]Department of Internal Medicine (Endocrinology and Metabolism), Faculty of Medicine, University of Tsukuba, 1-1-1 Tennodai, Tsukuba, Ibaraki 305-8575, Japan

[2]Transborder Medical Research Center, University of Tsukuba, 1-1-1 Tennodai, Tsukuba, Ibaraki 305-8575, Japan

[3]Department of Chemistry, Rikkyo University, Nishi-Ikebukuro, Toshima, Tokyo 171-8501, Japan

[4]Department of Internal Medicine, Faculty of Medicine, Niigata University, 1-754 Asahimachi, Niigata 951-8510, Japan

[5]International Institute for Integrative Sleep Medicine (WPI-IIIS), University of Tsukuba, 1-1-1 Tennodai, Tsukuba, Ibaraki 305-8575, Japan

[6]Department of Stem Cells and Human Disease Models, Research Center for Animal Life Science, Shiga University of Medical Science, Seta, Tsukinowa-cho, Otsu, Shiga 520-2192, Japan

[7]Department of Anatomy and Embryology, Faculty of Medicine, University of Tsukuba, 1-1-1 Tennodai, Tsukuba, Ibaraki 305-8575, Japan

[8]Life Science Center for Survival Dynamics, Tsukuba Advanced Research Alliance (TARA), University of Tsukuba, 1-1-1 Tennodai, Tsukuba, Ibaraki 305-8575, Japan

[9]Laboratory Animal Resource Center (LARC), University of Tsukuba, 1-1-1 Tennodai, Tsukuba, Ibaraki 305-8575, Japan

[10]AMED-CREST, Japan Agency for Medical Research and Development (AMED), 1-7-1, Ohte-machi, Chiyoda-ku, Tokyo, 100-0004, Japan

Keywords

Non-alcoholic fatty liver disease

Fatty acid

Lipogenesis

Patatin-like phospholipase domain-containing protein 3

Protein phosphatase 2A

Contact information

* Correspondence to: Hitoshi Shimano, MD, Ph.D.

Department of Internal Medicine (Endocrinology and Metabolism), Faculty of Medicine, University of Tsukuba, 1-1-1 Tennodai, Tsukuba, Ibaraki 305-8575, Japan.

Tel. and Fax: +81-29-863-2081; E-mail: hshimano@md.tsukuba.ac.jp

Abbreviations

NAFLD, non-alcoholic fatty liver disease; T2D, type 2 diabetes; Elovl6, ELOVL fatty acid elongase 6; FA, fatty acid; LKO, liver-specific Elovl6 knockout; HSD, high-sucrose diet; Pnpla3, patatin-like phospholipase domain-containing protein 3; PP2A, protein phosphatase 2A; CerS4, ceramide synthase 4; ER, endoplasmic reticulum; LD, lipid droplet; TAG, triacylglycerol; NASH, non-alcoholic steatohepatitis; DNL, *de novo* lipogenesis; GKO, global deletion of *Elovl6*; HFHS, high-fat and high-sucrose; LC-MS/MS, liquid chromatography coupled with tandem mass spectrometry; DMEM, Dulbecco's Modified Eagle's Medium; T-Cho, total cholesterol; eWAT, epididymal white adipose tissue; AUC, area under the curve; IR, insulin receptor; IRS, insulin receptor substrate; PKC, protein kinase C; GSK3, glycogen synthase kinase 3; PRAS40, proline-rich Akt substrate of 40 kDa; qPCR, quantitative real-time

PCR; Srebf1c, sterol regulatory element binding protein 1c; ACC, acetyl-CoA carboxylase; Fasn, fatty acid synthase; Scd, stearoyl-CoA desaturase; GFP, green fluorescent protein; PL, phospholipid; I2PP2A, Inhibitor 2 of PP2A; shRNA, short hairpin RNA.

Financial support

This work was supported by AMED-CREST from the Japan Agency for Medical Research and Development, AMED (to H.S.); Grants-in-Aid for Scientific Research (A) 15H02541 (to H.S.), Scientific Research (A) 18H04051, Scientific Research on Innovative Areas 17H06395 (to H.S.), Scientific Research (B) 15H03093 (to T.M.), Scientific Research (B) 18H03189 (to T.M.), and Program to Disseminate Tenure Tracking System (to T.M.) from the Ministry of Science, Education, Culture, and Technology of Japan; Front Runner of Future Diabetes Research from Japan Foundation for Applied Enzymology (to T.M.); Ono Medical Research Foundation (to T.M.); Takeda Science Foundation (to T. M.); Mochida Memorial Foundation for Medical and Pharmaceutical Research (to T. M.); Kowa Life Science Foundation (to T. M.).

ABSTRACT

Dysfunctional hepatic lipid metabolism is a cause of non-alcoholic fatty liver disease (NAFLD), the most common chronic liver disorder worldwide, and is closely associated with insulin resistance and type 2 diabetes (T2D). ELOVL fatty acid elongase 6 (Elovl6) is responsible for converting C16 saturated and monounsaturated fatty acids (FAs) into C18 species. We have previously shown that Elovl6 contributes to obesity-induced insulin resistance by modifying hepatic C16/C18-related FA composition. To define the precise molecular mechanism by which hepatic Elovl6 affects energy homeostasis and metabolic disease, we generated liver-specific Elovl6 knockout (LKO) mice. Unexpectedly, LKO mice were not protected from high-fat diet-induced insulin resistance. Instead, LKO mice exhibited higher insulin sensitivity than controls when consuming a high-sucrose diet (HSD), which induces lipogenesis. Hepatic patatin-like phospholipase domain-containing protein 3 (Pnpla3) expression was downregulated in LKO mice, and adenoviral Pnpla3 restoration reversed the enhancement in insulin sensitivity in HSD-fed LKO mice. Lipidomic analyzes showed that the hepatic ceramide(d18:1/18:0) content was lower in LKO mice, which may explain the effect on insulin sensitivity. Ceramide(d18:1/18:0) enhances protein

phosphatase 2A (PP2A) activity by interfering with the binding of PP2A to its biological inhibitor I2PP2A, leading to Akt dephosphorylation. Its production involves the formation of an Elovl6-ceramide synthase 4 (CerS4) complex in the endoplasmic reticulum (ER) and a Pnpla3-CerS4 complex on lipid droplets (LDs). Consistent with this, liver-specific Elovl6 deletion in ob/ob mice reduced both hepatic ceramide(d18:1/18:0) and PP2A activity, and ameliorated insulin resistance. *Conclusion:* Our study demonstrates the key role of hepatic Elovl6 in the regulation of the acyl-chain composition of ceramide, and that C18:0-ceramide is a potent regulator of hepatic insulin signaling linked to Pnpla3-mediated NAFLD.

INTRODUCTION

Non-alcoholic fatty liver disease (NAFLD), characterized by excessive triacylglycerol (TAG) accumulation in hepatocytes, is recognized as a hepatic phenotype of the metabolic syndrome (1). A large majority of obese and diabetic individuals develop NAFLD, but it is also a risk factor for various other conditions, including insulin resistance, hyperlipidemia, and type 2 diabetes (T2D) (2, 3). Furthermore, non-alcoholic steatohepatitis (NASH), a severe form of NAFLD characterized by hepatocellular damage, lobular inflammation, abnormal glucose tolerance, and fibrosis, can progress to cirrhosis and hepatocellular carcinoma (4, 5).

Chronic and/or excess consumption of carbohydrates and saturated fatty acids (FAs) is associated with the development of hepatic insulin resistance (6, 7). Hepatic insulin resistance promotes aberrant glucose production, *de novo* lipogenesis (DNL), atherogenic dyslipidemia, and NAFLD, which are major risk factors for T2D and cardiovascular disease (8, 9). There are few effective therapies for hepatic insulin resistance or obesity, and the development of novel therapeutics necessitates a better understanding of the mechanistic relationship between obesity and NAFLD.

Elongation and desaturation are central steps in the *de novo* synthesis of long-chain FAs, and length and saturation are critical determinants of FA function and metabolic fate (10). ELOVL fatty acid elongase 6 (Elovl6) is a microsomal enzyme that is involved in the elongation of C16 saturated and monounsaturated FAs to form C18 FAs (11, 12). Loss of Elovl6 function reduces stearate (C18:0) and oleate (C18:1n-9) concentrations but increases palmitate (C16:0), palmitoleate (C16:1n-7), and vaccinate (C18:1n-7) concentrations (13, 14). We have previously reported that mice with global deletion of *Elovl6* (GKO) are protected against insulin resistance when fed a high-fat and high-sucrose (HFHS) diet or when mated to leptin-deficient *ob/ob* mice because the hepatic FA composition is modified (13). In the present study, we generated liver-specific *Elovl6* knockout (LKO) mice to investigate the role of Elovl6 in the hepatic control of lipid metabolism and energy homeostasis.

MATERIALS AND METHODS

Animals.

All animal husbandry and experimental protocols complied with institutional guidelines

and were approved by the Animal Experiment Committee of the University of Tsukuba. The mice were housed in specific pathogen-free conditions under a 12-h light/dark cycle, with free access to water and either standard chow (MF; Oriental Yeast, Tokyo, Japan) or a HFHS diet (F2HFHSD; Oriental Yeast, Tokyo, Japan) or a high-sucrose diet high-sucrose diet (HSD; D11725; Research Diets, New Jersey, USA) in the Laboratory Animal Resource Center at the University of Tsukuba. The detailed dietary composition of the HFHS diet and HSD is shown in Supporting Table 1.

Lipidomic profiling.

The MxP® Lipids platform (Metanomics Health GmbH, Berlin, Germany) was used for the entire lipid analysis workflow as described in the Online Materials and Methods.

Statistical analysis.

Values are expressed as mean ± SEM. Student's t-tests were used to compare the means of two groups and one-way ANOVA was used for multiple group mean comparisons. All analyzes were performed using GraphPad Prism 5 (GraphPad Software Inc., CA, USA), and $p < 0.05$ (two-tailed) was considered to represent statistical significance.

RESULTS

LKO mice are not protected from HFHS diet-induced insulin resistance

We generated LKO mice by crossing Elovl6 lox/lox mice with albumin promoter-Cre transgenic mice, which express Cre exclusively in postpartum hepatocytes (Supporting Figure 1). To determine whether liver-specific *Elovl6* deletion produces the same metabolic phenotype as that of GKO mice (13), Flox and LKO mice were fed a normal chow or HFHS diet from 8 weeks of age. There were no differences in body weight (Supporting Figure 2A), liver weights (Supporting Figure 2B), or hepatic TAG or total cholesterol (T-Cho) concentrations (Supporting Figure 2C) between Flox and LKO mice on either a chow or HFHS diet. Epididymal white adipose tissue (eWAT) weight was slightly but significantly lower in LKO mice than in Flox mice on an HFHS diet (Supporting Figure 2B). In contrast to GKO, however, liver-specific Elovl6 deletion did not reduce plasma glucose or insulin concentrations in mice on an HFHS diet (Supporting Figure 2D). Moreover, oral glucose tolerance tests (OGTTs; Supporting Figure 2E) and insulin tolerance tests (ITTs; Supporting Figure 2F) showed no significant differences between Flox and LKO mice fed an HFHS diet. These results

demonstrate that hepatocyte-specific *Elovl6* deficiency is insufficient to ameliorate insulin resistance induced by an HFHS diet.

Insulin sensitivity is higher in LKO mice fed a lipogenic diet

We next fed Flox and LKO mice an HSD for 14 days to induce Elovl6 activity and DNL, which revealed several phenotypic differences. On the HSD diet, there were no differences in body, liver and eWAT weights (Supporting Figure 3A), or in plasma lipid concentrations (Supporting Figure 3B) between Flox and LKO mice. The HSD induced a similar degree of hepatosteatosis, as demonstrated by increases in hepatic TAG and T-Cho concentrations (Figure 1A) and number of lipid droplets (LDs) (Supporting Figure 3C) in both genotypes, compared to the chow diet. Furthermore, *Elovl6* deletion exacerbated the changes in hepatic FA composition induced by HSD feeding. Specifically, HSD feeding of LKO mice significantly lowered the stearate and oleate content, but increased the palmitate, palmitoleate, and vaccinate content, relative to Flox mice (Figure 1B). HSD-fed LKO mice had significantly lower plasma glucose and insulin levels compared to HSD-fed Flox controls (Figure 1C). During OGTTs, HSD-fed LKO mice exhibited lower plasma glucose excursions than HSD-fed Flox mice, evidenced by a lower area under the curve (AUC; Figure 1D). Furthermore,

during ITTs, HSD-fed LKO mice demonstrated lower plasma glucose concentrations than HSD-fed Flox mice (Figure 1E). These results suggest that LKO mice are more insulin-sensitive than Flox mice when consuming an HSD.

We next evaluated insulin signaling following an intravenous injection of insulin. Insulin administration had similar effects on total insulin receptor (IR) and phospho-IR protein levels, and on the ratio of phosphorylated IR to total IR in HSD-fed Flox and LKO mouse liver (Figure 1F). We have previously shown that global *Elovl6* deficiency increases total and phosphorylated insulin receptor substrate (IRS)-2 protein levels and suppresses protein kinase C (PKC) ε activity in the liver, which at least partially explains the amelioration of diet-induced insulin resistance (13). However, the total and phosphorylated levels of IRS-1 and IRS-2 proteins (Supporting Figure 3D), and PKCε translocation to the membrane, an index of PKCε activity (Supporting Figure 3E), were not affected by LKO in the liver of HSD-fed mice. In contrast, the insulin-induced phosphorylation of Akt (Ser473, Thr308) was much higher in the livers of HSD-fed LKO mice than in those of HSD-fed Flox mice (Figure 1F). In addition, the insulin-induced phosphorylation of the Akt substrates glycogen synthase kinase 3 (GSK3) α/β (Ser21/9) and proline-rich Akt substrate of 40 kDa (PRAS40; Thr246) was

significantly higher in the livers of LKO mice than in those of Flox mice. The insulin-induced phosphorylation of Akt (Ser473) was similar in the eWAT and muscle of Flox and LKO mice (Supporting Figure 3F). These data demonstrate that the higher insulin sensitivity in HSD-fed LKO mice is mediated through an enhancement in the hepatic insulin signaling *via* Akt.

Dietary lipids do not normalize the higher insulin sensitivity in HSD-fed LKO mice

Because stearate and oleate content was lower in the liver of LKO mice, we wished to determine whether dietary supplementation with these FAs could reverse the increase in insulin sensitivity identified in HSD-fed LKO mice. We therefore supplemented the HSD with 20% by mass of both tristearin and triolein. However, after 14 days on a diet supplemented with stearate and oleate, LKO mice demonstrated greater insulin sensitivity, as evaluated using an ITT (Supporting Figure 4A), suggesting that FA(s) endogenously synthesized by Elovl6 are involved in the regulation of hepatic insulin sensitivity.

LKO mice demonstrate an altered hepatic gene expression profile

To identify candidate genes associated with the enhancement in hepatic insulin

sensitivity in HSD-fed LKO mice, livers from Flox and LKO mice fed an HSD were profiled using microarray analysis. The heatmap in Figure 2A and Supporting Table 2 list all the genes with significant differences in expression *versus* controls. Pathway analysis revealed highly significant downregulation of eight pathways involved in lipid metabolism (Figure 2B). We next performed quantitative real-time PCR (qPCR) analysis to confirm the major findings of the microarray analysis, and found that liver-specific Elovl6 deficiency was associated with lower expression of sterol regulatory element binding protein 1c (*Srebf1c*) mRNA (Figure 2C) and the nuclear active form of SREBP-1 protein (Supporting Figure 4B), the major transcription factor involved in the transcriptional regulation of lipogenesis by carbohydrates (8, 15). Moreover, liver-specific Elovl6 deficiency significantly impaired the HSD-induced upregulation of hepatic mRNAs encoding lipogenic enzymes, such as acetyl-CoA carboxylase 1 (*Acc1*), fatty acid synthase (*Fasn*), and stearoyl-CoA desaturase 1 (*Scd1*) (Supporting Figure 4C). A volcano plot demonstrates that the genes significantly downregulated by *Elovl6* deficiency (Supporting Figure 4D) included patatin-like phospholipase domain containing 3 (*Pnpla3*), which encodes a membrane-bound protein with a predominant TAG lipase activity (16, 17). qPCR analysis confirmed that *Pnpla3* expression was increased 67-fold by HSD feeding in the liver of Flox mice and

reduced by 68% in the liver of LKO mice (Figure 2C). A similar expression pattern was also identified for the *Pnpla3* paralog *Pnpla5* (Supporting Figure 4E). In addition, we performed immunoblotting for Pnpla3 and found that its protein abundance was lower in the liver of LKO mice than in that of Flox mice (Supporting Figure 4F).

Downregulation of Pnpla3 mediates the increase in insulin sensitivity in HSD-fed LKO mice

To determine if the Pnpla3 reduction contributes to the higher insulin sensitivity in HSD-fed LKO mice, Flox and LKO mice consuming an HSD were injected with a recombinant adenovirus encoding mouse Pnpla3 (Ad-Pnpla3) or green fluorescent protein (Ad-GFP). Hepatic Pnpla3 protein was expressed at similar levels in HSD-fed Ad-Pnpla3-infected LKO mice and Flox mice, according to the results of immunoblotting (Figure 2D). Pnpla3 overexpression did not affect body weight, but increased liver weight to a similar extent in both Flox and LKO mice (Supporting Figure 5A). However, Pnpla3 overexpression did not affect the hepatic lipid content (Supporting Figure 5B, C) or liver pathology (Supporting Figure 5C, D) in Flox and LKO mice. Remarkably, the restoration of hepatic Pnpla3 protein expression in HSD-fed LKO mice reversed both the increase in insulin sensitivity (Figure 2E) and the

increase in the insulin-stimulated phosphorylation of hepatic Akt (Ser473, Thr308), GSK3α/β, and PRAS40 (Figure 2F). These results suggest that Elovl6- and Pnpla3-dependent lipid metabolic pathways are crucial in the regulation of hepatic insulin signaling under lipogenic conditions.

Lipid profiling of Elovl6- and Pnpla3-regulated lipids in the liver

We hypothesized that Elovl6 and Pnpla3 cooperate in the regulation of hepatic insulin sensitivity by changing the acyl-chain composition of specific lipid(s) that modulate insulin action. To test this hypothesis, we performed lipidomics on liver samples from HSD-fed Flox and LKO mice injected with either Ad-GFP or Ad-Pnpla3. Deletion of *Elov6* significantly increased the content of 39 lipid metabolites and reduced the content of 39 other lipid metabolites in the liver (Figure 3A and Supporting Table 3). These Elovl6-related changes occurred in a variety of lipids, including ceramides, cholesterol esters, FFAs, phospholipids (PLs), lysoPLs, sphingomyelins, and TAGs. Conversely, the restoration of hepatic Pnpla3 expression in LKO mice increased the content of six lipid metabolites and reduced the content of 27 metabolites in the liver (Figure 3A and Supporting Table 3). Consistent with a physiologic role of Pnpla3 in determining the TAG and PL composition of hepatic LDs (18-20), Pnpla3 expression altered the

distribution of TAG and FFA species, as well as of ceramide and sphingomyelin species. Among these, the following specific lipids exhibited changes corresponding to the effects of manipulating Elovl6 and Pnpla3. The concentration of ceramide(d18:1/18:0) was lower in LKO liver than in Flox liver and was increased by the restoration of Pnpla3 expression in LKO mice. In contrast, the concentration of ceramide(d18:2/22:1) was higher in LKO liver than in Flox liver, and was reduced by the restoration of Pnpla3 expression.

Ceramides have been implicated in the lipid-induced inhibition of insulin sensitivity (21-23). Moreover, specific ceramide species, which are defined by their fatty acyl-chain length, can have specific biologic functions (24-26). Therefore, we expanded our initial lipidomic analysis by analyzing multiple ceramide species to determine whether their hepatic concentrations are modulated by Elovl6 and Pnpla3. The total hepatic ceramide content was not significantly affected by genotype, diet, or adenovirus infection (Supporting Figure 6A), and 19 of the ceramide species evaluated were similar in abundance between the HSD-fed Flox and LKO mice (Figure 3B). However, Elovl6 deficiency significantly reduced the content of ceramide(d18:1/18:0) and ceramide(d18:2/18:0) in the liver. In contrast, restoration of Pnpla3 significantly

increased the content of ceramide(d18:1/18:0) and ceramide(d18:1/20:0), but significantly reduced the content of ceramide(d18:2/22:1) in the liver of HSD-fed LKO mice (Figure 3C). An injection of a small quantity of Pnpla3 adenovirus significantly increased the content of ceramide(d18:1/16:0) and ceramide(d18:1/18:0), and significantly reduced the content of ceramide(d18:2/22:1) in the liver of HSD-fed Flox mice. Elovl6 deficiency significantly reduced the HSD-induced increase in hepatic ceramide(d18:1/18:0), and this effect was attenuated by the restoration of Pnpla3 expression (Figure 3B, C). Thus, changes in ceramide(d18:1/18:0) concentration are strongly associated with the insulin sensitivity of LKO mice.

Ceramide(d18:1/18:0) increases PP2A activity and inhibits insulin signaling by reducing the interaction between PP2A and I2PP2A

Because ceramides are known to regulate insulin sensitivity by activating PP2A and PKCζ (21-23), we assessed the hepatic activities of PP2A and PKCζ. HSD-feeding significantly increased PP2A activity in the liver of Flox mice, but not LKO mice (Figure 3D). The restoration of hepatic Pnpla3 expression in HSD-fed LKO mice significantly increased PP2A activity to a level comparable to that of HSD-fed Flox mice (Figure 3D). We also assessed the phosphorylation status of hepatic PKCζ and

found that phosphorylation at Thr410, which is required for PKCζ activation (21), was not altered by Elovl6 deficiency or HSD-feeding (Figure 3E). These results suggest that the higher hepatic insulin sensitivity in HSD-fed LKO mice may be mediated through the suppression of C18:0-ceramide production, resulting in a reduction in ceramide-induced PP2A activity in the liver and lower PP2A-dependent downregulation of insulin signaling, implying a disinhibition of insulin signaling.

To determine whether ceramide(d18:1/18:0) inhibits insulin signaling, human hepatoma HepG2 cells were treated with 10 μM ceramide(d18:1/16:0), ceramide(d18:1/18:0), or ceramide(d18:1/20:0) for 4 h, and with vehicle or insulin for the last 10 min of this period (Figure 4A). Treatment with ceramide(d18:1/16:0) or ceramide(d18:1/20:0) did not affect insulin-stimulated phosphorylation of Akt, but ceramide(d18:1/18:0) treatment significantly suppressed the insulin-stimulated phosphorylation of Akt compared to vehicle and ceramide(d18:1/16:0) treatment.

Ceramide inhibits insulin signaling by activating PP2A, a serine/threonine phosphatase that dephosphorylates and thus deactivates Akt (27). Previous studies have demonstrated that PP2A activity is modulated by phosphorylation at Tyr307 and

carboxymethylation at Leu309 of the C subunit (28). Immunoblot analysis revealed that Elovl6 deficiency and Pnpla3 expression did not affect the levels of phosphorylation or carboxymethylation of the PP2A C subunit in the liver (Supporting Figure 6B). In addition, ceramide activates PP2A activity in part via direct binding of Inhibitor 2 of PP2A (I2PP2A/SET oncogene), which prevents the interaction between PP2A and I2PP2A (27, 29). Notably, I2PP2A preferentially binds C18-ceramides over C14–C16 ceramides (30, 31). We hypothesized that if the major effect of Elovl6 deficiency on hepatic insulin signaling is to reduce hepatic ceramide(d18:1/18:0) production, this effect would be modulated by altering I2PP2A–PP2A binding. To test this hypothesis, HepG2 cells transfected with HA-tagged PP2A catalytic subunit alpha isoform (PPP2CA) and FLAG-tagged I2PP2A were treated with ceramide(d18:1/16:0), ceramide(d18:1/18:0), or ceramide(d18:1/20:0). Ceramide(d18:1/16:0) did not change the PPP2CA–I2PP2A interaction, but ceramide(d18:1/18:0) and ceramide(d18:1/20:0) significantly inhibited the PPP2CA–I2PP2A interaction (Figure 4B). This reduction in the PPP2CA–I2PP2A interaction was much larger in ceramide(d18:1/18:0)-treated cells than in ceramide(d18:1/20:0)-treated cells.

To confirm the role of I2PP2A in ceramide(d18:1/18:0)-induced insulin resistance,

HepG2 cells were infected with lentivirus expressing a short hairpin RNA (shRNA) targeting I2PP2A or a scrambled shRNA (control). Immunoblotting confirmed a significant reduction in the abundance of I2PP2A protein following infection with the specific shRNA (Figure 4C). In HepG2 cells infected with control shRNA, ceramide(d18:1/18:0) reduced the insulin-stimulated phosphorylation of Akt (Figure 4C). Knockdown of I2PP2A reduced the insulin-stimulated phosphorylation of Akt and abrogated the inhibitory effect of ceramide(d18:1/18:0) on the insulin-stimulated phosphorylation of Akt (Figure 4C). Thus, ceramide(d18:1/18:0) inhibits Akt signaling in a I2PP2A-dependent manner to regulate PP2A activity.

To determine the structural basis of the interaction between ceramides and I2PP2A, we performed molecular modeling using the crystal structure of I2PP2A and ceramide(d18:1/16:0), ceramide(d18:1/18:0), or ceramide(d18:1/20:0) as probes, and studied their interactions quantitatively using the first-principles calculations-based fragment molecular orbital method (32). The relative binding scores, the theoretical interaction energies between each ceramide and I2PP2A, from the value of ceramide(d18:1/16:0), are shown in Figure 4D. Consistent with the biologic data, this model suggested that the binding affinity of each species to I2PP2A is in the descending

order ceramide(d18:1/18:0), ceramide(d18:1/20:0), and ceramide(d18:1/16:0). Thus, the potent effect of ceramide(d18:1/18:0) on I2PP2A–PP2A binding shown by *in vivo* and *in vitro* assays was also confirmed by a computer simulation.

Ceramide synthase (CerS) associates with Elovl6 and Pnpla3 on the endoplasmic reticulum (ER) and at the ER-LD interface, respectively

Our findings suggest that both Elovl6 and Pnpla3 are involved in metabolic pathways that regulating ceramide acyl species. *De novo* ceramide synthesis involves six distinct CerSs, CerS1 to CerS6, which are specialized for the synthesis of ceramides with different fatty acyl-chain lengths (26). Therefore, we sought to identify physical interactions among Elovl6, Pnpla3, and CerS4, a CerS that synthesizes C18–C20 ceramides and is highly expressed in the liver (33).

We first characterized the subcellular distributions of each protein in HEK293 cells using confocal microscopy. When expressed in HEK293 cells treated with oleate to increase LD formation, C-terminal FLAG-tagged Elovl6 (Elovl6-FLAG) and V5-tagged CerS4 (CerS4-V5) displayed a reticular distribution that likely corresponded to the ER (Supporting Figure 7A). Consistent with previous reports, HA-tagged Pnpla3

(Pnpla3-HA) accumulated on membranes and in LDs (Supporting Figure 7B). In co-expression experiments, Elovl6-FLAG appeared to colocalize with CerS4-V5 in the ER, while Pnpla3-HA and CerS4-V5 appeared to colocalize at the ER-LD interface upon oleate loading (Figure 5A). When co-expressed with Elovl6-FLAG, Pnpla3-HA displayed a reticular distribution, likely corresponding to the ER and LDs (Figure 5A). However, within 24 h of transfection, both Elovl6-FLAG- and Pnpla3-HA-expressing HEK293 cells were smaller and rounder, with dense cytoplasm and tightly-packed organelles, suggestive of the induction of apoptosis, which was presumably due to the greater production of C18:0-ceramide and the higher PP2A activity (27).

We next aimed to identify interactions among Elovl6, Pnpla3, and CerS4 by immunoprecipitation from co-overexpressing cells. HEK293 cells were transfected with Elovl6-FLAG and CerS4-V5, Pnpla3-HA and CerS4-V5, or Elovl6-FLAG and Pnpla3-HA, and then treated with oleate for 24 h. This confirmed the interaction of Elovl6-FLAG with CerS4-V5 (Figure 5B and Supporting Figure 8A), and Pnpla3-HA was also shown to interact with CerS4-V5 (Figure 5B and Supporting Figure 8B). However, Elovl6-FLAG did not interact with Pnpla3-HA (Figure 5B and Supporting Figure 8C). Taken together, these results suggest that Elovl6 and Pnpla3 may be

involved in regulating a pool of C18:0-ceramide by forming Elovl6-CerS4 and Pnpla3-CerS4 complexes on the ER and at the ER-LD interface, respectively.

Liver-specific deletion of *Elovl6* ameliorates insulin resistance in *ob/ob* mice

To further define the role of hepatic Elovl6 in obesity and insulin resistance, we assessed the effects of liver-specific *Elovl6* deletion in leptin-deficient *ob/ob* mice, a widely used animal model of severe obesity, steatohepatitis, and insulin resistance. Mice with liver-specific disruption of Elovl6 (*ob/ob*-LKO) were severely obese, with similar body and eWAT weight to those of *ob/ob* mice (Figure 6A). Liver weight was significantly greater in *ob/ob*-LKO mice than in *ob/ob* mice (Figure 6A), but with similar degrees of hepatosteatosis (Supporting Figure 9A–C), although there were prominent differences in FA composition (Supporting Figure 9D). Liver-specific disruption of *Elovl6* significantly reduced plasma glucose and insulin concentrations compared to *ob/ob* mice (Figure 6B). OGTTs showed that glucose intolerance was moderately ameliorated in *ob/ob*-LKO mice *versus* *ob/ob* mice (Figure 6C). Furthermore, ITTs showed that the insulin resistance was significantly less severe in *ob/ob*-LKO mice than in *ob/ob* mice (Figure 6C). The expression of lipogenic genes, including *Elovl6*, *Srebf1c*, *Fasn*, *Scd1*, and *Pnpla3*, was significantly higher in the livers

of *ob/ob* mice than in Flox mice (Figure 6D). However, *ob/ob*-LKO mice showed significantly lower hepatic expression of these lipogenic genes than *ob/ob* mice. We also quantified the relative content of representative ceramide species in the livers of Flox, *ob/ob*, and *ob/ob*-LKO mice and found that the increase in ceramide(d18:1/18:0) content in *ob/ob* mouse liver was absent in *ob/ob*-LKO mouse liver (Figure 6E). Moreover, the content of hepatic ceramide(d18:1/20:0), ceramide(d18:1/24:1), ceramide(d17:1/18:0), ceramide(d17:1/24:1), ceramide(d18:2/18:0), and ceramide(d18:2/20:0) was significantly lower, and the content of ceramide(d18:1/16:0) was significantly higher in *ob/ob*-LKO mice than in *ob/ob* mice. The activity of PP2A in the liver of *ob/ob*-LKO mice was also lower than in *ob/ob* mice (Figure 6F), which was comparable to the trend identified in Flox mice. Taking these results together, it can be concluded that hepatic Elovl6-mediated C18:0-ceramide production regulates insulin sensitivity through the modulation of PP2A activity under lipogenic conditions, and that liver-specific deletion of Elovl6 can ameliorate insulin resistance in the obese diabetic state.

DISCUSSION

In the present study, we aimed to determine the role of hepatic Elovl6-synthesized long-chain FAs in lipid metabolism and glucose homeostasis by generating liver-specific *Elovl6*-deficient mice. Our results demonstrate that hepatic Elovl6 regulates hepatic insulin sensitivity, in part by affecting the hepatic ceramide FA composition. In turn, ceramide FA composition regulates insulin signaling under lipogenic conditions by modulating the interaction between I2PP2A and PP2A, and PP2A activity. The proposed pathway is presented in Figure 7 and Supporting Figure 9E.

There is increasing evidence that diets high in carbohydrate result in greater DNL, obesity, ectopic lipid accumulation, and insulin resistance in animals, as well as in humans (23, 34–36). Hyperglycemia stimulates pancreatic insulin secretion, which, together with dietary carbohydrate, stimulates hepatic DNL by upregulating lipogenic gene transcription. The transcription factors responsible for mediating this include SREBP-1c, which regulates hepatic DNL primarily by regulating the expression of genes involved in DNL, lipid homeostasis, and glucose metabolism (8). *Elovl6* expression is highly responsive to carbohydrates and insulin, and its promoter contains

response elements for SREBP-1c (12, 37). *Pnpla3* expression is also strongly induced by carbohydrate feeding and insulin through the lipogenic transcription factors SREBP-1c and carbohydrate-response element-binding protein (38, 39). Moreover, accumulation of long-chain FAs, such as stearate and oleate, the major end-products of the SREBP-1c pathway, prevents the degradation of the Pnpla3 protein by the proteasome and stabilize it, thereby increasing its abundance (38). We found that the expression levels of *Srebf1c* and its target lipogenic genes, including *Acc1*, *Fasn*, *Scd1*, and *Pnpla3*, were collectively suppressed in the livers of HSD-fed LKO mice. How does hepatic Elovl6 regulate lipogenic gene expression? On an HSD diet, hepatic Elovl6 deficiency markedly reduced the nuclear levels of SREBP-1, indicating that hepatic Elovl6 expression and its products are required for the maturation and nuclear translocation of active SREBP-1 protein. Although the mechanism whereby Elovl6 deficiency reduces the maturation of SREBP-1 protein and *Srebf1c* mRNA expression remains to be elucidated, a recent study has suggested that the altered acyl-chain composition of PLs in the ER induced by Elovl6 deficiency may reduce SREBP-1 post-translational processing (40).

Our data demonstrate a novel role for hepatic Elovl6 in the regulation of insulin

signaling. Elovl6 is linked to the generation of ceramide species that activate PP2A by disrupting interactions with its endogenous inhibitor I2PP2A. Ceramides are bioactive sphingolipids, mainly composed of a sphingosine backbone and FA chains of variable length and saturation (26, 41). Several studies have indicated indicate that specific ceramide species possess distinct physiologic activities (24, 25, 42). In particular, C16:0-ceramide appears to have a critical role in the pathophysiology of insulin resistance. For example, mice with global or liver-specific *CerS6* knockout exhibit a lower C16:0-ceramide concentration and are protected against diet-induced obesity, insulin resistance, and adipose tissue inflammation (25). A complementary paper found that heterozygous *CerS2* knockout mice exhibit high C16:0-ceramide concentrations, hepatosteatosis, glucose intolerance, and insulin resistance (24). The present findings suggest that hepatic Elovl6 deficiency increases insulin sensitivity by reducing C18:0-ceramide concentration, which maintains the inhibition of PP2A by I2PP2A, thereby increasing Akt activity, a key insulin signaling intermediate. Consistent with this notion, an important role of ceramide(d18:1/18:0) in the development of insulin resistance has been demonstrated in several studies. In mice, increasing acid ceramidase expression in the liver reduces the concentrations of C16:0- and C18:0-ceramides and improves insulin action, implying that these ceramide species may inhibit insulin

signaling (42). Luukkonen et al. have recently reported that ceramide(d18:1/18:0) is among the species that are present in significantly higher concentrations in the livers of patients with high homeostasis model assessment-insulin resistance, and are most strongly associated with insulin resistance (43). Moreover, studies in humans have shown that plasma ceramide(d18:1/18:0) concentration is significantly higher and is strongly associated with T2D and prediabetes (44, 45). Overall, these results strongly suggest that C18:0-ceramide suppresses insulin sensitivity. We believe that the present findings regarding Elovl6 contribute to understanding the molecular mechanisms that mediate these associations.

Hepatic Pnpla3 is expressed predominantly in hepatocytes, in which it is found on the ER and LD membrane (38, 46). *In vitro* studies have demonstrated that purified recombinant human PNPLA3 catalyzes the hydrolysis of the three major glycerolipids, TAGs, diacylglycerols, and monoacylglycerols, but is most effective with respect to TAGs (38, 47, 48). A recent *in vitro* study also suggested that Pnpla3 alters the TAG and PL composition of LDs by catalyzing the transfer of very long-chain PUFAs from TAGs to PLs (20). The present results suggest that Pnpla3 is involved in the synthesis of ceramides *in vivo*.

In addition to the ER, our results identify the ER-LD interface as a source of ceramides, and C18:0-ceramide generation is mainly catalyzed by CerS4 in the liver (26, 33). The co-overexpression of Pnpla3 and CerS4 in HEK293 cells suggested that Pnpla3 modifies ceramide FA composition by forming an enzyme complex with CerS4 at the ER-LD interface. Consistent with this result, Senkal *et al*. recently reported that CerSs localize to LDs and form a multi-enzyme complex with acyl-CoA synthetase long-chain family member 5 and diacylglycerol O-acyltransferase 2 at the ER-LD interface, where they generate acylceramides from ceramides and fatty acyl-CoAs (49). Therefore, it is possible that the regulation of ceramide species by Pnpla3 may be facilitated by the release of FAs from hepatic LDs. Pnpla3 is a TAG hydrolase that acts at the surface of LDs, where it releases FAs from TAGs, making them available for incorporation into ceramides. This possibility is supported by a lipidomic study of *ob/ob* mice showing an association between greater deposition of TAG species in the liver and a proportional increase in hepatic ceramide(d18:1/18:0) content (50).

Overall, the results of the present study demonstrate that liver-specific deletion of Elovl6 enhances insulin sensitivity in mice by reducing the generation of ceramides

involved in the endogenous activation of PP2A. Although we cannot rule out the possibility that Elovl6 deficiency affects the acyl-chain composition of other lipids that regulate hepatic insulin sensitivity given that our lipidomic platform did not determine the fatty acyl constituents, positional isomers, or double bond positions in the lipid fractions containing PLs, TAGs, and diacylglycerols, the present results strongly suggest that C18:0-ceramide is important in the regulation of insulin sensitivity in lipogenic conditions. Our observations linking Elovl6 and ceramides could thus provide new insight into the pathophysiology of insulin resistance and suggest that inhibition of Elovl6 may represent a therapeutic target for the amelioration of insulin resistance.

ACKNOWLEDGMENTS

We are grateful to Drs. Akio Hayashi and Katsuya Kishikawa for their helpful comments. We also thank Katsuko Okubo and Chizuko Fukui for technical assistance, and the members of our laboratories for discussion and helpful comments on the manuscript.

REFERENCES

1. Cohen JC, Horton JD, Hobbs HH. Human fatty liver disease: old questions and new insights. Science 2011;332:1519-1523.
2. Bugianesi E, McCullough AJ, Marchesini G. Insulin resistance: a metabolic pathway to chronic liver disease. Hepatology 2005;42:987-1000.
3. Utzschneider KM, Kahn SE. Review: The role of insulin resistance in nonalcoholic fatty liver disease. J Clin Endocrinol Metab 2006;91:4753-4761.
4. Michelotti GA, Machado MV, Diehl AM. NAFLD, NASH and liver cancer. Nat Rev Gastroenterol Hepatol 2013;10:656-665.
5. Younossi Z, Anstee QM, Marietti M, Hardy T, Henry L, Eslam M, George J, et al. Global burden of NAFLD and NASH: trends, predictions, risk factors and prevention. Nat Rev Gastroenterol Hepatol 2018;15:11-20.
6. Postic C, Girard J. Contribution of de novo fatty acid synthesis to hepatic steatosis and insulin resistance: lessons from genetically engineered mice. J Clin Invest 2008;118:829-838.
7. Petersen MC, Shulman GI. Mechanisms of Insulin Action and Insulin Resistance. Physiol Rev 2018;98:2133-2223.
8. Shimano H, Sato R. SREBP-regulated lipid metabolism: convergent physiology

- divergent pathophysiology. Nat Rev Endocrinol 2017;13:710-730.

9. Petersen MC, Vatner DF, Shulman GI. Regulation of hepatic glucose metabolism in health and disease. Nat Rev Endocrinol 2017;13:572-587.

10. Guillou H, Zadravec D, Martin PG, Jacobsson A. The key roles of elongases and desaturases in mammalian fatty acid metabolism: Insights from transgenic mice. Prog Lipid Res 2010;49:186-199.

11. Moon YA, Shah NA, Mohapatra S, Warrington JA, Horton JD. Identification of a mammalian long chain fatty acyl elongase regulated by sterol regulatory element-binding proteins. J Biol Chem 2001;276:45358-45366.

12. Matsuzaka T, Shimano H, Yahagi N, Yoshikawa T, Amemiya-Kudo M, Hasty AH, Okazaki H, et al. Cloning and characterization of a mammalian fatty acyl-CoA elongase as a lipogenic enzyme regulated by SREBPs. J Lipid Res 2002;43:911-920.

13. Matsuzaka T, Shimano H, Yahagi N, Kato T, Atsumi A, Yamamoto T, Inoue N, et al. Crucial role of a long-chain fatty acid elongase, Elovl6, in obesity-induced insulin resistance. Nat Med 2007;13:1193-1202.

14. Moon YA, Ochoa CR, Mitsche MA, Hammer RE, Horton JD. Deletion of ELOVL6 blocks the synthesis of oleic acid but does not prevent the

development of fatty liver or insulin resistance. J Lipid Res 2014;55:2597-2605.

15. Horton JD, Goldstein JL, Brown MS. SREBPs: activators of the complete program of cholesterol and fatty acid synthesis in the liver. J Clin Invest 2002;109:1125-1131.

16. Kienesberger PC, Oberer M, Lass A, Zechner R. Mammalian patatin domain containing proteins: a family with diverse lipolytic activities involved in multiple biological functions. J Lipid Res 2009;50 Suppl:S63-68.

17. Bruschi FV, Tardelli M, Claudel T, Trauner M. PNPLA3 expression and its impact on the liver: current perspectives. Hepat Med 2017;9:55-66.

18. Li JZ, Huang Y, Karaman R, Ivanova PT, Brown HA, Roddy T, Castro-Perez J, et al. Chronic overexpression of PNPLA3I148M in mouse liver causes hepatic steatosis. J Clin Invest 2012;122:4130-4144.

19. Ruhanen H, Perttila J, Holtta-Vuori M, Zhou Y, Yki-Jarvinen H, Ikonen E, Kakela R, et al. PNPLA3 mediates hepatocyte triacylglycerol remodeling. J Lipid Res 2014;55:739-746.

20. Mitsche MA, Hobbs HH, Cohen JC. Patatin-like phospholipase domain-containing protein 3 promotes transfer of essential fatty acids from triglycerides to phospholipids in hepatic lipid droplets. J Biol Chem

2018;293:9232.

21. Chavez JA, Summers SA. A ceramide-centric view of insulin resistance. Cell Metab 2012;15:585-594.

22. Chaurasia B, Summers SA. Ceramides - Lipotoxic Inducers of Metabolic Disorders. Trends Endocrinol Metab 2015;26:538-550.

23. Petersen MC, Shulman GI. Roles of Diacylglycerols and Ceramides in Hepatic Insulin Resistance. Trends Pharmacol Sci 2017;38:649-665.

24. Raichur S, Wang ST, Chan PW, Li Y, Ching J, Chaurasia B, Dogra S, et al. CerS2 Haploinsufficiency Inhibits beta-Oxidation and Confers Susceptibility to Diet-Induced Steatohepatitis and Insulin Resistance. Cell Metab 2014;20:919.

25. Turpin SM, Nicholls HT, Willmes DM, Mourier A, Brodesser S, Wunderlich CM, Mauer J, et al. Obesity-induced CerS6-dependent C16:0 ceramide production promotes weight gain and glucose intolerance. Cell Metab 2014;20:678-686.

26. Wegner MS, Schiffmann S, Parnham MJ, Geisslinger G, Grosch S. The enigma of ceramide synthase regulation in mammalian cells. Prog Lipid Res 2016;63:93-119.

27. Oaks J, Ogretmen B. Regulation of PP2A by Sphingolipid Metabolism and

Signaling. Front Oncol 2014;4:388.

28. Seshacharyulu P, Pandey P, Datta K, Batra SK. Phosphatase: PP2A structural importance, regulation and its aberrant expression in cancer. Cancer Lett 2013;335:9-18.

29. Li M, Makkinje A, Damuni Z. The myeloid leukemia-associated protein SET is a potent inhibitor of protein phosphatase 2A. J Biol Chem 1996;271:11059-11062.

30. Mukhopadhyay A, Saddoughi SA, Song P, Sultan I, Ponnusamy S, Senkal CE, Snook CF, et al. Direct interaction between the inhibitor 2 and ceramide via sphingolipid-protein binding is involved in the regulation of protein phosphatase 2A activity and signaling. FASEB J 2009;23:751-763.

31. Saddoughi SA, Gencer S, Peterson YK, Ward KE, Mukhopadhyay A, Oaks J, Bielawski J, et al. Sphingosine analogue drug FTY720 targets I2PP2A/SET and mediates lung tumour suppression via activation of PP2A-RIPK1-dependent necroptosis. EMBO Mol Med 2013;5:105-121.

32. Arulmozhiraja S, Matsuo N, Ishitsubo E, Okazaki S, Shimano H, Tokiwa H. Comparative Binding Analysis of Dipeptidyl Peptidase IV (DPP-4) with Antidiabetic Drugs - An Ab Initio Fragment Molecular Orbital Study. PLoS One

2016;11:e0166275.

33. Laviad EL, Albee L, Pankova-Kholmyansky I, Epstein S, Park H, Merrill AH, Jr., Futerman AH. Characterization of ceramide synthase 2: tissue distribution, substrate specificity, and inhibition by sphingosine 1-phosphate. J Biol Chem 2008;283:5677-5684.

34. Samuel VT. Fructose induced lipogenesis: from sugar to fat to insulin resistance. Trends Endocrinol Metab 2011;22:60-65.

35. Sanders FW, Griffin JL. De novo lipogenesis in the liver in health and disease: more than just a shunting yard for glucose. Biol Rev Camb Philos Soc 2016;91:452-468.

36. Ter Horst KW, Serlie MJ. Fructose Consumption, Lipogenesis, and Non-Alcoholic Fatty Liver Disease. Nutrients 2017;9.

37. Kumadaki S, Matsuzaka T, Kato T, Yahagi N, Yamamoto T, Okada S, Kobayashi K, et al. Mouse Elovl-6 promoter is an SREBP target. Biochem Biophys Res Commun 2008;368:261-266.

38. Huang Y, He S, Li JZ, Seo YK, Osborne TF, Cohen JC, Hobbs HH. A feed-forward loop amplifies nutritional regulation of PNPLA3. Proc Natl Acad Sci U S A 2010;107:7892-7897.

39. Dubuquoy C, Robichon C, Lasnier F, Langlois C, Dugail I, Foufelle F, Girard J, et al. Distinct regulation of adiponutrin/PNPLA3 gene expression by the transcription factors ChREBP and SREBP1c in mouse and human hepatocytes. J Hepatol 2011;55:145-153.

40. Rong X, Wang B, Palladino EN, de Aguiar Vallim TQ, Ford DA, Tontonoz P. ER phospholipid composition modulates lipogenesis during feeding and in obesity. J Clin Invest 2017;127:3640-3651.

41. Hannun YA. Functions of ceramide in coordinating cellular responses to stress. Science 1996;274:1855-1859.

42. Xia JY, Holland WL, Kusminski CM, Sun K, Sharma AX, Pearson MJ, Sifuentes AJ, et al. Targeted Induction of Ceramide Degradation Leads to Improved Systemic Metabolism and Reduced Hepatic Steatosis. Cell Metab 2015;22:266-278.

43. Luukkonen PK, Zhou Y, Sadevirta S, Leivonen M, Arola J, Oresic M, Hyotylainen T, et al. Hepatic ceramides dissociate steatosis and insulin resistance in patients with non-alcoholic fatty liver disease. J Hepatol 2016;64:1167-1175.

44. Wigger L, Cruciani-Guglielmacci C, Nicolas A, Denom J, Fernandez N,

Fumeron F, Marques-Vidal P, et al. Plasma Dihydroceramides Are Diabetes Susceptibility Biomarker Candidates in Mice and Humans. Cell Rep 2017;18:2269-2279.

45. Hilvo M, Salonurmi T, Havulinna AS, Kauhanen D, Pedersen ER, Tell GS, Meyer K, et al. Ceramide stearic to palmitic acid ratio predicts incident diabetes. Diabetologia 2018;61:1424-1434.

46. Hoekstra M, Li Z, Kruijt JK, Van Eck M, Van Berkel TJ, Kuiper J. The expression level of non-alcoholic fatty liver disease-related gene PNPLA3 in hepatocytes is highly influenced by hepatic lipid status. J Hepatol 2010;52:244-251.

47. He S, McPhaul C, Li JZ, Garuti R, Kinch L, Grishin NV, Cohen JC, et al. A sequence variation (I148M) in PNPLA3 associated with nonalcoholic fatty liver disease disrupts triglyceride hydrolysis. J Biol Chem 2010;285:6706-6715.

48. Pingitore P, Pirazzi C, Mancina RM, Motta BM, Indiveri C, Pujia A, Montalcini T, et al. Recombinant PNPLA3 protein shows triglyceride hydrolase activity and its I148M mutation results in loss of function. Biochim Biophys Acta 2014;1841:574-580.

49. Senkal CE, Salama MF, Snider AJ, Allopenna JJ, Rana NA, Koller A, Hannun

YA, et al. Ceramide Is Metabolized to Acylceramide and Stored in Lipid Droplets. Cell Metab 2017;25:686-697.

50. Yetukuri L, Katajamaa M, Medina-Gomez G, Seppanen-Laakso T, Vidal-Puig A, Oresic M. Bioinformatics strategies for lipidomics analysis: characterization of obesity related hepatic steatosis. BMC Syst Biol 2007;1:12.

FIGURE LEGENDS

Figure 1. Deletion of *Elovl6* in the liver increases insulin sensitivity in lipogenic diet-fed mice

(**A**) Hepatic TAG and T-Cho concentrations in 12-week-old male Flox and LKO mice fed normal chow or HSD for 14 days (n = 9–14 per group). (**B**) Hepatic FA composition in Flox and LKO mice fed a chow or HSD for 14 days (n = 5 per group). (**C**) Plasma concentrations of glucose and insulin in Flox and LKO mice fed a chow or HSD for 14 days (n = 14–25 per group). (**D**) Plasma glucose and insulin concentrations and AUCs of glucose during OGTTs in Flox and LKO mice fed a chow or HSD for 14 days (n = 24–26 per group). (**E**) Plasma glucose concentrations and AUCs during ITTs in Flox and LKO mice fed an HSD for 14 days (0.5 U insulin/kg, n = 14–19 per group). (**F**)

Immunoblot analysis of the insulin signaling in response to a bolus injection of insulin in the livers of Flox and LKO mice fed an HSD for 14 days. The results were quantified by densitometry (n = 3 per group). *$p < 0.05$, **$p < 0.01$, ***$p < 0.001$.

Figure 2. Reduction in hepatic Pnpla3 expression is involved in the higher insulin sensitivity of LKO mice

(**A**) Heatmap representation of the differentially expressed transcripts identified using microarray in the livers of HSD-fed Flox and LKO mice. Arbitrary signal intensity acquired from the microarray analysis is represented by colors (n = 3 per group). (**B**) Pathways that were significantly affected by hepatic Elovl6 deficiency. Significantly enriched ($p < 0.01$) metabolic pathways identified using the KEGG database are shown. (**C**) mRNA expression of *Elovl6*, *Srebf1c*, and *Pnpla3* in the livers of Flox and LKO mice fed a chow or HSD for 14 days (n = 15–29 per group). **$p < 0.01$, ***$p < 0.001$. (**D**) Adenovirus-mediated restoration of Pnpla3 expression in the livers of LKO mice. Immunoblot analysis of Pnpla3 expression in the livers of Flox and LKO mice infected with adenovirus encoding GFP (Ad-GFP) or Pnpla3 (Ad-Pnpla3). Twelve-week-old male Flox and LKO mice were fed an HSD for 7 days, then infected with Ad-GFP or Ad-Pnpla3. After adenovirus infection, the mice were fed an HSD for 7 days. (**E**)

Plasma glucose concentrations and AUCs during ITTs in Flox and LKO mice infected with either Ad-GFP or Ad-Pnpla3 (0.5 U insulin/kg, n = 12–17 per group). *$p < 0.05$, **$p < 0.01$ for LKO Ad-GFP vs. Flox Ad-GFP mice. #$p < 0.05$, ##$p < 0.01$ for LKO Ad-Pnpla3 vs. LKO Ad-GFP mice. (**F**) Immunoblot analysis of the insulin signaling pathway in response to a bolus injection of insulin in the livers of Flox and LKO mice infected with either Ad-GFP or Ad-Pnpla3. The results were quantified by densitometry (n = 5 per group). *$p < 0.05$, **$p < 0.01$.

Figure 3. Hepatic insulin sensitivity is associated with changes in the ceramide profile and PP2A activity

(**A**) Heatmap of the liver lipidomic analysis of HSD-fed Flox and LKO mice infected with either Ad-GFP or Ad-Pnpla3. The heatmap shows metabolites that were significantly altered by Elovl6 deficiency or Ad-Pnpla3 infection. The relative content is indicated by the color. (**B, C**) LC-MS/MS analysis of liver ceramide species from Flox and LKO mice fed a chow diet or HSD (n = 5 or 6 per group, **B**), or infected with either Ad-GFP or Ad-Pnpla3 (n = 3–6 per group, **C**). The indicated molecular species were confirmed by product ion scanning. (**D**) The hepatic PP2A activity of Flox and LKO mice fed a normal chow or HSD (n = 6–9 per group) or infected with either Ad-GFP

(GFP) or Ad-Pnpla3 (P3, n = 5–7 per group). The phosphatase activity of the immunoprecipitated PP2A was quantified using a phosphatase activity assay. (**E**) Immunoblot analysis of phosphorylated PKCζ and total PKCζ in the livers of Flox and LKO mice fed a normal chow or HSD. The ratio of phosphorylated to total PKCζ was determined by densitometry (n = 4 per group). *$p < 0.05$, **$p < 0.01$, ***$p < 0.001$.

Figure 4. Ceramide(d18:1/18:0) inhibits the I2PP2A–PP2A interaction and insulin-induced phosphorylation of Akt in HepG2 cells

(**A**) Immunoblot analysis of Akt phosphorylation in response to insulin treatment of HepG2 cells pretreated with ceramide(d18:1/16:0), ceramide(d18:1/18:0), ceramide(d18:1/20:0), or vehicle. Cells were pretreated with media containing vehicle or 10 μM ceramide for 4 h before insulin stimulation. The ratio of phosphorylated to total Akt was determined using densitometry (n = 6 per group). (**B**) Effect of ceramide species on the interaction between PP2A and I2PP2A. HepG2 cells were incubated with the indicated ceramide for 4 h. The PP2A–I2PP2A interaction was determined by immunoprecipitation using an anti-FLAG antibody, followed by immunoblotting using anti-HA and anti-FLAG antibodies. The PP2A–I2PP2A interaction was quantified using densitometry (n = 6 per group). (**C**) Effect of I2PP2A knockdown on insulin-induced

Akt phosphorylation in HepG2 cells treated with 10 mM ceramide for 4 h. The ratio of phosphorylated to total Akt was determined using densitometry (n = 5 per group). (**D**) Molecular docking simulations of ceramide(d18:1/16:0), ceramide(d18:1/18:0), and ceramide(d18:1/20:0) with I2PP2A, and van der Waals interaction energy between the ceramides and amino acid residues of I2PP2A. Hydrophobic and hydrophilic residues are shown in red and blue, respectively. *$p < 0.05$, **$p < 0.01$, ***$p < 0.001$.

Figure 5. CerS4 interacts with Elovl6 and Pnpla3

HEK293 cells were transfected with FLAG-tagged Elovl6, HA-tagged Pnpla3, and (or) V5-tagged CerS4. (**A**) Co-localizations of Elovl6-FLAG with CerS4-V5, Pnpla3-HA with CerS4-V5, and Elovl6-FLAG with Pnpla3-HA were identified using confocal microscopy. Scale bar = 10 μm. (**B**) Interactions among Elovl6, Pnpla3, and CerS4 determined by immunoblotting after immunoprecipitation using the indicated antibodies.

Figure 6. Hepatic deletion of Elovl6 ameliorates insulin resistance in *ob/ob* mice

(**A**) Body, liver, and eWAT weights of 12-week-old Flox, *ob/ob*, and *ob/ob*-LKO mice (n = 17−25 per group). (**B**) Plasma glucose and insulin concentrations of 12-week-old

Flox, *ob/ob*, and *ob/ob*-LKO (n = 17–25 per group). (**C**) Plasma glucose concentration during OGTTs (n = 14–22 per group) and ITTs (2.0 U insulin/kg, n = 10 or 11 per group), and AUCs during the ITT (n = 10 or 11 per group) in 12-week-old Flox, *ob/ob*, and *ob/ob*-LKO mice. (**D**) qPCR analysis of genes involved in DNL in livers of Flox, *ob/ob*, and *ob/ob*-LKO mice (n = 16–21 per group). (**E**) LC-MS/MS analysis of liver ceramide species from Flox, *ob/ob*, and *ob/ob*-LKO mice. The indicated molecular species were confirmed by product ion scanning (n = 3 or 4 per group). (**F**) Liver PP2A activity of Flox, ob/ob, and ob/ob-LKO mice (n = 5 or 6 per group). *$p < 0.05$, **$p < 0.01$, ***$p < 0.001$.

Figure 7. Schematic description of the Elovl6/Pnpla3/CerS pathway regulating hepatic insulin signaling

Excess consumption of carbohydrate and hyperinsulinemia activate *de novo* lipogenesis and upregulate the expression of Elovl6 and Pnpla3 in the liver. Activation of Elovl6 increases the amount of C18:0, enhancing C18:0-ceramide production through formation of an enzyme complex with CerS4 on the ER. Pnpla3 acts on the surface of LDs, releases FAs from TAGs, and modifies ceramide FA composition by forming an enzyme complex with CerS4 at the ER-LD interface. Both Elovl6 and Pnpla3 are linked

to the generation of C18:0-ceramide, which activates PP2A by disrupting the interactions with its endogenous inhibitor I2PP2A. As a consequence, PP2A inhibits insulin signaling by impairing Akt activation.

Figure 1

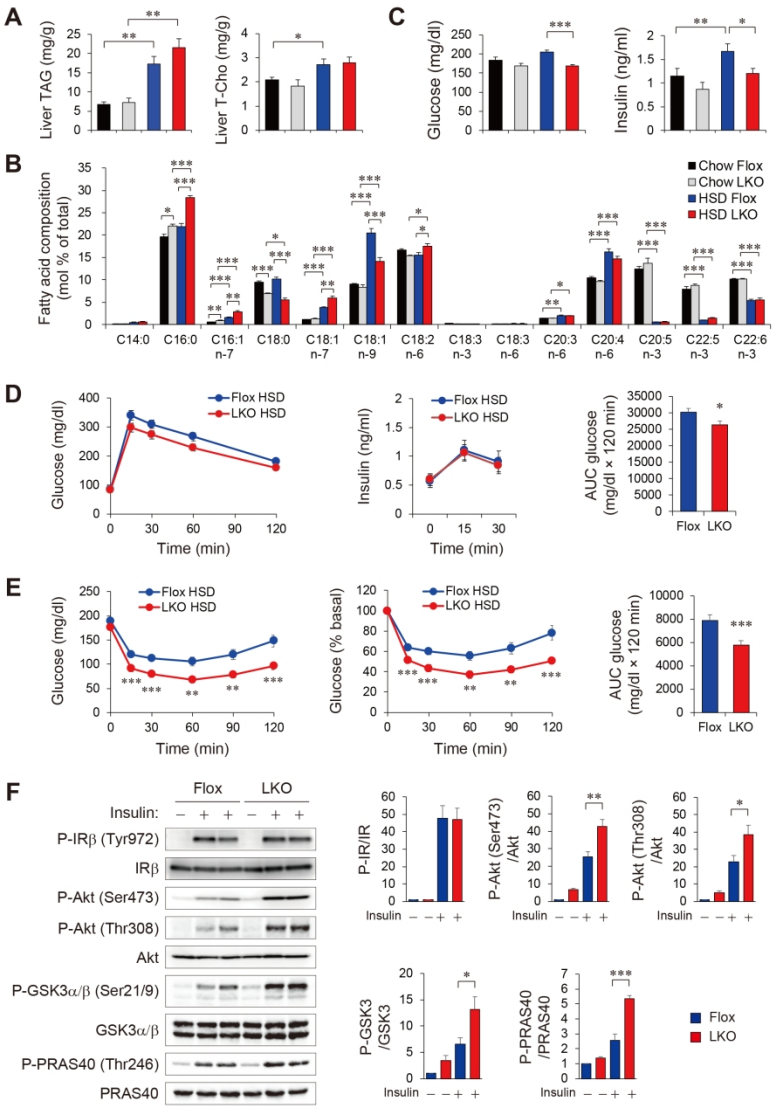

Figure 1. Deletion of Elovl6 in the liver increases insulin sensitivity in lipogenic diet-fed mice

Figure 2

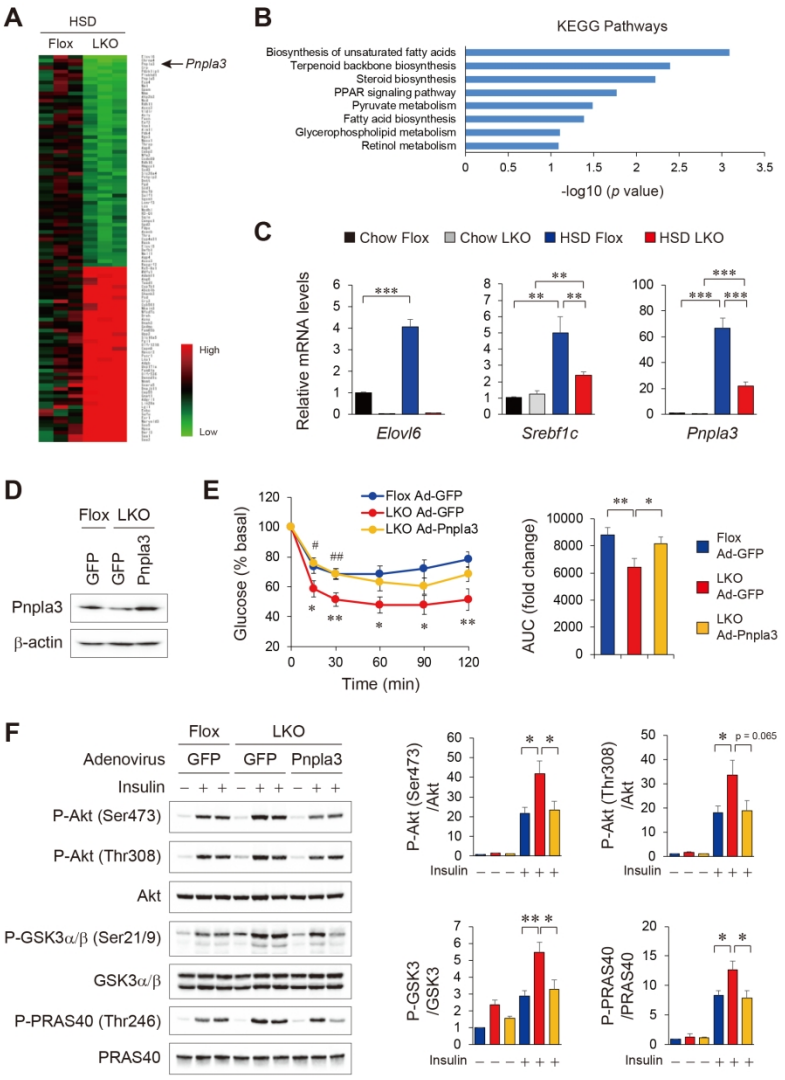

Figure 2. Reduction in hepatic Pnpla3 expression is involved in the higher insulin sensitivity of LKO mice

Figure 3

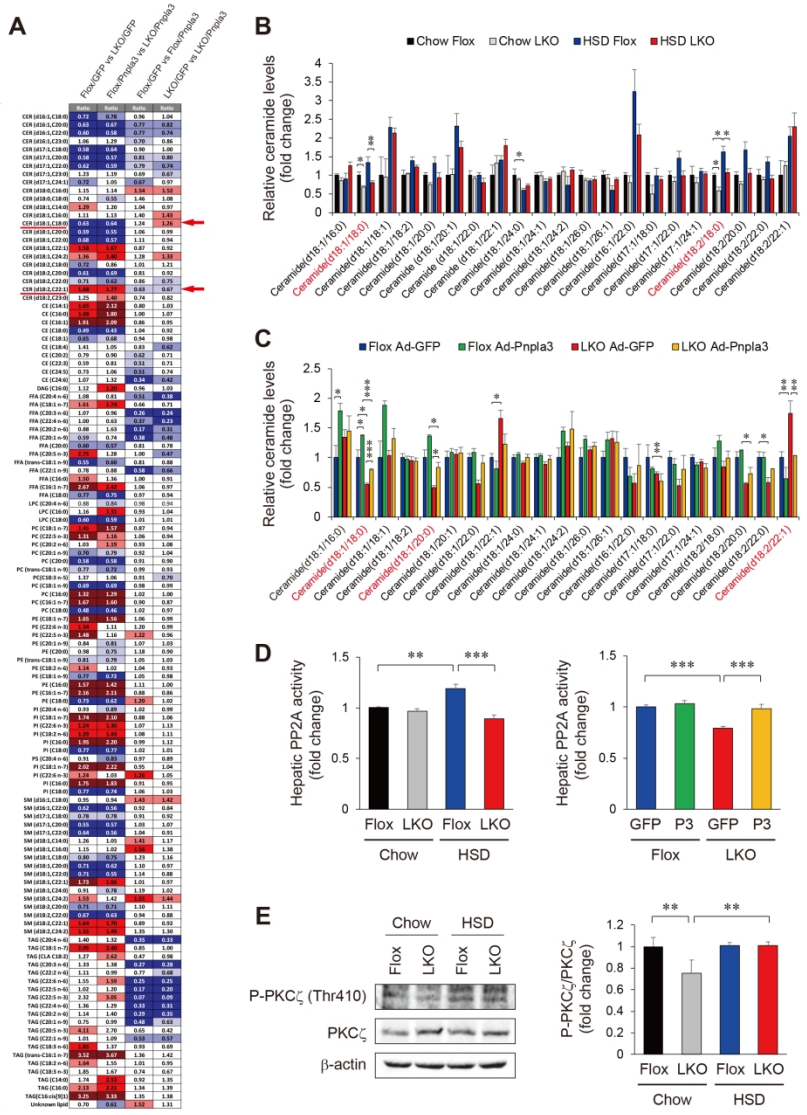

Figure 3. Hepatic insulin sensitivity is associated with changes in the ceramide profile and PP2A activity

Figure 4

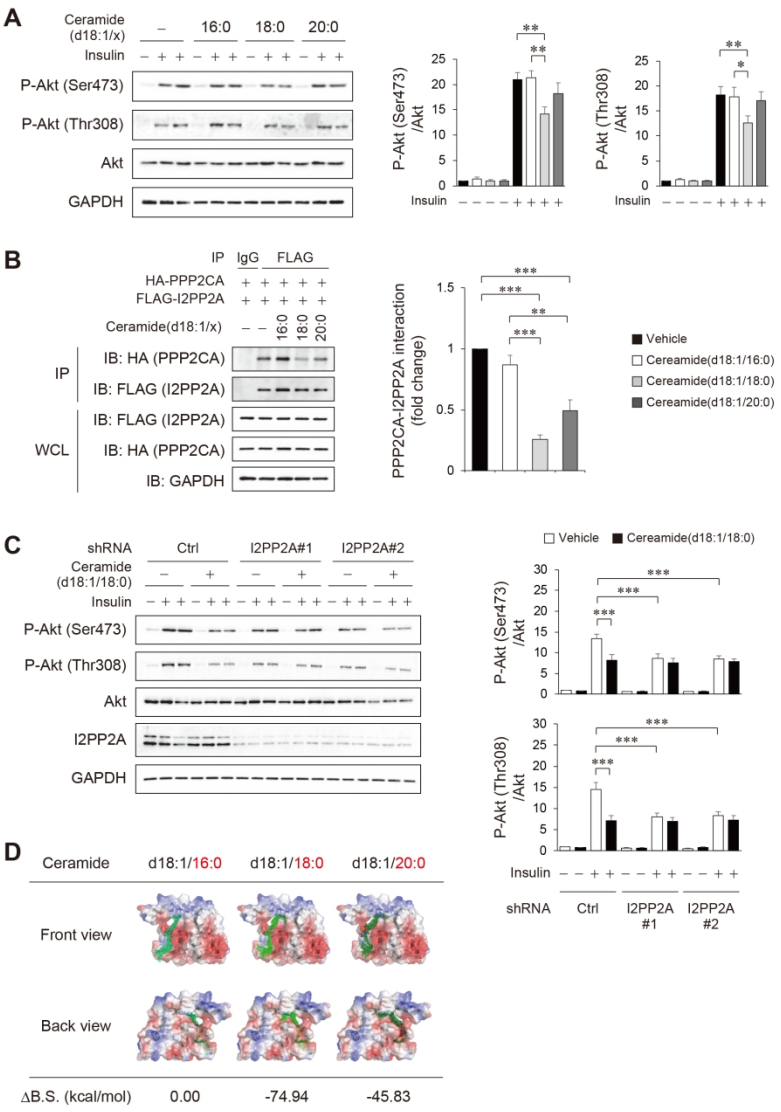

Figure 4. Ceramide(d18:1/18:0) inhibits the I2PP2A–PP2A interaction and insulin-induced phosphorylation of Akt in HepG2 cells

Figure 5

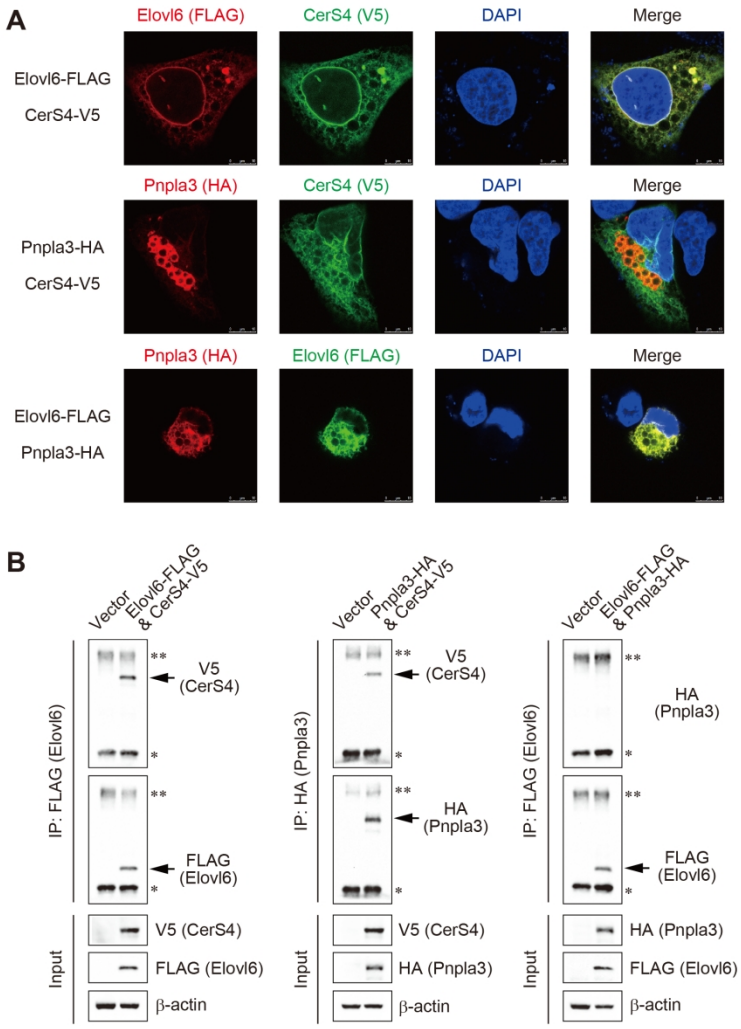

Figure 5. CerS4 interacts with Elovl6 and Pnpla3

Figure 6

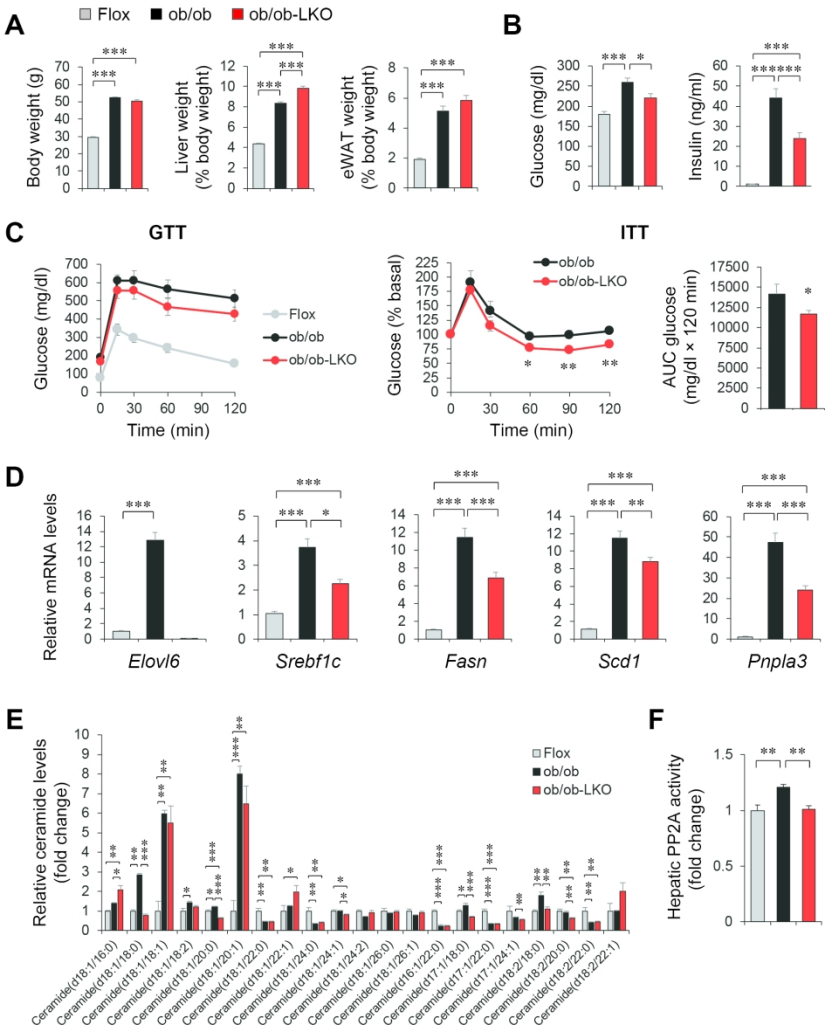

Figure 6. Hepatic deletion of Elovl6 ameliorates insulin resistance in ob/ob mice

Figure 7

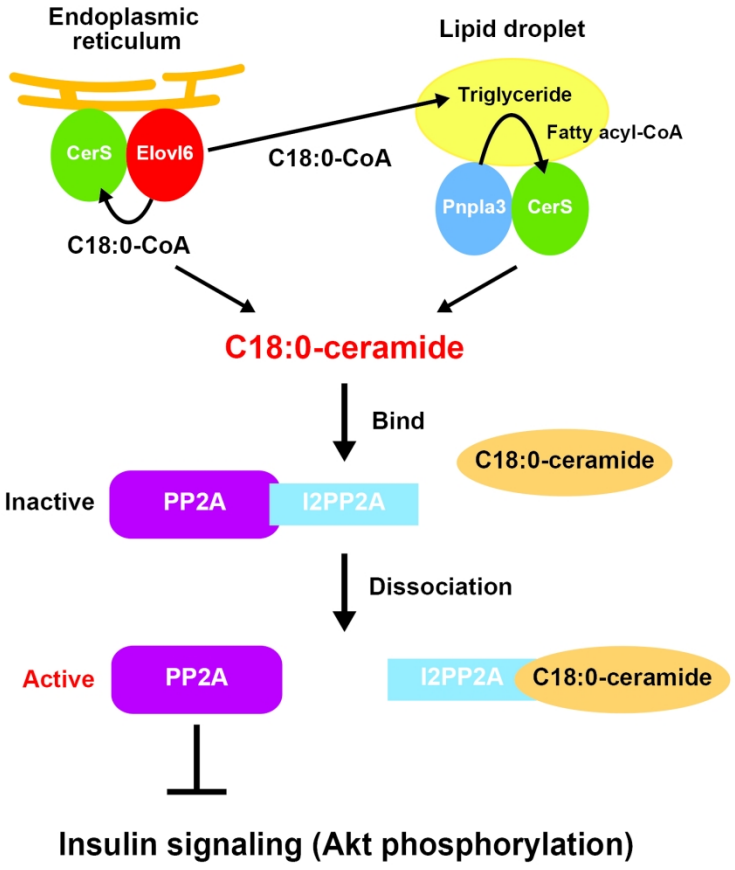

Figure 7. Schematic description of the Elovl6/Pnpla3/CerS pathway regulating hepatic insulin signaling

SUPPORTING INFORMATION

Hepatocyte Elovl6 determines ceramide acyl-chain length and hepatic insulin sensitivity in mice

Takashi Matsuzaka, Motoko Kuba, Saori Koyasu, Yuta Yamamoto, Kaori Motomura, Sundaram Arulmozhiraja, Hiroshi Ohno, Rahul Sharma, Takuya Shimura, Yuka Okajima, Song-iee Han, Yuichi Aita, Yuhei Mizunoe, Yoshinori Osaki, Hitoshi Iwasaki, Shigeru Yatoh, Hiroaki Suzuki, Hirohito Sone, Yoshinori Takeuchi, Naoya Yahagi, Takafumi Miyamoto, Motohiro Sekiya, Yoshimi Nakagawa, Masatsugu Ema, Satoru Takahashi, Hiroaki Tokiwa, and Hitoshi Shimano

SUPPORTING MATERIALS AND METHODS

Materials.

Human insulin was obtained from Novo Nordisk. HepG2 and HEK293 cells were purchased from American Type Culture Collection (ATCC). Ceramide(d18:1/16:0), ceramide(d18:1/18:0), and ceramide(d18:1/20:0) were purchased from Avanti Polar Lipids. Antibodies against phospho-insulin receptor (Tyr972) (Cat# 07-838; RRID: AB_568829), insulin receptor beta subunit (Cat# 07-724; RRID: AB_11213944), IRS-1 (Cat# 05-1085; RRID: AB_1977296), and IRS-2 (Cat# 06-506; RRID: AB_10615782) were obtained from Millipore. Antibodies against phospho-Akt (Ser473) (Cat# 4060; RRID: AB_2315049), phospho-Akt (Thr308) (Cat# 13038; RRID: AB_2629447), Akt (pan) (Cat# 4691; RRID: AB_915783), phospho-Tyrosine (Cat# 3089; RRID: AB_331228), lamin A/C (Cat# sc-8984; RRID: AB_2136278), phospho-PKC zeta (Thr410) (Cat# 2060; RRID: AB_561487), PKC zeta (Cat# 9368; RRID: AB_10693777), DYKDDDDK-Tag (Cat# 14793; RRID: AB_2572291), V5-Tag (Cat# 13202; RRID: AB_2687461), and glyceraldehyde-3-phosphate dehydrogenase (GAPDH) (Cat# 5174; RRID: AB_10622025) were obtained from Cell Signaling Technology. Antibodies against PNPLA3 (Cat# ab81874; RRID: AB_10712485), SET

(Cat# ab181990; RRID: AB_2737445), and Calreticulin (Cat# ab92516; RRID: AB_10562796) were obtained from Abcam. Antibodies against PKC epsilon (Cat# sc-214; RRID: AB_2237729) and SREBP-1 (Cat# 9411; RRID: AB_2194223) were obtained from Santa Cruz Biotechnology. Antibodies against DDDDK-Tag (Cat# PM020; RRID: AB_591224) and HA-tag (Cat# M180-3; RRID: AB_10951811) were obtained from MBL International. Antibody against V5-Tag (Cat# R960-25; RRID: AB_255656) was obtained from Thermo Fisher Scientific. Anti-DDDDK-tag mAb-Magnetic Agarose (Cat# M185-10), anti-HA-tag mAb-Magnetic Agarose (Cat# M180-10), and Anti-V5-tag mAb-Magnetic Agarose (Cat# M167-10) were purchased from MBL International. Tristearin and triolein were purchased from Tokyo Chemical Industry and FUJIFILM Wako Chemicals, respectively.

Generation of liver-specific *Elovl6* knockout mice.

The targeting vector for *Elovl6* gene disruption was constructed by ligation of three polymerase chain reaction (PCR) fragments into a conditional targeting vector cassette (51). The targeting vector was linearized and transfected into C57BL/6J mouse embryonic stem (ES) cells (52). ES cells that integrated the targeting vector either by homologous or random integration were selected by growth on G418. The anticipated

homologous recombination was subsequently confirmed by PCR and Southern hybridization. ES cells harboring the homologous integration were injected into ICR mouse blastocysts to generate chimeric mice. Male mice chimeric for the targeted allele were mated with female Flpe-transgenic mice to remove the Neo cassette and generate a floxed *Elovl6* allele (*Elovl6*$^{l\circ x/+}$). Offspring *Elovl6*$^{lox/+}$ mice were intercrossed with C57BL/6J Albumin-Cre mice (stock No: 003574, Jackson Laboratory) to generate compound heterozygous (*Elovl6*$^{l\circ x/+;Cre/+}$) mice. Compound heterozygous mice were crossed with *Elovl6*$^{l\circ x/l\circ x}$ mice to obtain *Elovl6*$^{l\circ x/l\circ x;Cre/+}$ (liver-specific Elovl6 knockout: LKO) mice. Genotyping was performed by PCR using genomic DNA isolated from the tail tip as previously described (3). The primer sequences for the Cre transgenes are available from the Jackson Laboratory (https://www2.jax.org/protocolsdb/f?p=116:5:0::NO:5:P5_MASTER_PROTOCOL_ID,P5_JRS_CODE:20627,003574). For Elovl6 lox genotyping, we used primers 5'-GCTCAGCAGCCTTCCTGTGAG-3' (P1) and 5'-TCCACTGGACAGAGTGGCTTC-3' (P2). Age-matched male littermates were used in all experiments. We sacrificed mice during the early light phase, after a 4-h fast.

Elovl6 enzyme activity assay.

Elovl6 enzyme activity was determined in liver microsomes by measuring [2-^{14}C]malonyl-CoA incorporation into exogenous palmitoyl-CoA as described previously (12, 13).

Fatty acid composition of liver.

Total lipids in liver were extracted using Bligh–Dyer's procedure, and the relative abundances of each FA were measured quantitatively by LC-MS/MS as described previously (53).

Metabolic measurements.

Glucose, insulin, triglyceride (TAG), total cholesterol (T-Cho), free fatty acid (FFA), alanine aminotransferase (ALT), and aspartate aminotransferase (AST) levels in plasma and TAG and T-Cho levels in liver were determined as described previously (13, 54). For the oral glucose tolerance test (OGTT), mice were orally administrated D-glucose (1 g/kg body weight) after an overnight fast (16 h). For the insulin tolerance test (ITT), mice were injected intraperitoneally with regular human insulin (Eli Lilly Japan) after a 4-h fast. Blood samples were collected before injection and at specific times after injection (indicated in figures) to determine glucose and insulin levels. Hepatic TAG

and T-Cho levels were measured as described previously (13).

***In vivo* insulin stimulation assay.**

Mice were fasted for 4 h and anesthetized by injection of 30 mg/kg pentobarbitone (Kyoritsu Seiyaku, Tokyo, Japan). We then opened the peritoneal cavity and injected either saline control or insulin (0.5 units/kg) into the inferior vena cava. After 1.5 min, the livers were rapidly excised and immediately frozen in liquid nitrogen. We performed immunoprecipitation and immunoblot analysis of insulin signaling molecules using tissue homogenates.

Dietary fat supplementation.

Twelve-week-old male Flox and LKO mice were fed with HSD or HSD supplemented with 20% (w/w) tristearin (C18:0) plus 20% triolein (C18:1n-9) for 14 days.

Preparation of recombinant adenovirus and animal transduction.

Adenoviruses expressing full-length mouse Pnpla3 (Ad-Pnpla3) or GFP (Ad-GFP) control were prepared as described (13). Adenoviruses were injected into the mice via the tail vein at 1×10^9 plaque-forming units. Mice were sacrificed for analysis on day 7

after viral injection.

Microarray analysis.

Total RNA was extracted using the NucleoSpin RNA Kit (TaKaRa Bio, Shiga, Japan) according to the manufacturer's instructions. To determine the quality of RNA, the RNA Integrity Number (RIN) was measured using the Agilent 2100 Bioanalyzer. Microarray analysis was performed with the SurePrint G3 Mouse Gene Expression 8X60K Microarray Kit (#G4852A, Agilent Technologies). Data were analyzed by Expressionist Analyst software version 8.2.7b (Genedata AG, Basel, Switzerland). Heatmaps were generated using Multi Experiment Viewer (MeV) software (http://www.tm4.org/mev.html). Pathway analysis was performed using GO and KEGG analysis systems provided by DAVID v6.8 (https://david.ncifcrf.gov/). The raw data are available in the Gene Expression Omnibus (GEO) database (GSE123494).

RNA extraction and quantitative real-time PCR analysis.

Total RNA extraction from liver, cDNA synthesis, and quantitative real-time PCR (qPCR) were performed as previously described (13, 54, 55). For the qPCR of *Pnpla3*, we used primers 5'-TCACCTTCGTGTGCAGTCTC-3' (forward) and

5'-CCTGGAGCCCGTCTCTGAT-3' (reverse). For the qPCR of *Pnpla5*, we used primers 5'-ACACTGCCCTTCGAGTATGC-3' (forward) and 5'-CAGGATGCTCCTCATCCAAT -3' (reverse). mRNA expression levels were normalized to that of cyclophilin mRNA and expressed relative to the appropriate experimental control using the ΔΔCT method.

Immunoblotting.

Immunoblotting was performed as described previously (3). Aliquots of whole cell lysate (50 μg), membrane fraction (25 μg), and nuclear extract (25 μg) proteins from liver, WAT, or skeletal muscle were loaded onto SDS-PAGE gels, separated, and transferred to PDVF membranes. The membranes were probed with primary antibodies overnight at 4 °C, followed by labeling with horseradish peroxidase (HRP)-conjugated secondary antibody against mouse or rabbit IgG (Cell Signaling Technology Japan, Tokyo, Japan). Immune complexes were visualized using enhanced chemiluminescence (Bio-Rad Laboratories, Hercules, CA, USA). The intensity of the bands was quantified using ImageJ software (National Institutes of Health) and normalized to β-actin or GAPDH.

Metabolite profiling analysis in the MxP Lipids platform.

The MxP® Lipids platform (Metanomics Health GmbH, Berlin, Germany) was used for the entire lipid analysis workflow. The total lipid content of freeze-dried, homogenized liver tissue was extracted using chloroform/methanol. The lipid extracts were subsequently fractionated using normal phase liquid chromatography into 11 different lipid groups. The lipid fractions containing cholesterol esters (CEs), sphingomyelins (SMs), and ceramides were analyzed by liquid chromatography coupled with tandem mass spectrometry (LC-MS/MS) using electrospray ionization and atmospheric pressure chemical ionization with detection of specific multiple reaction monitoring transitions. The lipid fractions containing monoacylglycerols, diacylglycerols, triacylglycerols (TAG), phosphatidylcholines, phosphatidylserines, phosphatidylinositols, lysophosphatidylcholines and FFAs were analyzed by gas chromatography-flame ionization detection after derivatization with trimethyl sulfonium hydroxide to yield FA methyl esters corresponding to the acyl moieties of the class-separated lipids. The concentrations of FA methyl esters in the C14–C24 range were determined in each fraction.

Metabolite profiling based on a semi-quantitative analytical platform yields relative metabolite levels (“ratios”) to a defined reference. To support this concept and

allow alignment of different analytical batches, two different reference sample types were run in parallel throughout the whole process. First, a project pool was generated from aliquots of all samples and measured with four replicates within each analytical sequence of 24 samples. For all semi-quantitatively analyzed metabolites, the data were normalized against the median of the pooled reference sample within each analytical sequence to provide pool-normalized ratios (performed for each sample per metabolite). This processing step compensated for inter- and intra-instrumental variation, i.e., normalized the variability that occurs when different analytical sequences are analyzed by different devices. The limit of detection and the dynamic range of the semi-quantitative measurements were determined by dilution and spiking experiments during method development. The term "additional" (add.) was applied to metabolite names when the quantification was disturbed by metabolites exhibiting identical analytical characteristics with respect to the quantitation method.

Prior to statistical analysis, log10 transformation of ratios was conducted so that the data distribution was approximately normal. SIMCA-P version 13.0 (Umetrics AB, Umea, Sweden), TIBCO Spotfire 3.3.1, and R 2.8.1 were used for data analyses and visualization. Initially, an exploratory multivariate analysis [Principal Component Analysis (PCA)] was applied to log10-transformed ratios scaled to unit variance. A

mixed linear model (ANOVA, R package nlme) with “genotype,” “adenovirus,” and “adenovirus:genotype,” as fixed effects was fitted to the data. Significance level was set to 5%. The multiple test problem was addressed by calculating the false discovery rate (FDR) using the Benjamini & Hochberg method (56).

Targeted ceramide profiling analysis.

Total lipids were extracted from freeze-dried, homogenized liver tissue using chloroform/methanol containing 1% acetic acid and the internal standards. The lipid extracts were subjected to ceramide profiling by liquid chromatography tandem mass spectrometry (LC-MS/MS) using a UltiMate3000 BioRS system (Thermo Fisher Scientific) coupled to a 3200QTRAP triple quadrupole mass spectrometer (SCIEX) equipped with an ESI source. LC separation was achieved using a reverse-phase *L-column2 C8* metal-free column (3 μm particle size, 2.1 mm i.d. × 100 mm; Chemicals Evaluation and Research Institute, Tokyo, Japan) at 40 °C. Sample injection volume was 3 μL, flow rate was 0.3 mL/min, and sampler temperature was 4°C. Mobile phase A consisted of ultra-pure water/acetonitrile (1:1) with 1 mM ammonium formate and mobile phase B of acetonitrile/2-propanol (1:9). The targeted analyses were performed in positive multiple reaction monitoring mode. We used ceramide(d18:1/17:0) as an

internal standard and ceramide(d18:1/18:0) for the preparation of standard solution. Samples were measured in triplicate. MS data were acquired and processed using the Xcalibur 3.0 software package. Lipid Search (Mitsui Knowledge Industry, Tokyo, Japan) was used for lipid molecular species identification and quantification.

Protein phosphatase 2A (PP2A) activity assay.

The PP2A activity in liver lysates were measured using a PP2A Immunoprecipitation Phosphatase Assay kit (Merck Millipore, Darmstadt, Germany), according to the manufacturer's protocol.

Lentivirus production and transduction.

Lentivirus production and transduction were performed as described previously (57). MISSION TRC shRNA target sets for human I2PP2A (TRCN0000063716 and TRCN0000063717) and negative control (nontarget; SHC002) were purchased from Sigma-Aldrich (St. Louis, MO, USA). Generation and infection of lentivirus were performed according to the manufacturer's instructions.

Molecular modeling of I2PP2A with ceramides.

The complex structures of I2PP2A during interactions with ceramide(d18:1/16:0), ceramide(d18:1/18:0), and ceramide(d18:1/20:0) were constructed using the Molecular Operating Environment (MOE) program (Chemical Computing Group, https://www.chemcomp.com/MOE-Molecular_Operating_Environment.htm) by combining I2PP2A X-ray structures (PDB ID: 2E50). The preliminary structure optimization was performed by molecular mechanics calculations utilizing the Amber10EHT force field with solvation energy accounted via the Born model. The constructed structure was subjected to molecular dynamics (MD) simulations up to 500 ps to analyze the stability of modelled structures. The initial setups for the MD simulations were made by using the AMBER14 program (http://ambermd.org/) utilizing ff14SB force field. The MD simulations were performed with explicit solvent water molecules. AMBER topology files created using AMBER were converted to GROMACS format using acpype.py script (58). All the MD simulations were performed using the GROMACS package (http://www.gromacs.org/). Calculations were run at 300 K and a pressure of 1 bar, with the NPT ensemble. FMO calculations were carried out using the PAICS program (59). The correlated Resolution-of-Identity second-order Moller Plesset (RI-MP2) level of theory with correlation-consistent double ζ basis set cc-pVDZ was used for the FMO calculations.

Culture of HepG2 cells, ceramide treatment, and insulin stimulation.

Human hepatocellular carcinoma HepG2 cells were cultured in Dulbecco's Modified Eagle's Medium (DMEM) supplemented with 10% fetal bovine serum and 1% penicillin/streptomycin. For ceramide treatment, HepG2 cells were seeded into collagen I-coated 60-mm dishes and cultured in serum-free DMEM supplemented with 0.5% FA-free bovine serum albumin. Then, the cells were permeabilized with 20 μg/mL digitonin for 5 min and incubated for 4 h with C16–C20 ceramide solubilized in 2% dodecane/98% ethanol solution. In addition, some cells were treated with insulin (100 nM) for 10 min.

Culture of HEK293 cells, plasmid construction, transfection, and immunoprecipitation.

Human Embryonic Kidney 293 (HEK293) cells were cultured in DMEM supplemented with 10% FBS and 1% penicillin/streptomycin. cDNAs encoding C-terminal FLAG-tagged Elovl6, C-terminal HA-tagged Pnpla3, and C-terminal V5-tagged CerS4 were cloned separately into the pcDNA3.1 plasmid. Cells were transiently transfected with the indicated plasmid combinations using Lipofectamine 3000 (Life Technologies

Corporation, NY, USA) according to the manufacturer's protocol. Anti-FLAG, anti-HA, and anti-V5 immunoprecipitations were performed by incubating cell lysates with anti-FLAG, anti-HA, and anti-V5 magnetic agarose antibodies (MBL, Nagaya, Japan), respectively, overnight on an end-to-end rotator at 4 °C. The immunoprecipitated complexes were washed with excess volumes of lysis buffer before SDS-PAGE separation and immunoblotting.

Immunofluorescence and confocal microscopy analysis.

HEK293 cells were plated on 35-mm dishes with poly-lysine-coated glass bottoms (Matsunami Glass, Osaka, Japan), and were transiently transfected with the indicated plasmid using Lipofectamine 3000 (Life Technologies Corporation, NY, USA) according to the manufacturer's protocol. Cells were then washed with 1× phosphate buffered saline (PBS), fixed with 4% (w/v) paraformaldehyde in 1× PBS for 15 min, washed and permeabilized with 0.1% Triton X-100 in PBS for 5 min, washed three times with 1× PBS, and blocked in 1% (w/v) FA-free BSA containing 1× PBS for 1 h. After incubation with primary antibodies at 1:500 dilution in 1% BSA solution, cells were washed in PBS and incubated with secondary antibodies conjugated to Alexa Fluor dyes (Life Technologies Corporation, NY, USA) for 1 h. For the detection of

LDs, cells were incubated with 10 μM BODIPY 493/503 (Thermo Fisher Scientific, MA, USA) for 1 h. Dishes were mounted with VECTEASHIELD Mounting Medium and DAPI (Vector Laboratories, CA, USA). Immunofluorescence was performed using a TCS SP5 confocal microscope (Leica, Wetzlar, Germany), and images and overlays were analyzed using LAS AF software (Leica, Wetzlar, Germany).

SUPPORTING DISCUSSION

We have previously shown that global Elovl6 deficiency prevents diet-induced insulin resistance by modifying hepatic FA composition (13). However, unexpectedly, we found that LKO mice were not protected from HFHS diet-induced insulin resistance. We interpret this result as indicating that the deletion of *Elovl6* in hepatic non-parenchymal cells, such as Kupffer cells and stellate cells, or in extrahepatic tissues, such as adipose tissue, skeletal muscle, and intestine, may be necessary to generate a protective effect of Elovl6 inhibition on mice fed an HFHS diet.

Our results also show a positive correlation between ceramide(d18:2/22:1) and insulin sensitivity. However, we could not determine the direct effect of ceramide(d18:2/22:1) on insulin sensitivity because there is no commercially available standard or this ceramide and it is difficult to chemically synthesize it. Moreover, to our knowledge, there have been no reports regarding the role of ceramide(d18:2/22:1) in cell physiology and disease. Future studies should aim to determine the physiologic and clinical relevance of this ceramide for insulin resistance and disease in humans.

Although PP2A and PKCζ are downstream targets of ceramide modulation, their roles in DNL-dependent insulin sensitivity have not been evaluated. Here we show that a reduction in PP2A activity, but not in PKCζ activity, was associated with higher insulin sensitivity in HSD-fed LKO mice, suggesting that the activation of hepatic PP2A depends on the production of ceramides by Elovl6. Because Elovl6 and Pnpla3 are nutritionally regulated, as SREBP-1 targets, and are crucial for ceramide formation, the acyl-CoAs used for ceramide synthesis are likely derived from DNL and TAGs in LDs. Another possible impact of Elovl6 deficiency on ceramide metabolism is activation of the *de novo* synthesis of ceramide. It is likely that greater palmitoyl-CoA accumulation in LKO hepatocytes activates *de novo* ceramide synthesis because palmitoyl-CoA and L-serine are precursors for the sphingolipid biosynthesis (22). Thus, suppression of C18:0-ceramide in the liver of LKO mice may result from a combination of the activation of *de novo* ceramide synthesis and a reduction in C18:0 synthesis.

SUPPORTING FIGURE LEGENDS

Supporting Figure 1. Generation of liver-specific Elovl6 knockout mice

(**A**) Schematic representation of the mouse *Elovl6* gene. Each box represents one exon. The black boxes represent the *Elovl6* coding exons (numbered) and open boxes indicate non-coding regions. (**B**) Targeting strategy for conditional deletion of the *Elovl6* gene. The targeting construct contains the fifth exon (the conserved HXXHH motif and the 3' untranslated region-containing exon) of *Elovl6* flanked by three loxP sites and the PGK-neo cassette (Neo) flanked by FRT sites. Neo was removed by crossing with mice expressing FLPe under control of the human β-actin promoter. *Elovl6* exon 5 was deleted by mating *Elovl6* Flox+/− mice with Albumin-Cre mice. Arrows to P1 and P2 indicate the positions of primers for genotyping. We confirmed homologous recombination between the targeting vector and Elovl6 locus in C57BL6/J mouse embryonic stem (ES) cells by polymerase chain reaction (PCR) and Southern hybridization (data not shown). Chimeric mice were obtained by microinjecting Elovl6 flp/+ ES cells into mouse blastocysts, and the resulting animals were crossed with C57BL/6J mice to achieve germ line transmission of the floxed allele. Next, Elovl6 lox/+ mice were mated with the general deleter mouse ACTB-FLPe to remove the

phosphoglycerokinase (PGK) neomycin resistance (neo) cassette, which might produce unwanted side effects, by excisional recombination of the Flp/FRT system. Elovl6 lox/lox mice were successfully generated by mating male and female Elovl6 lox/+ mice. Elovl6 lox/lox (Flox) mice were phenotypically indistinguishable from wild-type mice and showed normal Elovl6 mRNA expression and Elovl6 enzyme activity (data not shown), indicating the loxP sites did not interfere with Elovl6 expression. To generate liver-specific Elovl6 deficient mice, we crossed Elovl6 lox/lox mice to albumin promoter-Cre transgenic mice expressing Cre exclusively in postpartum hepatocytes to obtain Elovl6 lox/+;Cre+ mice. Subsequently, we crossed these mice to Flox mice to yield Elovl6 lox/lox;Cre+ (LKO) mice. LKO mice were born at a Mendelian ratio and newborns were physically indistinguishable from their control littermates, nursed successfully, weaned normally, and were active and fertile. (**C**) The genotype of mice harboring the null allele was confirmed by PCR using tail genomic DNA and primers P1 and P2 indicated in B to amplify a 304-bp product from the wild-type (WT) allele and a 376-bp product from the Elovl6 floxed allele (upper panel). Another PCR yielded a 100-bp band for the Cre transgene (lower panel). (**D**) qPCR analysis of *Elovl6* mRNA expression levels in various tissues. This analysis confirmed that the *Elovl6* gene deletion in LKO mice was restricted to the liver. Results are expressed as mean ± SEM

of n = 12 mice per group. ***$p < 0.001$ for LKO vs. Flox mice. (**E**) Hepatic Elovl6 activity was measured in the presence of 50 μg microsomal protein, NADH, and ^{14}C-palmitoyl-CoA. This assay further confirmed effective loss of activity in the liver of LKO mice. Results are expressed as mean ± SEM of n = 6 mice per group. ***$p <$ 0.001 for LKO vs. Flox mice. (**F**) Fatty acid composition of LKO and Flox mouse liver. Mice were fed a high-carbohydrate, fat-free diet for 3 days. Consistent with lack of hepatic Elovl6 activity, LKO mice had lower levels of Elovl6 products in liver, including stearate (C18:0) and oleate (C18:1n-9), and higher levels of palmitate (C16:0), palmitoleate (C16:1n-7), and vaccinate (C18:1n-7). These results demonstrate successful disruption of *Elovl6* in liver. Results are expressed as mean ± SEM of n = 3 mice per group. *$p < 0.05$, **$p < 0.01$, ***$p < 0.001$.

Supporting Figure 2. LKO mice are not protected from high-fat and high-sucrose (HFHS) diet-induced obesity and insulin resistance

(**A**) Body weight changes of 8-week-old male Flox and LKO mice fed a chow or HFHS diet for 12 weeks (n = 12–22 per group). (**B**) Weights of liver and eWAT from Flox and LKO mice fed a chow or a HFHS diet for 12 weeks (n = 15–20 per group). (**C**) Hepatic TAG and T-Cho levels of Flox and LKO mice fed a chow or HFHS diet for 12 weeks (n

= 12–16 per group). (**D**) Plasma concentrations of glucose and insulin of Flox and LKO mice fed a chow or HFHS diet for 12 weeks (n = 14 or 15 per group). (**E**) Plasma glucose and insulin concentrations during oral glucose tolerance tests (OGTTs) for Flox and LKO mice fed a chow or HFHS diet for 12 weeks (n = 10–14 per group). (**F**) Insulin tolerance tests (ITTs) for Flox and LKO mice fed a chow (0.5 U insulin per kg of body weight) or HFHS diet (1.0 U insulin per kg of body weight) (n = 12–25 per group). Results are expressed as mean ± SEM. *$p < 0.05$, **$p < 0.01$, ***$p < 0.001$.

Supporting Figure 3. Body and tissue weights, plasma concentrations of metabolic parameters, liver histology, and hepatic protein levels of Flox and LKO mice fed either a chow or HSD

(**A**) Body, liver, and eWAT weight in 12-weeks-old male Flox and LKO mice fed either a chow or HSD for 14 days (n = 16–23 mice per group). (**B**) Plasma triacylglycerol (TAG), total cholesterol (T-Cho), free fatty acid (FFA), and alanine aminotransferase (ALT) levels in Flox and LKO mice fed either a chow or HSD for 14 days (n = 15–24 mice per group). (**C**) Hematoxylin and eosin (H&E) staining of liver sections from representative mice from each group. Scale bar = 50 μm. (**D**) Phosphorylation of IRS-1 and IRS-2 induced by a bolus injection of insulin in livers of Flox and LKO mice on an

HSD. Blots are representative of three independent experiments. IP, immunoprecipitated; IB, immunoblotted; pY, phosphorylated tyrosine. (**E**) Immunoblot analysis of membrane and cytosolic PKCε contents in the livers of Flox and LKO mice fed an HSD for 14 days. Blots are representative of three independent experiments. Results are expressed as mean ± SEM of n = 6 mice per group. (**F**) Immunoblot analysis of Akt phosphorylation in response to bolus injection of insulin into eWAT and skeletal muscle of Flox and LKO mice fed an HSD for 14 days. Blots are representative of three independent experiments. *$p < 0.05$, **$p < 0.01$.

Supporting Figure 4. Effects of stearate and oleate supplementation and HSD feeding in LKO mice

(**A**) ITTs (0.5 U insulin per kg of body weight) for 12-weeks-old male Flox and LKO mice fed either an HSD or HSD supplemented with stearate (C18:0) and oleate (C18:1n-9) for 14 days (n = 9–15 per group). (**B**) Immunoblot analysis of SREBP-1 in the membrane fraction and nuclear extract, and lamin A/C protein in the nuclear extract from livers of Flox and LKO mice fed a regular chow diet or HSD. (**C**) qPCR analysis of lipogenic genes in the livers of Flox and LKO mice fed a chow or HSD (n = 15–29 per group). (**D**) The volcano plot of microarray analysis for differentially expressed

transcripts in the livers of HSD-fed Flox and LKO mice. Significantly up- and down-regulated genes are represented in green and orange respectively. (**E**) *Pnpla5* expression in the livers of Flox and LKO mice fed either a chow or HSD (n = 8–13 per group). (**F**) Immunoblot analysis of Pnpla3 expression in the livers of Flox and LKO mice fed a chow or HSD. *$p < 0.05$, **$p < 0.01$, ***$p < 0.001$.

Supporting Figure 5. Effects of adenovirus-mediated Pnpla3 restoration in LKO mice

(**A**) Body and liver weight in 12-weeks-old male Flox and LKO mice infected with either Ad-GFP or Ad-Pnpla3 (n = 9–16 per group). (**B**) Hepatic TAG and T-Cho levels in Flox and LKO mice infected with either Ad-GFP or Ad-Pnpla3 (n = 7–10 per group). (**C**) H&E staining of liver sections from representative mice from each group. Scale bar = 100 μm. (D) Plasma ALT and aspartate aminotransferase (AST) levels in Flox and LKO mice infected with either Ad-GFP or Ad-Pnpla3 (n = 17–20 per group). **$p < 0.01$, ***$p < 0.001$.

Supporting Figure 6. Effects of HSD feeding and adenovirus-mediated Pnpla3 restoration on ceramide contents and post-translational modification of PP2A in

the livers of Flox and LKO mice

(**A**) Relative levels of ceramide in the livers of 12-weeks-old male Flox and LKO mice fed either a chow or HSD for 14 days (n = 3–6 per group) or infected with either Ad-GFP or Ad-Pnpla3 for 7 days (n = 5–6 per group). (**B**) Immunoblot analysis of PP2A phosphorylation (Thr307) and methylation (Leu309) in the livers of Flox and LKO mice fed either a chow or HSD or infected with either Ad-GFP or Ad-Pnpla3. Blots are representative of three independent experiments.

Supporting Figure 7. Subcellular co-localization of FLAG-tagged Elovl6, HA-tagged Pnpla3, and V5-tagged CerS4 with ER and LD markers

(**A**) HEK293 cells were transfected with FLAG-tagged Elovl6, HA-tagged Pnpla3, and V5-tagged CerS4. Co-localization of Elovl6-FLAG, Pnpla3-HA, and CerS4-V5 with the ER marker calreticulin as imaged by confocal microscopy in the presence of 200 μM oleate. Scale bar = 10 μm. (**B**) Co-localization of Elovl6-FLAG, Pnpla3-HA, and CerS4-V5 with LDs detected by BODIPY as imaged by confocal microscopy in the presence of 200 μM oleate. Scale bar = 10 μm.

Supporting Figure 8. CerS4 associates with Elovl6 and Pnpla3

(**A-C**) HEK293 cells were transfected with FLAG-tagged Elovl6, HA-tagged Pnpla3, and (or) V5-tagged CerS4. Interactions of Elovl6 with CerS4 (**A**), Pnpla3 with CerS4 (**B**), and Elovl6 with Pnpla3 (**C**) were determined by immunoblotting after immunoprecipitation (IP) using the indicated antibodies.

Supporting Figure 9. Liver histology, hepatic lipid contents, and hepatic FA composition of Flox, *ob/ob*, and *ob/ob*-LKO mice, and the impact of Elovl6 deletion on hepatic insulin signaling

(**A**) H&E staining of liver sections from representative mice from each group. Scale bar = 100 μm. (**B**) Hepatic TAG and T-Cho levels in 12-week-old Flox, *ob/ob*, and *ob/ob*-LKO mice (n = 5 or 6 mice per group). (**C**) Plasma ALT levels in in 12-week-old Flox, *ob/ob*, and *ob/ob*-LKO mice (n = 10–17 mice per group). (**D**) Hepatic FA composition in Flox, *ob/ob*, and *ob/ob*-LKO mice (n = 5 mice per group). $^{**}p < 0.01$, $^{***}p < 0.001$. (**E**) Proposed models of hepatic insulin signaling for Flox and LKO mice.

SUPPORTING REFERENCES

51. Kudo T, Sato T, Hagiwara K, Kozuma Y, Yamaguchi T, Ikehara Y, Hamada M, et al. C1galt1-deficient mice exhibit thrombocytopenia due to abnormal terminal differentiation of megakaryocytes. Blood 2013;122:1649-1657.

52. Tanimoto Y, Iijima S, Hasegawa Y, Suzuki Y, Daitoku Y, Mizuno S, Ishige T, et al. Embryonic stem cells derived from C57BL/6J and C57BL/6N mice. Comp Med 2008;58:347-352.

53. Suzuki-Kemuriyama N, Matsuzaka T, Kuba M, Ohno H, Han SI, Takeuchi Y, Isaka M, et al. Different Effects of Eicosapentaenoic and Docosahexaenoic Acids on Atherogenic High-Fat Diet-Induced Non-Alcoholic Fatty Liver Disease in Mice. PLoS One 2016;11:e0157580.

54. Matsuzaka T, Atsumi A, Matsumori R, Nie T, Shinozaki H, Suzuki-Kemuriyama N, Kuba M, et al. Elovl6 promotes nonalcoholic steatohepatitis. Hepatology 2012;56:2199-2208.

55. Zhao H, Matsuzaka T, Nakano Y, Motomura K, Tang N, Yokoo T, Okajima Y, et al. Elovl6 Deficiency Improves Glycemic Control in Diabetic db/db Mice by Expanding beta-Cell Mass and Increasing Insulin Secretory Capacity. Diabetes

2017;66:1833-1846.

56. Benjamini Y, Drai D, Elmer G, Kafkafi N, Golani I. Controlling the false discovery rate in behavior genetics research. Behav Brain Res 2001;125:279-284.

57. Muranaka H, Hayashi A, Minami K, Kitajima S, Kohno S, Nishimoto Y, Nagatani N, et al. A distinct function of the retinoblastoma protein in the control of lipid composition identified by lipidomic profiling. Oncogenesis 2017;6:e350.

58. Sousa da Silva AW, Vranken WF. ACPYPE - AnteChamber PYthon Parser interfacE. BMC Res Notes 2012;5:367.

59. Ishikawa T, Ishikura T, Kuwata K. Theoretical study of the prion protein based on the fragment molecular orbital method. J Comput Chem 2009;30:2594-2601.

Supporting Table 1.

Dietary composition of high-fat and high-sucrose (HFHS) diet and high-sucrose diet (HSD)

	HFHS	HSD
Ingredient	gm%	gm%
Casein	25.0	20.0
DL-Methionine	0	0.3
Corn starch	14.869	0
Sucrose	20.0	65.0
Cellulose	5.0	5.0
Beef tallow	14.0	0
Lard	14.0	0
Soybean oil	2.0	0
Corn oil	0	5.0
Mineral mix	3.5	3.5
Vitamin mix	1.0	1.0
Choline bitartrate	0.25	0.2
Tert-butylhydroquinone	0.006	0
L-cystine	0.375	0
Total	100.0	100.0

Supporting Table 2. List of the differentially-expressed genes in the livers of HSD-fed Flox and LKO mice in microarray analysis.

pvalue	qvalue	LOGRatio	Flox gSig	LKO gSig	GenbankA	GeneSym	Description
0.01876	0.13523	−6.5703	19148.3	201.506	NM_13045	Elovl6	Mus musculus ELOVL family member 6, elongation of long chain fatty acids (yeast) (Elovl6), mRNA [NM_130450]
0.0418	0.179	−2.9322	573.328	75.1135	NM_01573	Chrna4	Mus musculus cholinergic receptor, nicotinic, alpha polypeptide 4 (Chrna4), mRNA [NM_015730]
0.00347	0.08197	−2.418	306.052	57.266	NM_05408	Pnpla3	Mus musculus patatin-like phospholipase domain containing 3 (Pnpla3), mRNA [NM_054088]
0.00866	0.09914	−2.2366	124.945	26.5112	AK05039	Crp	C-reactive protein, pentraxin-related [Source:MGI Symbol;Acc:MGI:88512] [ENSMUST00000194251]
0.02233	0.13758	−2.232	7548.7	1606.85	NM_00116	Pdzk1ip1	Mus musculus PDZK1 interacting protein 1 (Pdzk1ip1), transcript variant 1, mRNA [NM_001164557]
0.02559	0.13808	−2.2002	47.594	10.3568	NM_00117	Plekhd1	Mus musculus pleckstrin homology domain containing, family D (with coiled-coil domains) member 1 (Plekhd1), mRNA [NM_001177503]
0.02265	0.13758	−1.9938	929.018	233.254	NM_02942	Pnpla5	Mus musculus patatin-like phospholipase domain containing 5 (Pnpla5), mRNA [NM_029427]
0.01832	0.13523	−1.8656	101.919	27.9674	NM_01016	Eya4	Mus musculus eyes absent 4 homolog (Drosophila) (Eya4), mRNA [NM_010167]
0.02886	0.14702	−1.7142	33444.4	10192.7	NM_00119	Me1	Mus musculus malic enzyme 1, NADP(+)-dependent, cytosolic (Me1), transcript variant 2, mRNA [NM_001198933]
0.02473	0.13808	−1.6237	733.927	238.153	NM_00814	Gpam	Mus musculus glycerol-3-phosphate acyltransferase, mitochondrial (Gpam), mRNA [NM_008149]
0.02321	0.13758	−1.5917	355.273	117.873	NM_00128	Mme	Mus musculus membrane metallo endopeptidase (Mme), transcript variant 1, mRNA [NM_001289462]
0.00296	0.08161	−1.5906	278.871	92.5971	NM_00972	Atp2b2	Mus musculus ATPase, Ca++ transporting, plasma membrane 2 (Atp2b2), transcript variant 1, mRNA [NM_009723]
0.01589	0.1252	−1.5502	2171.63	741.53	NM_13865	Mvd	Mus musculus mevalonate (diphospho) decarboxylase (Mvd), transcript variant 1, mRNA [NM_138656]
0.0003	0.06233	−1.4906	457.868	162.939	NM_02155	Rdh11	Mus musculus retinol dehydrogenase 11 (Rdh11), mRNA [NM_021557]
0.00788	0.09914	−1.4871	3919.62	1398.25	NM_01981	Acss2	Mus musculus acyl-CoA synthetase short-chain family member 2 (Acss2), mRNA [NM_019811]
0.02143	0.13758	−1.4767	178.745	64.2237	NM_01370	Vldlr	Mus musculus very low density lipoprotein receptor (Vldlr), transcript variant 1, mRNA [NM_013703]
0.04345	0.18017	−1.4582	96925.8	35276	NM_00119	Acly	Mus musculus ATP citrate lyase (Acly), transcript variant 1, mRNA [NM_001199296]
0.01675	0.12688	−1.3997	216205	81945.6	NM_00798	Fasn	Mus musculus fatty acid synthase (Fasn), mRNA [NM_007988]
0.04625	0.1847	−1.3852	156.748	60.007	NM_13411	Eaf2	Mus musculus ELL associated factor 2 (Eaf2), transcript variant 1, mRNA [NM_134111]
0.0123	0.11535	−1.3804	2410.66	925.938	NM_01170	Vnn1	Mus musculus vanin 1 (Vnn1), mRNA [NM_011704]
0.00278	0.08161	−1.3778	159.069	61.2112	NM_00116	Aim1l	Mus musculus absent in melanoma 1-like (Aim1l), mRNA [NM_001162970]
0.00163	0.08161	−1.3762	907.635	349.642	NM_01374	Pdk4	Mus musculus pyruvate dehydrogenase kinase, isoenzyme 4 (Pdk4), mRNA [NM_013743]
0.01583	0.1252	−1.3691	1399.25	541.706	NM_13425	Rgs3	Mus musculus regulator of G-protein signaling 3 (Rgs3), transcript variant 2, mRNA [NM_134257]
0.00829	0.09914	−1.3507	148.682	58.2981	NM_01079	Meox1	Mus musculus mesenchyme homeobox 1 (Meox1), mRNA [NM_010791]
0.00217	0.08161	−1.3495	67787.3	26602	NM_00938	Thrsp	Mus musculus thyroid hormone responsive (Thrsp), mRNA [NM_009381]
0.00612	0.09914	−1.3014	101772	41293.7	NM_00747	Aqp8	Mus musculus aquaporin 8 (Aqp8), transcript variant 1, mRNA [NM_007474]
0.04143	0.17872	−1.294	91.8597	37.4632	NM_01387	Cabp2	Mus musculus calcium binding protein 2 (Cabp2), transcript variant 1, mRNA [NM_013878]
0.00844	0.09914	−1.2788	330.568	136.237	NM_00130	Nfe2	Mus musculus nuclear factor, erythroid derived 2 (Nfe2), transcript variant 1, mRNA [NM_001302338]
0.00121	0.08161	−1.2672	105.494	43.8298	NM_17747	Ccdc69	Mus musculus coiled-coil domain containing 69 (Ccdc69), mRNA [NM_177471]
0.00486	0.08695	−1.2612	4860.11	2027.59	NM_00904	Rdh16	Mus musculus retinol dehydrogenase 16 (Rdh16), mRNA [NM_009040]
0.00138	0.08161	−1.2591	53618.4	22402.2	NM_14594	Hmgcs1	Mus musculus 3-hydroxy-3-methylglutaryl-Coenzyme A synthase 1 (Hmgcs1), transcript variant 1, mRNA [NM_145942]
0.02735	0.14306	−1.2457	5030.66	2121.44	NM_02445	Scd3	Mus musculus stearoyl-coenzyme A desaturase 3 (Scd3), mRNA [NM_024450]
0.04708	0.18675	−1.2315	80.7831	34.4031	NM_01186	Slc26a4	Mus musculus solute carrier family 26, member 4 (Slc26a4), mRNA [NM_011867]
0.00881	0.09914	−1.205	71.0768	30.8317	NM_01383	Pstpip2	Mus musculus proline-serine-threonine phosphatase-interacting protein 2 (Pstpip2), mRNA [NM_013831]
0.01168	0.11167	−1.1606	2304.65	1030.96	NM_00934	Dntt	Mus musculus deoxynucleotidyltransferase, terminal (Dntt), transcript variant 1, mRNA [NM_009345]
0.01053	0.10921	−1.1557	6131.44	2752	NM_00108	Pgd	Mus musculus phosphogluconate dehydrogenase (Pgd), mRNA [NM_001081274]
0.01643	0.12688	−1.1547	1178.04	529.141	BC11441	Scd1	Mus musculus cDNA clone IMAGE:40040818. [BC114417]
0.0136	0.11996	−1.1093	58.8163	27.2619	NM_00108	Unc79	Mus musculus unc-79 homolog (C. elegans) (Unc79), mRNA [NM_001081017]
0.04554	0.1831	−1.1084	62.119	28.8114	NM_17229	Sulf1	Mus musculus sulfatase 1 (Sulf1), transcript variant 2, mRNA [NM_172294]
0.00307	0.08161	−1.1075	47.609	22.0956	NM_00116	Sgsm1	Mus musculus small G protein signaling modulator 1 (Sgsm1), transcript variant 3, mRNA [NM_001162965]
0.01348	0.11996	−1.1046	136.999	63.7111	NM_02889	Lonrf3	Mus musculus LON peptidase N-terminal domain and ring finger 3 (Lonrf3), mRNA [NM_028894]
0.00129	0.08161	−1.0896	1357.9	638.065	NM_14600	Lss	Mus musculus lanosterol synthase (Lss), mRNA [NM_146006]
0.003	0.08161	−1.086	4564.23	2150.01	NM_01094	Nsdhl	Mus musculus NAD(P) dependent steroid dehydrogenase-like (Nsdhl), mRNA [NM_010941]
0.00181	0.08161	−1.0834	1312.74	619.501	NM_01039	H2-Q1	Mus musculus histocompatibility 2, Q region locus 1 (H2-Q1), mRNA [NM_010390]
0.0151	0.12226	−1.0822	12509.1	5908.2	NM_00927	Sqle	Mus musculus squalene epoxidase (Sqle), mRNA [NM_009270]
0.01912	0.1357	−1.079	175.938	83.2788	AK13795	Cenpc1	centromere protein C1 [Source:MGI Symbol;Acc:MGI:99700] [ENSMUST00000198059]
0.03116	0.14973	−1.0704	107.412	51.1467	NM_00114	Gpd2	Mus musculus glycerol phosphate dehydrogenase 2, mitochondrial (Gpd2), transcript variant 1, mRNA [NM_001145820]
0.00245	0.08161	−1.059	83659.7	40153.7	NM_00125	Fdps	Mus musculus farnesyl diphosphate synthetase (Fdps), transcript variant 1, mRNA [NM_001253751]
0.04429	0.18017	−1.0584	16888.9	8109.59	NM_13390	Acacb	Mus musculus acetyl-Coenzyme A carboxylase beta (Acacb), mRNA [NM_133904]
0.00583	0.09846	−1.0549	71.7502	34.5359	NM_17806	Thra	Mus musculus thyroid hormone receptor alpha (Thra), mRNA [NM_178060]
0.04045	0.17755	−1.0476	641.029	310.109	NM_00125	Cyp4a31	Mus musculus cytochrome P450, family 4, subfamily a, polypeptide 31 (Cyp4a31), transcript variant 2, mRNA [NM_001252539]
0.0041	0.08695	−1.038	838.099	408.162	NM_01667	Reck	Mus musculus reversion-inducing-cysteine-rich protein with kazal motifs (Reck), mRNA [NM_016678]
0.02052	0.13625	−1.0336	644.455	314.801	XM_01124	Elovl5	PREDICTED: Mus musculus ELOVL family member 5, elongation of long chain fatty acids (yeast) (Elovl5), transcript variant X2, mRNA [XM_011242807]
0.03811	0.17193	−1.0278	634.977	311.426	NM_00784	Defb1	Mus musculus defensin beta 1 (Defb1), mRNA [NM_007843]
0.01094	0.10959	−1.0229	198.275	97.5765	NM_00103	Nell1	Mus musculus NEL-like 1 (Nell1), mRNA [NM_001037906]
0.0308	0.14921	−1.0182	311.347	153.717	NM_00970	Aqp4	Mus musculus aquaporin 4 (Aqp4), mRNA [NM_009700]
0.0344	0.15745	−1.0127	80.9507	40.1196	NM_19863	Acss3	Mus musculus acyl-CoA synthetase short-chain family member 3 (Acss3), transcript variant 2, mRNA [NM_198636]
0.01487	0.12204	−1.0105	72.7734	36.1231	NM_00902	Rasgrf2	Mus musculus RAS protein-specific guanine nucleotide-releasing factor 2 (Rasgrf2), mRNA [NM_009027]
0.00835	0.09914	1.01601	94445.4	190998	NR_00328	Rs5-8s1	Mus musculus 5.8S ribosomal RNA (Rs5-8s1), ribosomal RNA [NR_003280]
0.00482	0.08695	1.05036	25.3356	52.4712	XM_01123	Wdfy1	WD repeat and FYVE domain containing 1 [Source:MGI Symbol;Acc:MGI:1916618] [ENSMUST00000125641]
0.02193	0.13758	1.08155	97.3013	205.92	NM_00111	Adam11	Mus musculus a disintegrin and metallopeptidase domain 11 (Adam11), transcript variant 1, mRNA [NM_001110778]
0.04407	0.18017	1.08581	23101.7	49034.8	NM_00101	Ang6	Mus musculus angiogenin, ribonuclease A family, member 6 (Ang6), mRNA [NM_001011876]
0.02875	0.14702	1.09109	673.51	1434.81	NM_00116	Tead1	Mus musculus TEA domain family member 1 (Tead1), transcript variant 1, mRNA [NM_001166584]
0.02985	0.14702	1.09813	6233.95	13345.5	XM_00653	Cyp7b1	PREDICTED: Mus musculus cytochrome P450, family 7, subfamily b, polypeptide 1 (Cyp7b1), transcript variant X2, mRNA [XM_006535384]
0.00072	0.07141	1.0997	35.7608	76.6387	NM_01107	Abcb1b	Mus musculus ATP-binding cassette, sub-family B (MDR/TAP), member 1B (Abcb1b), mRNA [NM_011075]
0.00656	0.09914	1.10718	1076.57	2319.2	NM_00111	Shank2	Mus musculus SH3/ankyrin domain gene 2 (Shank2), transcript variant 2, mRNA [NM_001113373]
0.01655	0.12688	1.11516	1354.49	2934.07	NM_02862	Psd	Mus musculus pleckstrin and Sec7 domain containing (Psd), mRNA [NM_028627]
0.0221	0.13758	1.12381	120.819	263.291	AK03777	Cry2	cryptochrome 2 (photolyase-like) [Source:MGI Symbol;Acc:MGI:1270859] [ENSMUST00000125488]
0.04105	0.17837	1.13932	2043.57	4501.51	NM_00780	Cyb561	Mus musculus cytochrome b-561 (Cyb561), mRNA [NM_007805]
0.04777	0.18821	1.16433	25.7461	57.7045	NM_17298	Nkain3	Mus musculus Na+/K+ transporting ATPase interacting 3 (Nkain3), transcript variant 2, mRNA [NM_172987]
0.0087	0.09914	1.16749	132.675	298.014	NM_14544	Mfsd7c	Mus musculus major facilitator superfamily domain containing 7C (Mfsd7c), mRNA [NM_145447]
0.00867	0.09914	1.17045	91.9048	206.862	NR_10505	Dreh	Mus musculus down-regulated in hepatocellular carcinoma (Dreh), long non-coding RNA [NR_105051]
0.03441	0.15745	1.18695	36.4536	82.9941	NM_01205	Asns	Mus musculus asparagine synthetase (Asns), mRNA [NM_012055]
0.00294	0.08161	1.20512	22.4315	51.7173	BC05140	Dnah3	Mus musculus dynein, axonemal, heavy chain 3, mRNA (cDNA clone IMAGE:6390305), partial cds. [BC051401]
0.00937	0.09996	1.21152	179.635	416.003	AB04240	Gsdmc	Mus musculus MLZE mRNA, complete cds. [AB042406]
0.00806	0.09914	1.21184	35.5176	82.2705	NM_00108	Fam65b	Mus musculus family with sequence similarity 65, member B (Fam65b), transcript variant 2, mRNA [NM_001080381]
0.02491	0.13808	1.21554	174.812	405.961	NM_00128	Upp2	Mus musculus uridine phosphorylase 2 (Upp2), transcript variant 2, mRNA [NM_001289660]
0.00469	0.08695	1.22675	130.418	305.229	NM_00108	Slc16a5	Mus musculus solute carrier family 16 (monocarboxylic acid transporters), member 5 (Slc16a5), mRNA [NM_001080934]
0.02312	0.13758	1.23203	53350	125318	NM_14559	Fgl1	Mus musculus fibrinogen-like protein 1 (Fgl1), mRNA [NM_145594]
0.01993	0.1357	1.2877	471.854	1151.98	NM_14681	Olfr1218	Mus musculus olfactory receptor 1218 (Olfr1218), mRNA [NM_146818]
0.04031	0.17755	1.30383	49.8127	122.979	NM_00114	Capn8	Mus musculus calpain 8 (Capn8), transcript variant 2, mRNA [NM_001145806]
0.00947	0.09996	1.36701	21.0922	54.4042	NM_13425	Havcr2	Mus musculus hepatitis A virus cellular receptor 2 (Havcr2), mRNA [NM_134250]
0.01169	0.11167	1.3777	105.876	275.123	NM_14479	Pycr1	Mus musculus pyrroline-5-carboxylate reductase 1 (Pycr1), mRNA [NM_144795]
0.04398	0.18017	1.38371	32.8974	85.8417	NM_00115	Lnx1	Mus musculus ligand of numb-protein X 1 (Lnx1), transcript variant 1, mRNA [NM_001159577]
0.02561	0.13808	1.3958	21.7948	57.3496	NM_00112	Adgb	Mus musculus androglobin (Adgb), mRNA [NM_001127353]
0.00051	0.07141	1.39811	41.2749	108.783	NM_00788	Usp17la	Mus musculus ubiquitin specific peptidase 17-like A (Usp17la), mRNA [NM_007887]
0.00508	0.08824	1.43028	22.2687	60.0137	NM_02978	Fam81a	Mus musculus family with sequence similarity 81, member A (Fam81a), mRNA [NM_029784]
0.01327	0.11996	1.45762	17.9423	49.2794	NM_14652	Olfr536	Mus musculus olfactory receptor 536 (Olfr536), mRNA [NM_146520]
0.04002	0.17755	1.47298	15.4055	42.7651	NM_15355	Dennd1c	Mus musculus DENN/MADD domain containing 1C (Dennd1c), mRNA [NM_153551]
0.0141	0.12012	1.48929	146.434	411.116	XM_00651	Nnmt	nicotinamide N-methyltransferase [Source:MGI Symbol;Acc:MGI:1099443] [ENSMUST00000034808]
0.04056	0.17755	1.52587	142.392	410.032	NM_02890	Scara5	Mus musculus scavenger receptor class A, member 5 (putative) (Scara5), transcript variant 1, mRNA [NM_028903]
0.00157	0.08161	1.56693	178.192	527.935	NM_02640	Dnajb11	Mus musculus DnaJ (Hsp40) homolog, subfamily B, member 11 (Dnajb11), transcript variant 1, mRNA [NM_026400]
0.04242	0.18017	1.57153	124.413	369.78	NM_02876	Cep55	Mus musculus centrosomal protein 55 (Cep55), transcript variant 2, mRNA [NM_028760]
0.03352	0.15745	1.57457	235.455	701.296	NM_00814	Gnat1	Mus musculus guanine nucleotide binding protein, alpha transducing 1 (Gnat1), mRNA [NM_008140]
0.02647	0.13966	1.66262	1104.83	3497.78	NM_18103	Adgrl1	Mus musculus adhesion G protein-coupled receptor L1 (Adgrl1), mRNA [NM_181039]
0.04964	0.19427	1.72344	14.2513	47.0612	NM_14583	Lin28a	Mus musculus lin-28 homolog A (C. elegans) (Lin28a), mRNA [NM_145833]
0.01313	0.11996	1.76696	12.3301	41.964	AK03587	Lgi1	leucine-rich repeat LGI family, member 1 [Source:MGI Symbol;Acc:MGI:1861691] [ENSMUST00000134832]
0.00717	0.09914	1.83598	2934	10474.8	NM_02714	Enho	Mus musculus energy homeostasis associated (Enho), mRNA [NM_027147]
0.02593	0.13808	1.8429	11.8533	42.5216	AK04760	Sufu	suppressor of fused homolog (Drosophila) [Source:MGI Symbol;Acc:MGI:1345643] [ENSMUST00000118440]
0.01423	0.12012	1.89952	17.9725	67.0533	NM_00130	Esr1	Mus musculus estrogen receptor 1 (alpha) (Esr1), transcript variant 4, mRNA [NM_001302533]
0.02593	0.13808	1.91584	9.1116	34.3811	NM_02858	Marveld3	Mus musculus MARVEL (membrane-associating) domain containing 3 (Marveld3), transcript variant 1, mRNA [NM_028584]
0.00717	0.09914	2.11012	9.64451	41.6381	AK08777	Sox5	SRY (sex determining region Y)-box 5 [Source:MGI Symbol;Acc:MGI:98367] [ENSMUST00000149451]
0.00889	0.09914	2.23736	14.0824	66.4036	NM_00113	Hpca	Mus musculus hippocalcin (Hpca), transcript variant 1, mRNA [NM_001130419]
0.04419	0.18017	2.40037	301.706	1592.82	NM_02444	Derl3	Mus musculus Der1-like domain family, member 3 (Derl3), mRNA [NM_024440]
0.00484	0.08695	3.15665	40670.5	362682	NM_00911	Saa1	Mus musculus serum amyloid A 1 (Saa1), mRNA [NM_009117]
0.00381	0.08661	3.36661	48050.1	495617	NM_01131	Saa2	Mus musculus serum amyloid A 2 (Saa2), mRNA [NM_011314]

Supporting Table 3. Lipidomic changes in the livers of HSD-fed Flox and LKO mice infected with either Ad-GFP or Ad-Pnpla3

Effect_name		01_LKO_GFP_vs_Control_GFP	02_LKO_PNPLA3_vs_Control_PNPLA3	03_Control_PNPLA3_vs_Control_GFP	04_LKO_PNPLA3_vs_LKO_GFP	01_LKO_GFP_vs_Control_GFP	02_LKO_PNPLA3_vs_Control_PNPLA3	03_Control_PNPLA3_vs_Control_GFP	04_LKO_PNPLA3_vs_LKO_GFP
ONTOLOGY2_NAME	METABOLITE_NAME	Ratio	Ratio	Ratio	Ratio	p.value	p.value	p.value	p.value
Ceramides	CER_Ceramide (d16:1,C16:0)	1.13	1.09	1.09	1.06	0.5366	0.6248	0.6405	0.7429
Ceramides	CER_Ceramide (d16:1,C18:0)	0.72	0.78	0.96	1.04	0.0041	0.0166	0.6773	0.6636
Ceramides	CER_Ceramide (d16:1,C20:0)	0.63	0.67	0.77	0.82	0.0002	0.0004	0.0160	0.0384
Ceramides	CER_Ceramide (d16:1,C22:0)	0.60	0.58	0.77	0.74	0.0005	0.0002	0.0368	0.0156
Ceramides	CER_Ceramide (d16:1,C23:0)	1.06	1.29	0.70	0.86	0.7376	0.1290	0.0563	0.3572
Ceramides	CER_Ceramide (d16:1,C24:0)	0.90	0.84	0.90	0.85	0.5536	0.3276	0.5767	0.3452
Ceramides	CER_Ceramide (d16:1,C24:1)	0.83	0.97	0.75	0.88	0.3289	0.8696	0.1437	0.4748
Ceramides	CER_Ceramide (d17:1,C16:0)	1.15	1.13	1.12	1.10	0.4877	0.5198	0.5694	0.6096
Ceramides	CER_Ceramide (d17:1,C18:0)	0.58	0.64	0.90	1.00	8.91E-05	0.0004	0.3478	0.9763
Ceramides	CER_Ceramide (d17:1,C20:0)	0.58	0.57	0.81	0.80	0.0003	0.0001	0.0987	0.0633
Ceramides	CER_Ceramide (d17:1,C22:0)	0.62	0.59	0.79	0.74	0.0034	0.0008	0.0956	0.0319
Ceramides	CER_Ceramide (d17:1,C23:0)	1.23	1.19	0.69	0.67	0.3451	0.4022	0.1000	0.0604
Ceramides	CER_Ceramide (d17:1,C24:0)	0.87	0.85	0.94	0.93	0.5548	0.4806	0.8113	0.7383
Ceramides	CER_Ceramide (d17:1,C24:1)	0.72	1.05	0.67	0.97	0.0316	0.7123	0.0107	0.8440
Ceramides	CER_Ceramide (d18:0,C16:0)	1.15	1.14	1.54	1.52	0.5523	0.5574	0.0862	0.0764
Ceramides	CER_Ceramide (d18:0,C18:0)	0.74	0.55	1.46	1.08	0.3518	0.0613	0.2483	0.7906
Ceramides	CER_Ceramide (d18:0,C20:0)	0.65	0.60	1.11	1.03	0.2038	0.1179	0.7527	0.9288
Ceramides	CER_Ceramide (d18:0,C22:0)	0.69	0.62	1.05	0.94	0.2430	0.1167	0.8783	0.8362
Ceramides	CER_Ceramide (d18:0,C24:1)	1.02	1.20	0.99	1.16	0.9553	0.5479	0.9621	0.6221
Ceramides	CER_Ceramide (d18:1,C14:0)	1.29	1.20	1.04	0.97	0.0761	0.1711	0.7771	0.7852
Ceramides	CER_Ceramide (d18:1,C16:0)	1.11	1.13	1.40	1.43	0.6373	0.5467	0.1281	0.0897
Ceramides	CER_Ceramide (d18:1,C18:0)	0.63	0.64	1.24	1.26	0.0028	0.0023	0.1139	0.0778
Ceramides	CER_Ceramide (d18:1,C19:0)	0.93	1.11	0.97	1.17	0.7362	0.6086	0.9007	0.4634
Ceramides	CER_Ceramide (d18:1,C20:0)	0.59	0.55	1.06	0.99	0.0003	4.56E-05	0.6193	0.8954
Ceramides	CER_Ceramide (d18:1,C21:0)	1.00	1.07	0.88	0.94	0.9836	0.7248	0.5314	0.7362
Ceramides	CER_Ceramide (d18:1,C22:0)	0.68	0.57	1.11	0.94	0.0018	3.59E-05	0.3200	0.5041
Ceramides	CER_Ceramide (d18:1,C22:1)	1.58	1.67	0.87	0.92	0.0296	0.0115	0.4645	0.6453
Ceramides	CER_Ceramide (d18:1,C23:0)	1.26	1.19	0.97	0.92	0.2292	0.3252	0.8604	0.6227
Ceramides	CER_Ceramide (d18:1,C23:1)	1.05	1.21	0.87	1.00	0.8074	0.3357	0.5141	0.9821
Ceramides	CER_Ceramide (d18:1,C24:0)	1.01	0.98	1.17	1.13	0.9441	0.8985	0.3651	0.4445
Ceramides	CER_Ceramide (d18:1,C24:1)	1.04	0.98	1.18	1.11	0.8213	0.9056	0.3612	0.5353
Ceramides	CER_Ceramide (d18:1,C24:2)	1.36	1.40	1.28	1.33	0.0589	0.0297	0.1166	0.0640
Ceramides	CER_Ceramide (d18:2,C14:0)	1.19	1.17	0.83	0.81	0.4404	0.4708	0.4193	0.3418
Ceramides	CER_Ceramide (d18:2,C16:0)	1.06	1.14	1.11	1.20	0.7620	0.4261	0.5716	0.2869
Ceramides	CER_Ceramide (d18:2,C18:0)	0.72	0.86	1.01	1.21	0.0325	0.2610	0.9287	0.1742
Ceramides	CER_Ceramide (d18:2,C20:0)	0.61	0.69	0.81	0.92	0.0014	0.0074	0.1182	0.4841
Ceramides	CER_Ceramide (d18:2,C21:0)	1.06	1.07	0.82	0.83	0.7704	0.7016	0.3172	0.3229
Ceramides	CER_Ceramide (d18:2,C22:0)	0.71	0.62	0.86	0.75	0.0657	0.0104	0.3863	0.0971
Ceramides	CER_Ceramide (d18:2,C22:1)	1.68	1.77	0.63	0.67	0.0464	0.0219	0.0720	0.0923
Ceramides	CER_Ceramide (d18:2,C23:0)	1.25	1.40	0.74	0.82	0.2677	0.0887	0.1363	0.3014
Ceramides	CER_Ceramide (d18:2,C24:0)	0.87	0.93	0.96	1.02	0.3058	0.5520	0.7505	0.8652
Ceramides	CER_Ceramide (d18:2,C24:1)	1.00	1.07	0.87	0.94	0.9898	0.6843	0.4495	0.6982
Cholesterylesters	CE_Cholesterylester C14:1	1.65	**2.12**	0.80	1.03	0.0344	0.0032	0.3166	0.9049
Cholesterylesters	CE_Cholesterylester C16:0	1.68	1.80	1.00	1.07	0.0145	0.0070	0.9953	0.7277
Cholesterylesters	CE_Cholesterylester C16:1	1.91	**2.09**	0.86	0.95	0.0042	0.0016	0.4583	0.7743
Cholesterylesters	CE_Cholesterylester C18:0	**0.49**	**0.43**	1.04	0.92	0.0088	0.0032	0.8822	0.7503
Cholesterylesters	CE_Cholesterylester C18:1	0.65	0.68	0.94	0.98	0.0389	0.0587	0.7377	0.9007
Cholesterylesters	CE_Cholesterylester C18:2	1.03	1.05	1.02	1.04	0.8397	0.7142	0.9120	0.7835
Cholesterylesters	CE_Cholesterylester C18:3	1.16	1.05	0.96	0.86	0.3071	0.7434	0.7498	0.3109
Cholesterylesters	CE_Cholesterylester C18:4	1.41	1.05	0.83	0.62	0.1109	0.8011	0.3812	0.0331
Cholesterylesters	CE_Cholesterylester C20:1	0.75	0.90	0.68	0.82	0.2713	0.6961	0.1474	0.4463
Cholesterylesters	CE_Cholesterylester C20:2	0.79	0.90	0.62	0.71	0.3741	0.6873	0.0829	0.1973
Cholesterylesters	CE_Cholesterylester C20:3	0.84	0.92	0.74	0.81	0.4304	0.6890	0.1837	0.3379
Cholesterylesters	CE_Cholesterylester C20:4	0.88	0.94	0.95	1.02	0.3722	0.6715	0.7540	0.8693
Cholesterylesters	CE_Cholesterylester C20:5	1.27	1.08	1.00	0.85	0.1499	0.6166	0.9943	0.3347
Cholesterylesters	CE_Cholesterylester C22:1	1.10	1.29	0.94	1.10	0.7239	0.3458	0.8019	0.7259
Cholesterylesters	CE_Cholesterylester C22:3	0.59	0.81	0.51	0.71	0.1355	0.5466	0.0649	0.3201

Cholesterylesters	CE_Cholesterylester C22:4	0.88	0.92	0.77	0.80	0.7349	0.8249	0.4952	0.5710
Cholesterylesters	CE_Cholesterylester C22:6	1.09	1.23	0.96	1.09	0.6243	0.2425	0.8143	0.6409
Cholesterylesters	CE_Cholesterylester C24:4	0.61	0.87	0.90	1.29	0.1909	0.7115	0.7847	0.4870
Cholesterylesters	CE_Cholesterylester C24:5	0.73	1.06	0.51	0.74	0.2678	0.8369	0.0254	0.2848
Cholesterylesters	CE_Cholesterylester C24:6	1.07	1.32	**0.34**	**0.42**	0.8207	0.3721	0.0029	0.0123
Diacylglycerols	DAG_Palmitic acid (C16:0)	1.12	1.20	0.96	1.03	0.1933	0.0447	0.6279	0.7486
Free fatty acids	FFA_Arachidonic acid (C20:cis[5,8,11,14]4)	1.08	0.81	0.51	**0.38**	0.7720	0.4310	0.0244	0.0025
Free fatty acids	FFA_cis-Vaccenic acid (C18:cis[11]1)	1.61	1.74	0.66	0.71	0.0815	0.0465	0.1245	0.2046
Free fatty acids	FFA_dihomo-gamma-Linolenic acid (C20:cis[8,11,14]3)	1.07	0.96	**0.26**	**0.24**	0.8702	0.9100	0.0034	0.0019
Free fatty acids	FFA_Docosatetraenoic acid (C22:cis[7,10,13,16]4)	1.00	0.63	**0.37**	**0.23**	0.9913	0.2850	0.0310	0.0031
Free fatty acids	FFA_Eicosadienoic acid (C20:cis[11,14]2)	0.88	1.63	**0.17**	**0.31**	0.7854	0.2889	0.0011	0.0192
Free fatty acids	FFA_Eicosaenoic acid (C20:cis[11]1)	0.59	0.74	**0.38**	**0.48**	0.0697	0.2791	0.0028	0.0155
Free fatty acids	FFA_Eicosanoic acid (C20:0)	0.60	0.57	0.81	0.78	0.0398	0.0262	0.3816	0.2835
Free fatty acids	FFA_Eicosapentaenoic acid (C20:cis[5,8,11,14,17]5)	**2.75**	1.28	1.00	**0.47**	0.0104	0.4883	1.0000	0.0434
Free fatty acids	FFA_Elaidic acid (C18:trans[9]1)	0.55	0.60	0.81	0.88	0.0069	0.0167	0.2922	0.5165
Free fatty acids	FFA_Erucic acid (C22:cis[13]1)	0.78	0.88	0.58	0.66	0.1582	0.4683	0.0059	0.0270
Free fatty acids	FFA_gamma-Linolenic acid (C18:cis[6,9,12]3)	1.43	0.95	0.78	0.52	0.3548	0.8961	0.5276	0.1026
Free fatty acids	FFA_Linoleic acid (C18:cis[9,12]2)	1.28	1.09	0.83	0.71	0.3990	0.7609	0.5190	0.2414
Free fatty acids	FFA_Linolenic acid (C18:cis[9,12,15]3)	1.33	1.48	**0.50**	0.55	0.4988	0.3633	0.1131	0.1713
Free fatty acids	FFA_Oleic acid (C18:cis[9]1)	0.73	0.64	0.97	0.86	0.2394	0.1082	0.9146	0.5646
Free fatty acids	FFA_Palmitic acid (C16:0)	1.50	1.36	1.00	0.91	0.0818	0.1786	0.9955	0.6627
Free fatty acids	FFA_Palmitoleic acid (C16:cis[9]1)	**2.67**	**2.42**	1.06	0.97	0.0096	0.0173	0.8584	0.9175
Free fatty acids	FFA_Stearic acid (C18:0)	0.77	0.75	0.97	0.94	0.0113	0.0052	0.7613	0.5034
Lysophosphatidylcholines	LPC_Arachidonic acid (C20:cis[5,8,11,14]4)	0.88	0.84	0.98	0.94	0.1822	0.0723	0.8391	0.4726
Lysophosphatidylcholines	LPC_Linoleic acid (C18:cis[9,12]2)	1.09	1.00	1.00	0.92	0.3194	0.9672	0.9535	0.3274
Lysophosphatidylcholines	LPC_Palmitic acid (C16:0)	1.16	1.31	0.93	1.04	0.1732	0.0219	0.4963	0.6828
Lysophosphatidylcholines	LPC_Stearic acid (C18:0)	0.60	0.59	1.01	1.01	0.0001	0.0001	0.9263	0.9520
Monoacylglycerols	MAG_Erucic acid (C22:cis[13]1)	1.10	1.15	1.00	1.05	0.4815	0.3140	0.9811	0.7361
Monoacylglycerols	MAG_Linoleic acid (C18:cis[9,12]2)	1.30	1.26	0.58	0.56	0.5827	0.6281	0.2550	0.2301
Monoacylglycerols	MAG_Stearic acid (C18:0)	0.95	1.09	1.01	1.17	0.6854	0.4926	0.9362	0.2491
Phosphatidylcholines	PC_Arachidonic acid (C20:cis[5,8,11,14]4)	0.96	0.90	1.02	0.96	0.5779	0.1673	0.8004	0.5431
Phosphatidylcholines	PC_Behenic acid (C22:0)	1.10	0.86	1.08	0.84	0.5439	0.3398	0.6159	0.2908
Phosphatidylcholines	PC_cis-Vaccenic acid (C18:cis[11]1)	1.45	1.57	0.87	0.94	0.0175	0.0055	0.3313	0.6623
Phosphatidylcholines	PC_dihomo-gamma-Linolenic acid (C20:cis[8,11,14]3)	1.04	0.97	0.98	0.92	0.4419	0.5827	0.7359	0.1099
Phosphatidylcholines	PC_Docosahexaenoic acid (C22:cis[4,7,10,13,16,19]6)	1.06	1.07	0.97	0.98	0.4137	0.3189	0.6054	0.7401
Phosphatidylcholines	PC_Docosapentaenoic acid (C22:cis[4,7,10,13,16]5)	0.78	1.02	0.72	0.95	0.3155	0.9478	0.2020	0.8229
Phosphatidylcholines	PC_Docosapentaenoic acid (C22:cis[7,10,13,16,19]5)	1.31	1.16	1.06	0.94	0.0040	0.0826	0.4759	0.4493
Phosphatidylcholines	PC_Docosatetraenoic acid (C22:cis[7,10,13,16]4)	1.03	1.08	1.07	1.11	0.8205	0.6151	0.6444	0.4627
Phosphatidylcholines	PC_Eicosadienoic acid (C20:cis[11,14]2)	1.03	1.19	0.93	1.08	0.7141	0.0504	0.4194	0.3744
Phosphatidylcholines	PC_Eicosaenoic acid (C20:cis[11]1)	0.70	0.79	0.92	1.04	0.0127	0.0760	0.5387	0.7822
Phosphatidylcholines	PC_Eicosanoic acid (C20:0)	0.58	0.58	0.91	0.90	0.0009	0.0009	0.4707	0.4620
Phosphatidylcholines	PC_Eicosapentaenoic acid (C20:cis[5,8,11,14,17]5)	1.18	1.12	**2.58**	**2.44**	0.7897	0.8608	0.1437	0.1679
Phosphatidylcholines	PC_Elaidic acid (C18:trans[9]1)	0.77	0.72	0.99	0.93	0.0852	0.0391	0.9585	0.6483
Phosphatidylcholines	PC_gamma-Linolenic acid (C18:cis[6,9,12]3)	1.37	1.06	0.91	0.70	0.1342	0.7747	0.6315	0.0949
Phosphatidylcholines	PC_Linoleic acid (C18:cis[9,12]2)	1.13	1.12	0.99	0.98	0.1220	0.1617	0.8885	0.7621
Phosphatidylcholines	PC_Myristic acid (C14:0)	1.33	1.13	1.12	0.95	0.3641	0.6946	0.7075	0.8808
Phosphatidylcholines	PC_Oleic acid (C18:cis[9]1)	0.69	0.69	0.98	0.99	1.09E-05	1.46E-05	0.7803	0.8982
Phosphatidylcholines	PC_Palmitic acid (C16:0)	1.32	1.29	1.02	1.00	6.40E-06	2.06E-05	0.5818	0.9461
Phosphatidylcholines	PC_Palmitoleic acid (C16:cis[9]1)	1.67	1.60	0.90	0.87	0.0005	0.0011	0.4053	0.2413
Phosphatidylcholines	PC_Stearic acid (C18:0)	**0.48**	**0.46**	1.02	0.97	3.36E-07	1.38E-07	0.7903	0.7630
Phosphatidylcholines	PC_trans-Vaccenic acid (C18:trans[11]1)	1.21	1.29	0.84	0.89	0.2449	0.1233	0.2685	0.4778
Phosphatidylethanolamines	PE_Arachidonic acid (C20:cis[5,8,11,14]4)	1.05	0.90	1.08	0.93	0.6105	0.3099	0.4313	0.4577
Phosphatidylethanolamines	PE_cis-Vaccenic acid (C18:cis[11]1)	1.65	1.56	1.06	0.99	0.0001	0.0005	0.6011	0.9567
Phosphatidylethanolamines	PE_dihomo-gamma-Linolenic acid (C20:cis[8,11,14]3)	1.00	0.89	1.05	0.94	0.9606	0.2181	0.6107	0.4864
Phosphatidylethanolamines	PE_Docosahexaenoic acid (C22:cis[4,7,10,13,16,19]6)	1.34	1.11	1.20	0.99	0.0478	0.4508	0.2075	0.9558
Phosphatidylethanolamines	PE_Docosapentaenoic acid (C22:cis[7,10,13,16,19]5)	1.48	1.16	1.22	0.96	0.0026	0.1875	0.0893	0.7096
Phosphatidylethanolamines	PE_Docosatetraenoic acid (C22:cis[7,10,13,16]4)	1.13	1.03	1.24	1.13	0.5317	0.8790	0.2778	0.5320
Phosphatidylethanolamines	PE_Eicosadienoic acid (C20:cis[11,14]2)	1.11	0.95	1.33	1.14	0.5796	0.7901	0.1486	0.5053
Phosphatidylethanolamines	PE_Eicosaenoic acid (C20:cis[11]1)	0.84	0.81	1.07	1.03	0.1746	0.0963	0.5878	0.8386
Phosphatidylethanolamines	PE_Eicosanoic acid (C20:0)	0.98	0.75	1.18	0.90	0.8909	0.0816	0.3044	0.5199
Phosphatidylethanolamines	PE_Elaidic acid (C18:trans[9]1)	0.81	0.79	1.05	1.03	0.0929	0.0605	0.6656	0.8380
Phosphatidylethanolamines	PE_Linoleic acid (C18:cis[9,12]2)	1.14	1.02	1.04	0.93	0.0758	0.7894	0.5405	0.3315
Phosphatidylethanolamines	PE_Oleic acid (C18:cis[9]1)	0.77	0.72	1.05	0.98	0.0152	0.0039	0.6364	0.8649
Phosphatidylethanolamines	PE_Palmitic acid (C16:0)	1.57	1.42	1.11	1.00	2.87E-05	0.0004	0.2089	0.9693
Phosphatidylethanolamines	PE_Palmitoleic acid (C16:cis[9]1)	**2.16**	**2.11**	0.88	0.86	8.49E-06	1.21E-05	0.2822	0.2108
Phosphatidylethanolamines	PE_Stearic acid (C18:0)	0.73	0.62	1.20	1.02	0.0032	6.85E-05	0.0567	0.8488
Phosphatidylinositols	PI_Arachidonic acid (C20:cis[5,8,11,14]4)	0.93	0.89	1.02	0.99	0.2069	0.0699	0.7166	0.8001
Phosphatidylinositols	PI_cis-Vaccenic acid (C18:cis[11]1)	1.74	**2.10**	0.88	1.06	0.0030	0.0002	0.4377	0.6974
Phosphatidylinositols	PI_dihomo-gamma-Linolenic acid (C20:cis[8,11,14]3)	1.19	1.14	1.06	1.02	0.1975	0.3260	0.6533	0.9009
Phosphatidylinositols	PI_Docosahexaenoic acid (C22:cis[4,7,10,13,16,19]6)	1.24	1.30	1.07	1.13	0.0365	0.0122	0.4753	0.2212
Phosphatidylinositols	PI_Eicosanoic acid (C20:0)	1.61	1.56	1.05	1.01	0.3819	0.4177	0.9336	0.9863
Phosphatidylinositols	PI_Linoleic acid (C18:cis[9,12]2)	1.39	1.43	1.08	1.11	0.0211	0.0136	0.5567	0.4267

Phosphatidylinositols	PI_Palmitic acid (C16:0)	1.95	**2.20**	0.99	1.12	6.92E-05	1.16E-05	0.9619	0.3900
Phosphatidylinositols	PI_Stearic acid (C18:0)	0.77	0.77	1.02	1.01	0.0002	0.0002	0.7130	0.7937
Phosphatidylserines	PS_Arachidonic acid (C20:cis[5,8,11,14]4)	0.91	0.83	0.97	0.89	0.2142	0.0268	0.7410	0.1579
Phosphatidylserines	PS_cis-Vaccenic acid (C18:cis[11]1)	**2.02**	**2.22**	0.95	1.04	0.0002	4.28E-05	0.7259	0.7698
Phosphatidylserines	PS_dihomo-gamma-Linolenic acid (C20:cis[8,11,14]3)	1.11	1.03	1.12	1.05	0.1585	0.6460	0.1040	0.4862
Phosphatidylserines	PS_Docosadienoic acid (C22:cis[13,16]2)	0.84	1.06	0.85	1.08	0.3036	0.7173	0.3535	0.6407
Phosphatidylserines	PS_Docosahexaenoic acid (C22:cis[4,7,10,13,16,19]6)	1.24	1.03	1.26	1.05	0.0528	0.7567	0.0410	0.6617
Phosphatidylserines	PS_Docosapentaenoic acid (C22:cis[4,7,10,13,16]5)	0.92	0.94	1.01	1.03	0.7010	0.7768	0.9628	0.8827
Phosphatidylserines	PS_Linoleic acid (C18:cis[9,12]2)	1.13	1.09	1.14	1.10	0.3277	0.4571	0.2888	0.4081
Phosphatidylserines	PS_Myristic acid (C14:0)	**2.84**	0.84	**2.63**	0.78	0.1949	0.8284	0.2295	0.7504
Phosphatidylserines	PS_Myristoleic acid (C14:cis[9]1)	1.13	1.15	1.09	1.11	0.6862	0.6451	0.7742	0.7311
Phosphatidylserines	PS_Oleic acid (C18:cis[9]1)	0.92	0.90	1.11	1.08	0.7439	0.6824	0.7079	0.7702
Phosphatidylserines	PS_Palmitic acid (C16:0)	1.75	1.83	0.91	0.95	1.67E-06	5.98E-07	0.2254	0.5282
Phosphatidylserines	PS_Stearic acid (C18:0)	0.77	0.74	1.06	1.03	0.0029	0.0011	0.4149	0.7265
Sphingomyelins	SM_Sphingomyelin (d16:1,C16:0)	1.11	0.98	1.19	1.06	0.5936	0.9227	0.3669	0.7791
Sphingomyelins	SM_Sphingomyelin (d16:1,C18:0)	0.95	0.94	1.43	1.42	0.7576	0.7271	0.0571	0.0617
Sphingomyelins	SM_Sphingomyelin (d16:1,C22:0)	0.62	0.56	0.92	0.84	0.0003	4.26E-05	0.4649	0.1138
Sphingomyelins	SM_Sphingomyelin (d16:1,C24:1)	1.01	0.94	0.98	0.91	0.9239	0.6411	0.8778	0.4769
Sphingomyelins	SM_Sphingomyelin (d17:1,C16:0)	1.18	1.06	1.38	1.23	0.4278	0.7967	0.1395	0.3306
Sphingomyelins	SM_Sphingomyelin (d17:1,C18:0)	0.78	0.78	0.91	0.92	0.0565	0.0618	0.4604	0.4886
Sphingomyelins	SM_Sphingomyelin (d17:1,C20:0)	0.55	0.57	1.03	1.07	0.0062	0.0089	0.8720	0.7425
Sphingomyelins	SM_Sphingomyelin (d17:1,C22:0)	0.64	0.56	1.04	0.91	0.0008	7.15E-05	0.7552	0.4090
Sphingomyelins	SM_Sphingomyelin (d17:1,C23:0)	1.21	1.16	0.90	0.86	0.3292	0.4341	0.5677	0.4425
Sphingomyelins	SM_Sphingomyelin (d17:1,C24:0)	0.99	0.88	1.04	0.92	0.9680	0.3169	0.7807	0.4884
Sphingomyelins	SM_Sphingomyelin (d17:1,C24:1)	0.94	0.99	1.04	1.10	0.6734	0.9672	0.7897	0.5194
Sphingomyelins	SM_Sphingomyelin (d18:1,C14:0)	1.26	1.05	1.41	1.17	0.1790	0.7810	0.0548	0.3566
Sphingomyelins	SM_Sphingomyelin (d18:1,C16:0)	1.15	1.02	1.56	1.38	0.4725	0.9315	0.0297	0.1014
Sphingomyelins	SM_Sphingomyelin (d18:1,C18:0)	0.80	0.75	1.23	1.16	0.0828	0.0334	0.1121	0.2460
Sphingomyelins	SM_Sphingomyelin (d18:1,C19:0)	0.94	1.14	0.86	1.05	0.7157	0.4631	0.4159	0.7776
Sphingomyelins	SM_Sphingomyelin (d18:1,C20:0)	0.71	0.62	1.10	0.97	0.0014	6.92E-05	0.2902	0.7073
Sphingomyelins	SM_Sphingomyelin (d18:1,C21:0)	1.02	1.00	0.98	0.97	0.9302	0.9890	0.9295	0.8711
Sphingomyelins	SM_Sphingomyelin (d18:1,C22:0)	0.71	0.55	1.14	0.88	0.0004	6.99E-07	0.1102	0.1148
Sphingomyelins	SM_Sphingomyelin (d18:1,C22:1)	1.73	1.66	1.01	0.97	0.0088	0.0141	0.9722	0.8499
Sphingomyelins	SM_Sphingomyelin (d18:1,C23:0)	1.23	1.09	0.99	0.88	0.2239	0.6058	0.9576	0.4395
Sphingomyelins	SM_Sphingomyelin (d18:1,C23:1)	0.98	1.06	1.05	1.13	0.9263	0.7538	0.7923	0.5057
Sphingomyelins	SM_Sphingomyelin (d18:1,C24:0)	0.91	0.78	1.19	1.02	0.4922	0.0692	0.1857	0.8922
Sphingomyelins	SM_Sphingomyelin (d18:1,C24:1)	1.02	0.89	1.26	1.10	0.9093	0.4315	0.1222	0.4884
Sphingomyelins	SM_Sphingomyelin (d18:1,C24:2)	1.53	1.42	1.55	1.44	0.0524	0.1020	0.0473	0.0927
Sphingomyelins	SM_Sphingomyelin (d18:2,C16:0)	1.04	1.07	1.16	1.20	0.8097	0.6580	0.3121	0.2293
Sphingomyelins	SM_Sphingomyelin (d18:2,C18:0)	0.78	0.97	0.95	1.20	0.1494	0.8749	0.7730	0.3044
Sphingomyelins	SM_Sphingomyelin (d18:2,C20:0)	0.71	0.71	1.10	1.11	0.0177	0.0189	0.4660	0.4486
Sphingomyelins	SM_Sphingomyelin (d18:2,C22:0)	0.67	0.63	0.94	0.88	0.0024	0.0007	0.6057	0.2899
Sphingomyelins	SM_Sphingomyelin (d18:2,C22:1)	1.64	1.70	0.89	0.92	0.0287	0.0204	0.5642	0.6807
Sphingomyelins	SM_Sphingomyelin (d18:2,C23:0)	1.24	1.24	0.95	0.96	0.2618	0.2560	0.8006	0.8117
Sphingomyelins	SM_Sphingomyelin (d18:2,C24:0)	0.94	0.92	1.01	0.99	0.5671	0.4594	0.9228	0.9409
Sphingomyelins	SM_Sphingomyelin (d18:2,C24:2)	1.55	1.49	1.35	1.30	0.0237	0.0383	0.1029	0.1559
Triacylglycerols	TAG_Arachidonic acid (C20:cis[5,8,11,14]4)	1.40	1.32	**0.35**	**0.33**	0.1085	0.1846	8.39E-05	4.52E-05
Triacylglycerols	TAG_cis-Vaccenic acid (C18:cis[11]1)	**2.05**	**2.40**	0.85	1.00	0.0386	0.0140	0.6187	0.9981
Triacylglycerols	TAG_conjugated Linoleic acid (C18:cis[9]trans[11]2)	1.27	**2.62**	**0.47**	0.98	0.6571	0.0822	0.1695	0.9710
Triacylglycerols	TAG_dihomo-gamma-Linolenic acid (C20:cis[8,11,14]3)	1.33	1.38	**0.27**	**0.28**	0.3400	0.2760	0.0003	0.0005
Triacylglycerols	TAG_Docosadienoic acid (C22:cis[13,16]2)	1.11	0.99	0.77	0.68	0.6163	0.9454	0.2271	0.0849
Triacylglycerols	TAG_Docosahexaenoic acid (C22:cis[4,7,10,13,16,19]6)	1.55	1.59	**0.25**	**0.25**	0.1026	0.0868	4.77E-05	5.72E-05
Triacylglycerols	TAG_Docosapentaenoic acid (C22:cis[4,7,10,13,16]5)	1.02	1.20	**0.17**	**0.20**	0.9645	0.6211	0.0002	0.0004
Triacylglycerols	TAG_Docosapentaenoic acid (C22:cis[7,10,13,16,19]5)	**2.32**	**3.05**	**0.07**	**0.09**	0.1905	0.0884	0.0006	0.0015
Triacylglycerols	TAG_Docosatetraenoic acid (C22:cis[7,10,13,16]4)	1.36	1.29	**0.33**	**0.31**	0.1971	0.2801	0.0002	0.0001
Triacylglycerols	TAG_Eicosadienoic acid (C20:cis[11,14]2)	1.14	1.40	**0.29**	**0.35**	0.6553	0.2522	0.0004	0.0021
Triacylglycerols	TAG_Eicosaenoic acid (C20:cis[11]1)	0.75	0.99	**0.48**	0.63	0.2641	0.9633	0.0085	0.0769
Triacylglycerols	TAG_Eicosanoic acid (C20:0)	0.71	0.76	1.01	1.09	0.3723	0.4733	0.9700	0.8275
Triacylglycerols	TAG_Eicosapentaenoic acid (C20:cis[5,8,11,14,17]5)	**4.11**	**2.70**	0.65	**0.42**	0.0790	0.2056	0.5698	0.2723
Triacylglycerols	TAG_Elaidic acid (C18:trans[9]1)	1.04	1.10	1.25	1.33	0.9224	0.8082	0.5840	0.4899
Triacylglycerols	TAG_Erucic acid (C22:cis[13]1)	1.01	1.09	0.53	0.57	0.9792	0.7374	0.0257	0.0478
Triacylglycerols	TAG_gamma-Linolenic acid (C18:cis[6,9,12]3)	1.85	1.37	0.93	0.69	0.0427	0.2738	0.8109	0.2080
Triacylglycerols	TAG_Hexadecenoic acid (C16:trans[9]1)	**3.52**	**3.67**	1.36	1.42	0.0008	0.0006	0.3281	0.2700
Triacylglycerols	TAG_Linoleic acid (C18:cis[9,12]2)	1.64	1.55	1.01	0.95	0.0991	0.1445	0.9800	0.8505
Triacylglycerols	TAG_Linolenic acid (C18:cis[9,12,15]3)	1.85	1.67	0.74	0.67	0.1152	0.1809	0.4264	0.2949
Triacylglycerols	TAG_Myristic acid (C14:0)	1.74	**2.53**	0.92	1.35	0.1575	0.0237	0.8320	0.4346
Triacylglycerols	TAG_Oleic acid (C18:cis[9]1)	0.96	0.89	1.27	1.19	0.8932	0.7348	0.4677	0.5996
Triacylglycerols	TAG_Palmitic acid (C16:0)	**2.13**	**2.21**	1.34	1.39	0.0569	0.0471	0.4345	0.3810
Triacylglycerols	TAG_Palmitoleic acid (C16:cis[9]1)	**3.25**	**3.33**	1.35	1.38	0.0049	0.0043	0.4192	0.3820
Triacylglycerols	TAG_Stearic acid (C18:0)	0.65	0.62	1.31	1.25	0.2480	0.2017	0.4577	0.5385
Unknown lipid	Unknown lipid (1000329990007)	0.97	1.00	1.09	1.12	0.8617	0.9870	0.5862	0.4844
Unknown lipid	Unknown lipid (1000329990008)	0.93	0.91	0.97	0.95	0.7324	0.6652	0.8805	0.8090

Unknown lipid	Unknown lipid (1000329990027)	0.82	0.98	0.65	0.77	0.5075	0.9538	0.1443	0.3733
Unknown lipid	Unknown lipid (1100339990001)	1.11	1.09	1.26	1.24	0.6294	0.6790	0.2733	0.3032
Unknown lipid	Unknown lipid (1100339990002)	0.70	0.61	1.52	1.31	0.1125	0.0295	0.0633	0.2171

Supporting Figure 1

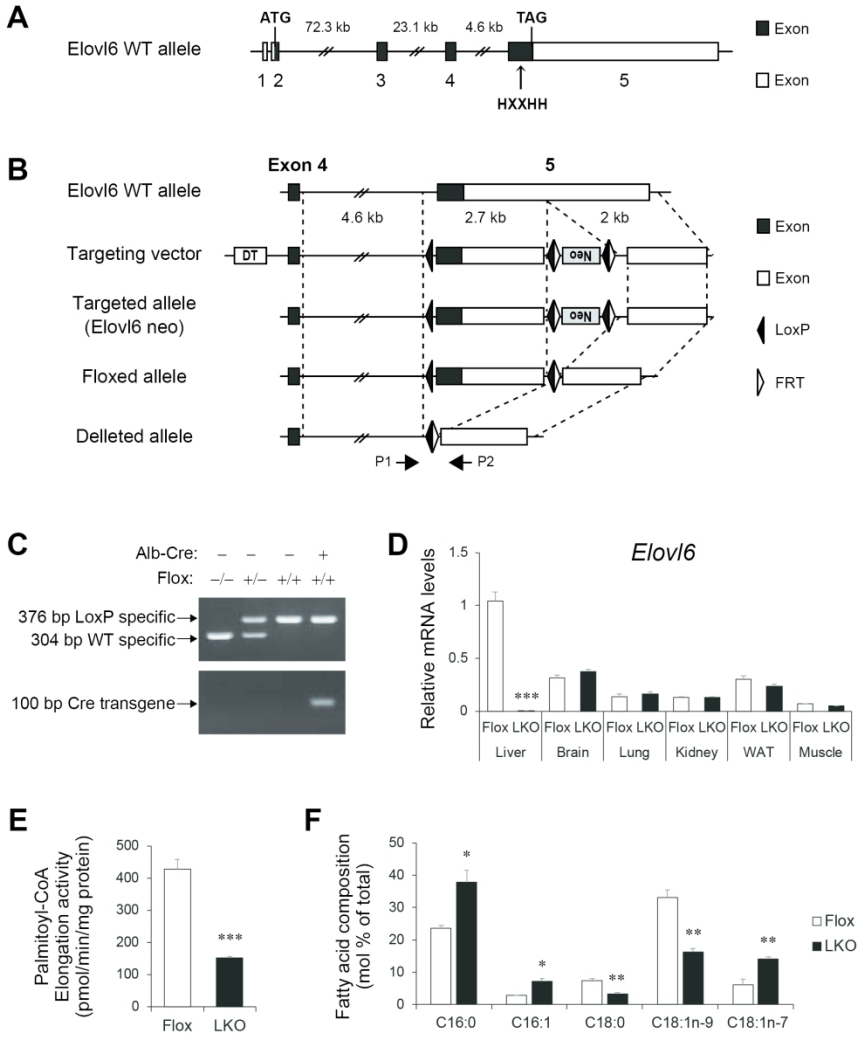

Supporting Figure 2

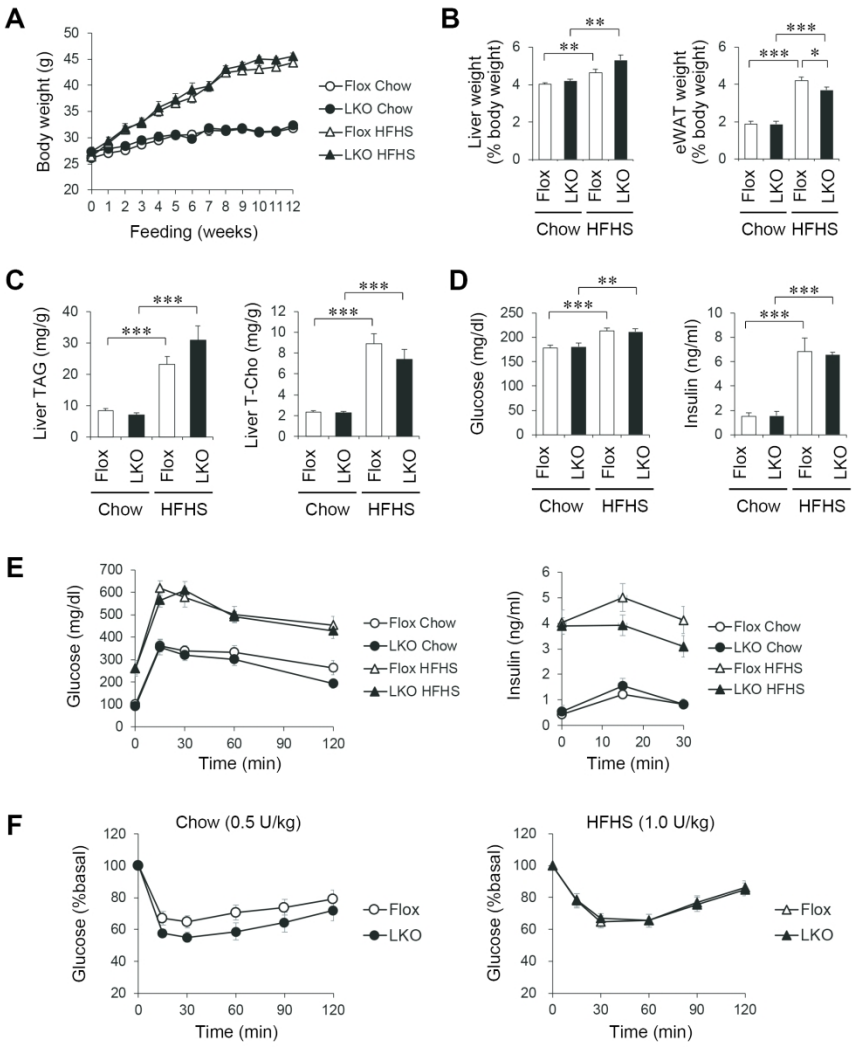

Supporting Figure 3

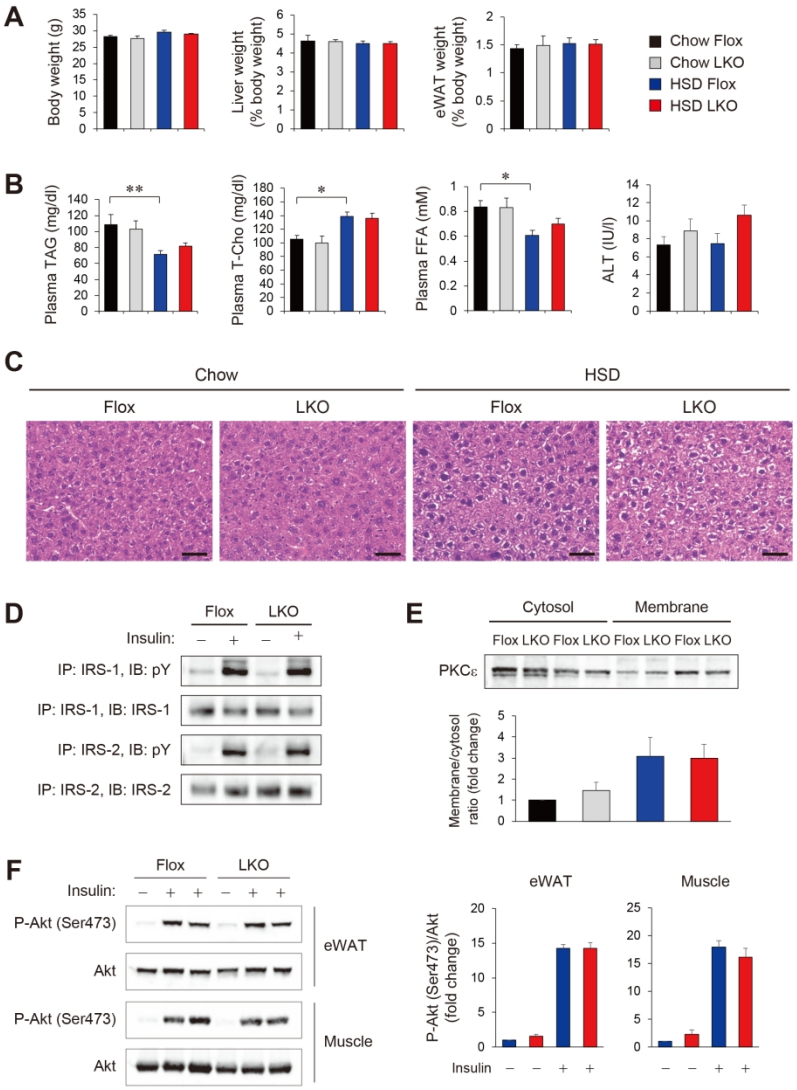

Supporting Figure 4

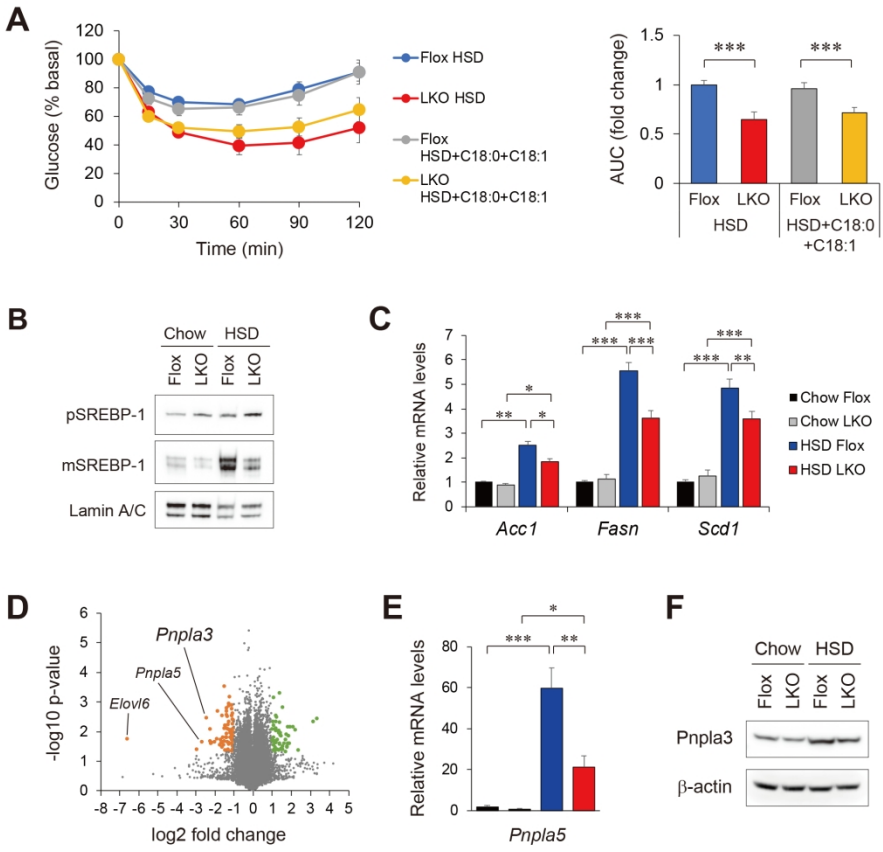

Supporting Figure 5

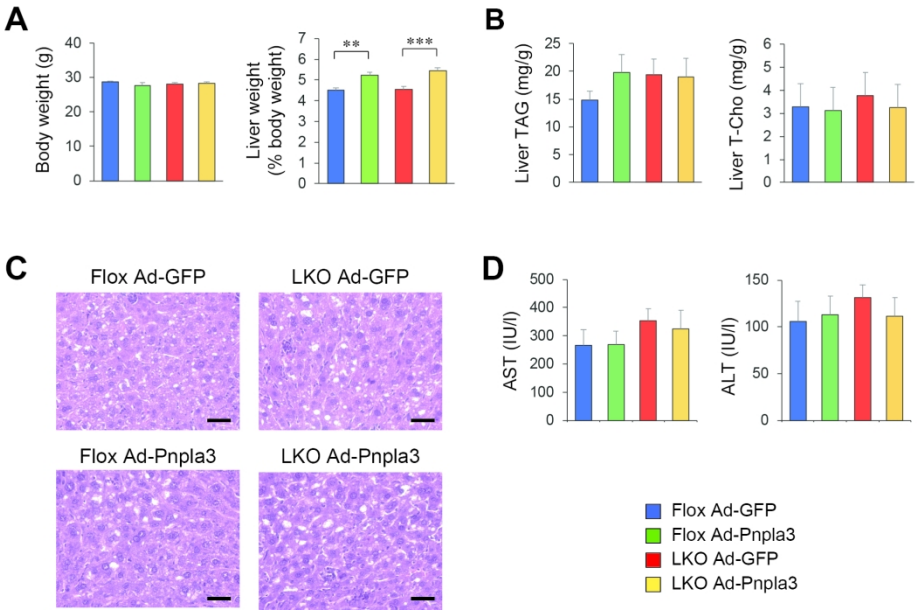

Supporting Figure 6

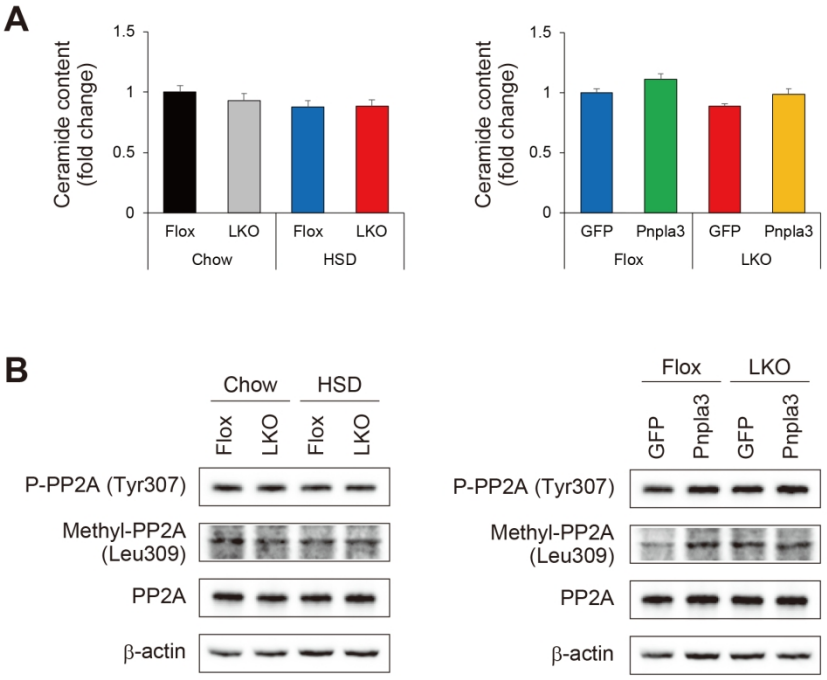

Supporting Figure 7

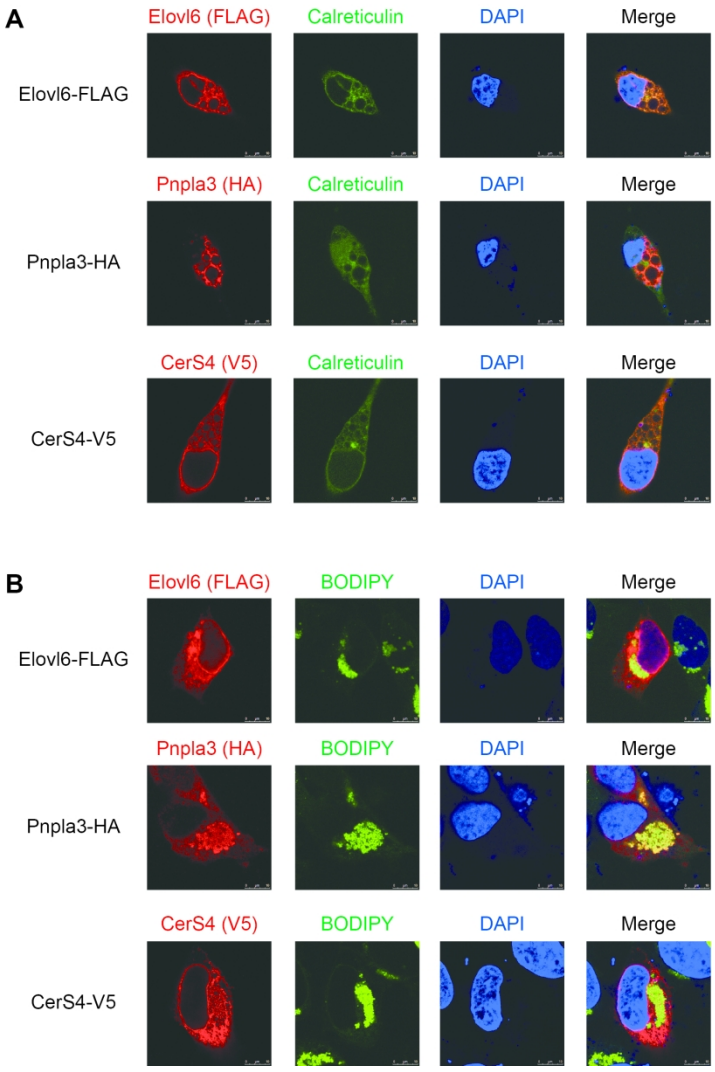

Supporting Figure 8

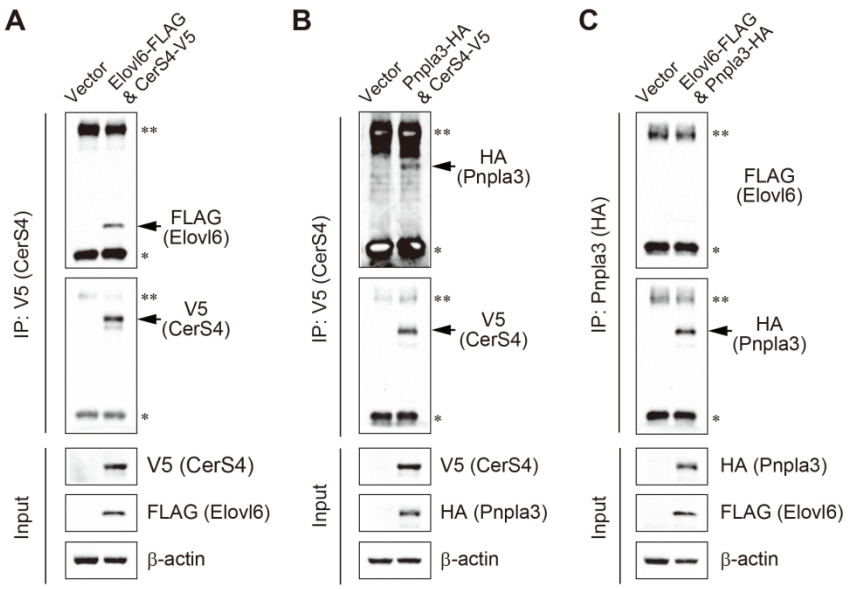

Supporting Figure 9

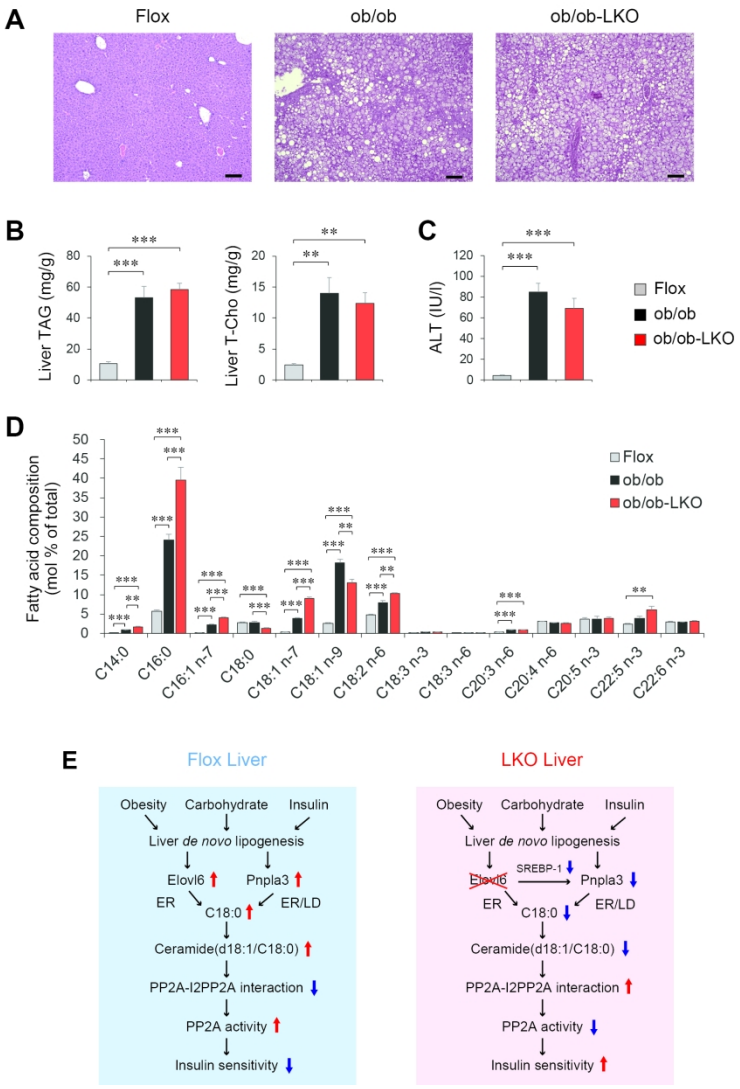

Figure for Reviewers

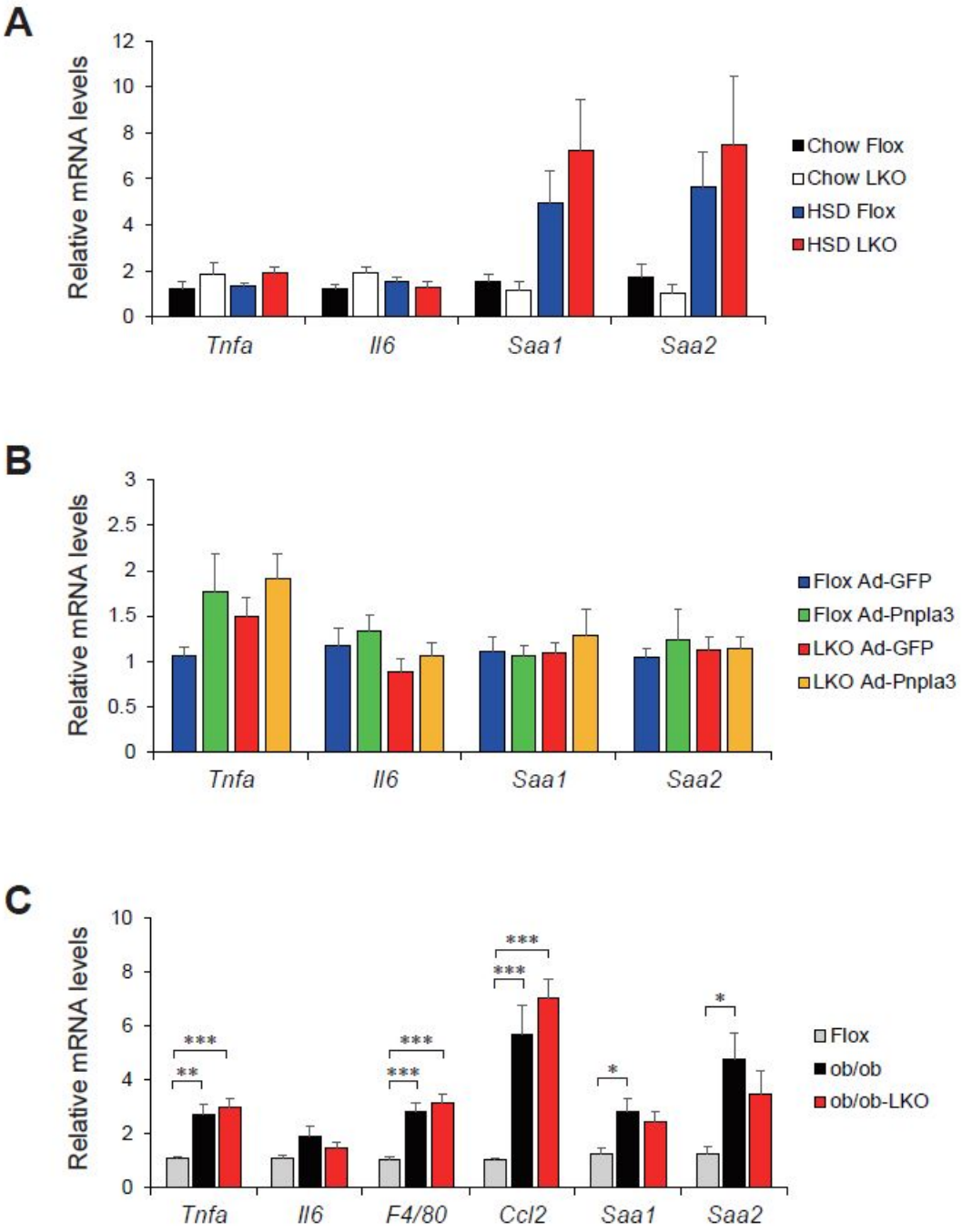

(**A**) Expression of tumor necrosis factor α (*Tnfa*), interleukin 6 (*Il6*), serum amyloid A 1 (*Saa1*), and serum amyloid A 2 (*Saa2*) in liver from Flox and LKO mice fed either a chow or HSD (n = 11−18 per group). (**B**) Expression of *Tnfa*, *Il6*, *Saa1*, and *Saa2* in liver from HSD-fed Flox and LKO mice infected with either Ad-GFP or Ad-Pnpla3 (n = 8−14 per group). (**C**) Expression of *Tnfa*, *Il6*, *F4/80*, chemokine (C-C motif) ligand 2 (*Ccl2*), *Saa1*, and *Saa2* in liver from Flox, ob/ob, and ob/ob-LKO mice (n = 8−14 per group). Results are expressed as mean ± SEM. *p < 0.05, **p < 0.01, ***p < 0.001.